



Universiteit
Leiden

The Netherlands

Quantifying nucleosome dynamics and protein binding with PIE-FCCS and spFRET

Martens, C.L.G.

Citation

Martens, C. L. G. (2023, February 1). *Quantifying nucleosome dynamics and protein binding with PIE-FCCS and spFRET*. *Casimir PhD Series*. Retrieved from <https://hdl.handle.net/1887/3514600>

Version: Publisher's Version

License: [Licence agreement concerning inclusion of doctoral thesis in the Institutional Repository of the University of Leiden](#)

Downloaded from: <https://hdl.handle.net/1887/3514600>

Note: To cite this publication please use the final published version (if applicable).

Quantifying nucleosome dynamics and protein binding with PIE-FCCS and spFRET

Proefschrift

ter verkrijging van
de graad van doctor aan de Universiteit Leiden,
op gezag van rector magnificus prof. dr. ir. H. Bijl,
volgens besluit van het college voor promoties
te verdedigen op 1 februari 2023
klokke 10.00 uur

door

Christine Laurentia Gerarda Martens

geboren te Nijmegen
in 1985

Promotor: Prof. dr. ir. S.J.T. van Noort
Promotiecommissie: Prof. dr. C. Joo (Delft University of Technology)
Prof. dr. H. Schiessel (TU Dresden, Dresden, Germany)
Prof. dr. J. Aarts
Dr. M.I. Huber
Dr. M.J.M. Schaaf
Prof. dr. T. Schmidt

Casimir PhD Series, Delft-Leiden, 2023-02
ISBN 978-90-8593-550-6

The cover is designed by the author and shows abstractions of several levels of DNA compaction and elements of fluorescence correlation spectroscopy.

The work described in this thesis was performed in the FOM programme 'Crowd management: the physics of DNA processing in complex environments' funded by the Foundation for Fundamental Research on Matter (FOM), now the Netherlands Organization for Scientific Research (NWO).

Voor mijn familie

Inveniam viam aut faciam

Hannibal Barca

Contents

1	Introduction	1
1.1	DNA: compaction vs. accessibility	2
1.2	Nucleosome structure and dynamics	7
1.2.1	Sequence-dependent properties	8
1.2.2	Nucleosome dynamics	9
1.2.3	Histone tail modifications	10
1.2.4	Transcription factors	11
1.3	Single-molecule microscopy and Förster Resonance Energy Transfer (FRET) for nucleosome research	13
1.4	Scope of this thesis	15
2	Methods and advances in single-molecule fluorescence microscopy and spectroscopy	17
2.1	Introduction	18
2.2	Methods and materials	19
2.2.1	FRET	19
2.2.2	Choice of fluorophores	20
2.2.3	Confocal microscope setup	23
2.3	Single-molecule burst microscopy	24
2.3.1	ALEX-spFRET burst analysis	25
2.3.2	Scanning Confocal Microscopy	27
2.4	Fluorescence Correlation Spectroscopy	29
2.4.1	Photophysics	30
2.4.2	Microscope calibration and corrections	31
2.4.3	Fluorescence Crosscorrelation Spectroscopy	35
2.4.4	Conformational dynamics	36
2.5	FCS data analysis	39
2.5.1	Data acquisition and processing	40
2.5.2	Assigning channels, PIE/ALEX phases and excluding aggregates	40
2.5.3	Correlation method and single-population fit	43
2.5.4	Multi-population fit strategies	45

2.6	Conclusions	46
3	Optimizing DNA synthesis, purification, and handling for single-pair FRET experiments on nucleosomes	47
3.1	Introduction	48
3.2	Construct design	48
3.3	DNA synthesis and purification	49
3.3.1	Decelerated PCR to optimize synthesis of DNA constructs from long primers	50
3.3.2	PEG and salt-induced precipitation optimized for long primers and short DNA strands	52
3.4	Nucleosome reconstitution	53
3.5	Surface passivation and molecule immobilization	55
3.6	Conclusions	59
4	Nucleosome stability and accessibility depends on linker DNA length, nucleosomal DNA sequence, buffer composition	61
4.1	Introduction	62
4.2	Theory	63
4.2.1	Nucleosome dynamics	63
4.2.2	Fluorescence Correlation Spectroscopy (FCS)	64
4.2.3	Nucleosome dynamics measured with FCS-PIE	65
4.3	Materials and methods	66
4.3.1	Nucleosome reconstitution and sample preparation	66
4.3.2	Single-molecule fluorescence spectroscopy	67
4.3.3	Burst analysis	67
4.3.4	Averaged fluorescence intensity analysis	68
4.3.5	FCS analysis	69
4.4	Results	70
4.4.1	Nucleosome conformation at low NaCl concentration	70
4.4.2	Electrostatic interactions in nucleosome 39-12	71
4.4.3	Effects of linker DNA	74
4.4.4	Effects of nucleosomal DNA sequence	80
4.4.5	Effects of buffer composition	84
4.5	Discussion and conclusions	86

5	H3K36me3 decreases nucleosome stability and increases LEDGF affinity in chromatin	91
5.1	Introduction	92
5.2	Materials and methods	93
5.2.1	Sample preparation and nucleosome reconstitution .	93
5.2.2	LEDGF purification and labeling	94
5.2.3	Single-molecule fluorescence microscopy	94
5.2.4	Fluorescence Correlation Spectroscopy	95
5.2.5	Fluorescence Cross-Correlation Spectroscopy and binding affinity	97
5.2.6	Multi-component fit and nucleosome dynamics . . .	98
5.3	Results	99
5.3.1	Effect of H3K36me3 on the stability of nucleosomes	99
5.3.2	LEDGF binding to DNA and nucleosomes, and resulting ATTO532 quenching	101
5.3.3	Effect of LEDGF binding on nucleosome dynamics . .	105
5.4	Discussion and conclusions	109
6	Quantifying transcription factor affinity in chromatin	111
6.1	Introduction	112
6.2	Materials and methods	114
6.2.1	DNA containing c-Jun and GR response elements . .	114
6.2.2	Recombinant c-Jun	114
6.2.3	GR transfection and activation	114
6.2.4	Single-molecule fluorescence correlation spectroscopy	116
6.2.5	FCCS analysis and binding affinity	117
6.3	Results	118
6.3.1	c-Jun interactions with DNA	118
6.3.2	GR activity	119
6.3.3	GR affinity for DNA and nucleosomes	122
6.3.4	Increasing nucleosome concentration increases complex concentration	124
6.4	Discussion and conclusions	126
	Samenvatting	159
	Summary	165

Publications	169
Curriculum Vitae	171
Acknowledgements	173

CHAPTER 1

INTRODUCTION

1.1 DNA: compaction vs. accessibility

The code of life is written in only four symbols: A, C, G and T, representing the nucleotide bases Adenine, Cytosine, Guanine and Thymine of DNA[1]. After being read during transcription, DNA is translated into the myriad of proteins, peptides and enzymes that build, maintain and regulate all the structures and functions of an organism[2]. The human genomic DNA has a contour length of about two meters, six orders of magnitude larger than the cell's nucleus, which has a diameter of approximately six micrometers[3]. In order to fit inside the nucleus, the genome is dramatically reduced in size through the formation of nucleosomes and chromatin[4][5]. And, although being in this highly condensed state, DNA is involved in fast and frequent processes such as transcription and DNA repair[6]. These processes need direct DNA access, and hence depend on a change in chromatin compaction.

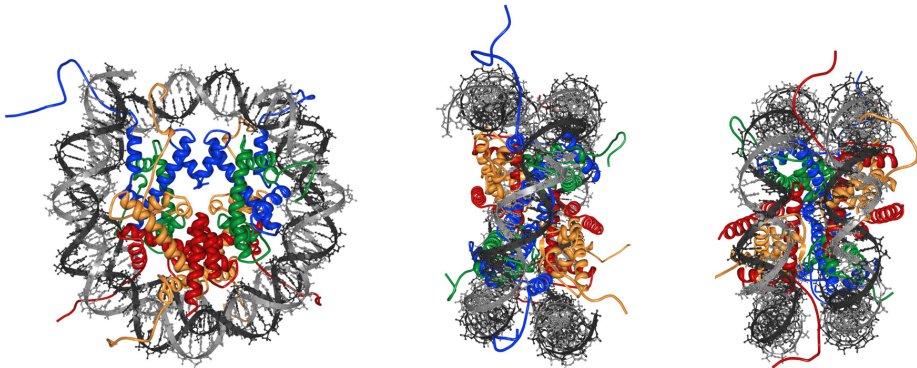


FIGURE 1.1: **The crystal structure of the nucleosome core particle (NCP) shows it near-perfect symmetry.** In the center of the NCP is the histone octamer (HO) consisting of two copies of H2A (yellow), H2B (red), H3 (blue), and H4 (green). Wrapped around the histone core is 147 base pairs of DNA (light and dark grey). DOI:10.2210/pdb1EQZ/pdb NDB:PD0137, rendered with RSCB PDB Protein workshop v.42.0.

In eukaryotic cells, the first order of compaction is the nucleosome (figure 1.1). This basic unit of chromatin consists of 147 base pairs wrapped 1.6 times around a histone core, an octameric ensemble of compactor proteins[7]. The nucleosome has been extensively characterized and will be discussed in the next paragraph. Larger order structures of compacted

DNA are however less well-elucidated. The 'textbook' explanation has long been that nucleosomes form an almost evenly spaced beads-on-a-string configuration (figure 1.2a).

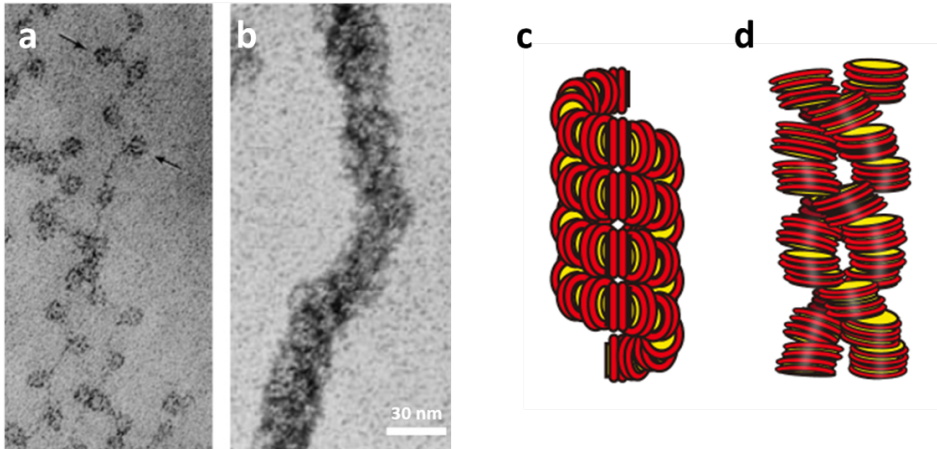


FIGURE 1.2: **Strings of nucleosomes are compacted into fibers under specific conditions.** One of the first observations of the nucleosomes (a) and chromatin fiber (b) was in chicken erythrocytes; picture from Olins et al.[8]. Modelling nucleosome compaction into a 30 nm fiber results into one- (c) or two-start fibers (d), depending on linker DNA length.[9]

In vivo studies have shown that there indeed seems to be a discrete spacing between nucleosomes, but that this spacing adheres to a $10n+5$ rule, with n the number of base pairs of linker DNA[5]. The next order of compaction supposedly formed is the 30 nm fiber (figure 1.2b), named for its width. Based on EM images[10][11] models were constructed, in which the 30nm fiber is formed by a string of nucleosomes compacted via a repetitive structure, dubbed the one-start helix, or solenoid, configuration (figure 1.2c). When the length of the linker DNA between its nucleosomes is shortened, the fiber takes on a two-start, or zig-zag, configuration (figure 1.2d). Both structures have been confirmed through *in vitro* experiments[12][13]. However, *in vivo*, no evidence of chromatin compaction through these configurations has been found[9]. The predominant reason for this lies in the set-up of the *in vitro* experiments; DNA containing nucleosome positioning elements alternated with the same length of linked DNA (following the $10n$ rule) is used. In this way, a high degree of control in synthesis and

probing of the fibers is exerted. Although using synthetic DNA sequences and predetermined linker lengths has its advantages, it provides a limited insight in the mechanisms of accessibility of higher order compacted DNA. The 'problem' *in vivo* is that, even excluding the influence of chromatin remodelers and other interactors, the sequence of the genome is much more varied, influencing the positioning and stability of nucleosomes.

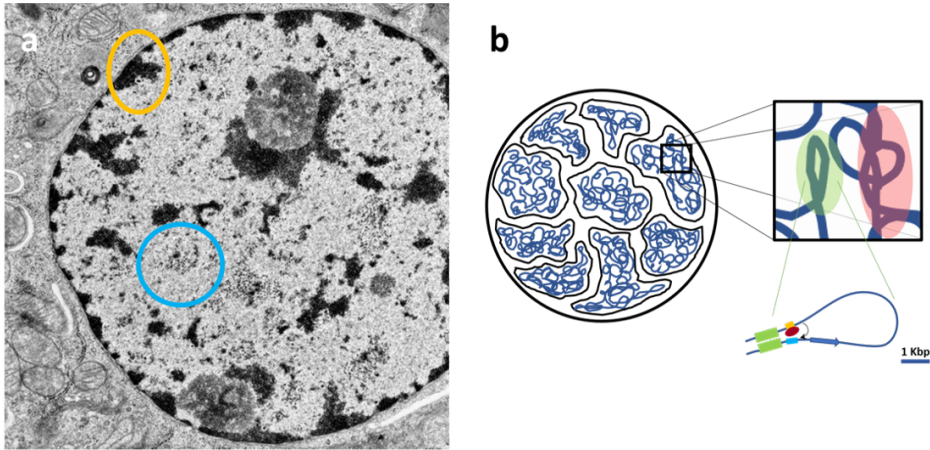


FIGURE 1.3: **In vivo chromatin is compacted into defined regions.** **a)** Globular structures in chromatin have long been classified as either eu- or heterochromatin (in blue, respectively orange circle) depending on their accessibility[14]. **b)** Recently the classification of topologically associated domains (TADs) has gained notice. TADs are defined as 3D interactions of DNA sequences separated from each other in 2D by 100 to 10.000 base pairs[15].

Over the past years, through the improvement of techniques able to probe chromatin *in vivo*, new insights into the nature of its compaction have arisen. Instead of different highly compacted structures, more global structures of accessible and in- or less accessible chromatin have been observed, categorized as euchromatin (eu- deriving from the Hellenic word for good) or heterochromatin (hetero- because it has not a single definable structure and is generally in a state of inactivity)[16][14] (figure 1.3a; euchromatin in blue circle, heterochromatin in orange circle). Euchromatin, or a part thereof, is sometimes referred to as hyperaccessible nucleosomes. Mnase seq and other digestion experiments have shown that chromatin, regardless of being in eu- or heterochromatin form, is compacted not in 30 nm sized

structures, but in smaller units[17][18]. One can argue that these structures consist of small numbers of nucleosomes, as well as less defined in linker lengths and nucleosomal stability[19], and hence cannot distribute the DNA bending energy over its local structure as efficiently as repetitive, highly compacted 30 nm fibers.

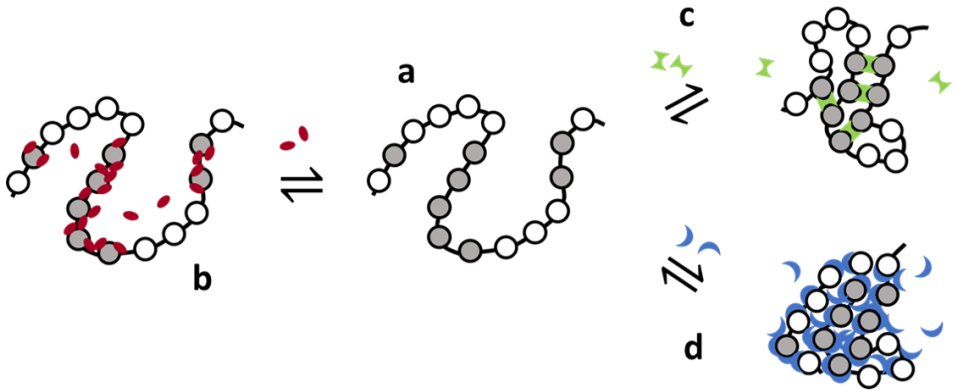


FIGURE 1.4: **Different protein binding mechanisms induce further compaction of nucleosomes on a string through phase separation.** **a)** nucleosomes on a string are shown without modifiers. **b)** Proteins binding cooperatively to nucleosomes do not necessarily induce compaction for effective functioning. **c)** Bridging proteins compact nucleosomes by cross-linking. **d)** Other molecules induce multivalent interactions with nucleosomes, thereby driving out other molecules and collapsing the chromatin structure to a more condensed state.

Recently a strong case has been made for the existence of topological associated domains (TADs)[20][15], in which sites of non-neighbouring compacted DNA interact with each other (figure 1.3b).

Different biophysical concepts are currently used to explain the formation of these domains in a self-organizing manner and without (or minimal) energy consumption. In addition to cooperative binding to a preformed chromatin structure, as depicted in figure 1.4b, two different mechanisms for the formation of phase-separated chromatin sub-compartments have been proposed[21]. One is based on bridging proteins that cross-link polymer segments with particular properties (also seen in the compaction of archeal DNA), inducing a collapse of the chromatin into an ordered globular phase (figure 1.4c). The other mechanism is based on multivalent interac-

tions among soluble molecules that bind to chromatin (figure 1.4d). These interactions can induce liquid-liquid phase separation, which drives the assembly of liquid-like nuclear bodies around the respective binding sites in chromatin.

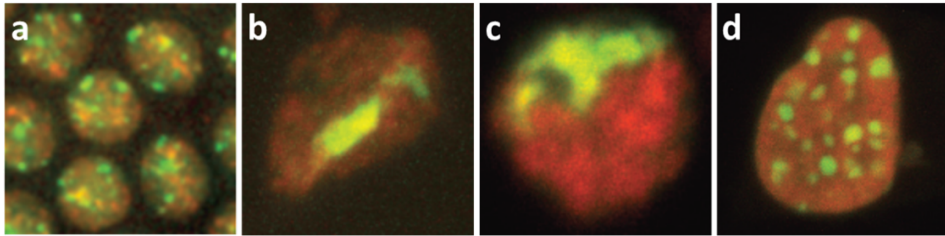


FIGURE 1.5: **In vivo phase separation induced by HP1 α .** HP1 α labeled with GFP (green), H2A labelled with mCherry (red). Different cell types show the formation of globular structures where HP1 α is present, but H2A is not. Cells are **a**) *Drosophila* embryo and **b**) adult gut, **c**) cultured Kc and **d**) mouse fibroblast NIH3T3. Images adapted from [22]

Persuading evidence that certain proteins drive chromatin to different states of compaction *in vivo* has been found by Strom et al.[22], who show that HP1 α (heterochromatin protein 1 α) undergoes liquid-liquid demixing *in vitro* as well as *in vivo* as compared to histone H2A. Distinct globular domains of heterochromatin containing HP1 α but no or little amounts of H2A can be found throughout different cell types, indicating the assembly of these domains depends on the (multivalent) interactions of the protein with the chromatin instead of being a cell types specific effect (figure 1.5). Results supporting the hypothesis DNA is compartmentalized through LLPS keep being added[23][24][25][26].

What should be concluded from the recent findings *in vivo* presented here is that, regardless what and how higher order structures of chromatin form, or how they interact, they are made up of nucleosomes. And that when one attribute of the nucleosome is changed, for instance through binding of a transcription factor or remodeller, there is strong evidence this brings about a change in the higher-order structure as well. Thereby gaining a better understanding in the mechanisms of the nucleosome will result in more insight into the more complex structures or domains it is a part of.

1.2 Nucleosome structure and dynamics

The nucleosome, or more accurately, the nucleosome core particle (NCP), consists of 147 base pairs of DNA wrapped around a histone core consisting of two copies of four histones: H2A, H2B, H3 and H4 (figure 1.6a). For decades the structure of the nucleosome has been the subject of extensive research[27][28][29][30]. Although the composition of the nucleosome had

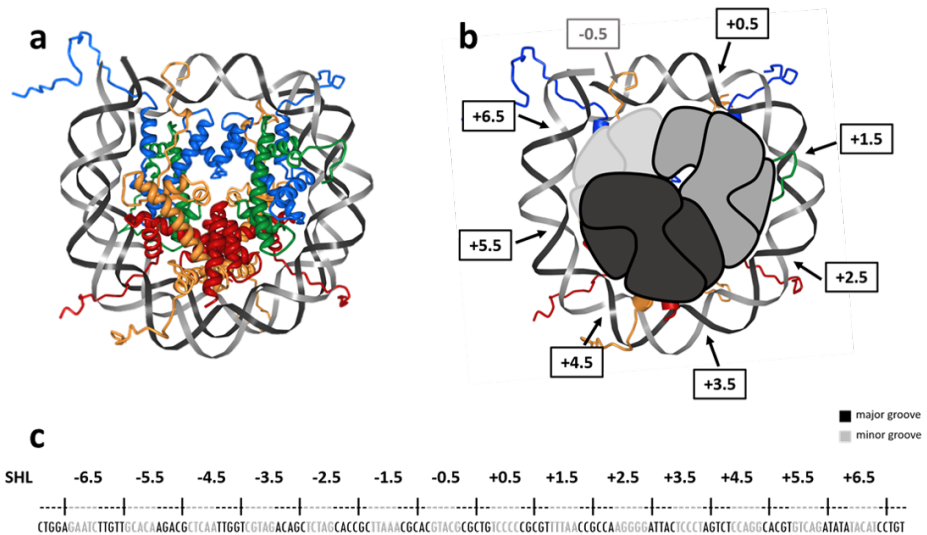


FIGURE 1.6: Preferred positioning of base pairs in the nucleosome pre-bends the DNA around the histone core. **a)** The H3/H4 tetramer (H3 (blue), H4 (green)) forms a diagonal ramp through the dyad, aligning the major and minor grooves of the DNA gyres in neighbouring planes. In this frontal view, the two H2A-H2B dimers perfectly overlap (H2A (yellow), H2B (red)). **b)** Projecting half of the wrapped DNA (75 base pairs) shows clearly how every 10 base pairs the DNA approaches the histone core through the minor groove. **c)** The Widom 601 sequence shows the preferred positioning of the A and T nucleotides in the minor grooves (grey) and the C and G nucleotides in the major grooves (black). (SHL = superhelical locations)

been realized before[31][32][33], it was the crystal structure at 2.8 angstrom resolution resolved by Luger et al. in 1997 that offered the first atomic depiction of the NCP[34]. It showed that the nucleosome has a pseudo-2-fold symmetry axis centered around a single base pair

(the dyad)[35]. What also became apparent from the crystal structure was that the path of nucleosomal DNA is nonuniform: the H2A/H2B dimers bind DNA in two planes perpendicular to DNA superhelical axis, while the central H3/H4 tetramer forms a diagonal ramp through the nucleosomal dyad, connecting these two planes (figure 1.6a). This way, the DNA gyres in neighbouring planes align their major and minor grooves as they track along the octamer surface. The DNA superhelix contacts the histone octamer at regular intervals (figure 1.6b) each ~ 10 base pairs, resulting in 14 superhelical locations (SHLs) denoting the minor grooves (figure 1.6c). These histone-DNA interfaces are mediated by extensive direct and water-mediated bonds, ionic interactions and nonpolar contacts.[36][37][38]

1.2.1 Sequence-dependent properties

Proof that the DNA sequence has an effect on nucleosome stability has been shown by Jonathan Widom through his SELEX (Systematic Evolution of Ligands by EXponential enrichment) experiments[39][40][41]. In a SELEX experiment, DNA sequences with high affinities for the histone octamer are selected by repeating the following steps: first, random DNA sequences are synthesized and reconstituted into nucleosomes. Their affinities for the histone octamer, as well as their ability to position nucleosomes are measured with several techniques (salt titration, etc). The best sequences are selected and amplified by PCR. This selection is repeated several times. Widom found that his selected sequences had higher affinity than natural nucleosome positioning sequences previously found. His most famous sequence is number 601, known by biologists, chemists and biophysicists as 'Widom 601' (601 has lesser-known siblings, among them 603, which is also often used for similar nucleosome experiments[40][42]).

Examination of the 601 sequence (figure 1.6c) and other high scoring sequences revealed common features: nucleotides arginine (A) and thymine (T) prefer positions in minor grooves, closer to the histone octamer, while cytosine (C) and guanine (G) prefer the major grooves[43]. These preferences stem from the difference in the number of hydrogen bonds between A-T (two bonds) and C-G (three bonds) making the latter pair more rigid[44][45]. Preferred positioning of base pairs also results in pre-bending DNA in such a way that less energy is needed to further bend the DNA around the histone core[43][46].

Recent micromanipulation experiments performed by Ngo et al. have shown nucleosomes respond highly asymmetrical to external forces[47]. The experiment combined optical tweezers capable of exerting piconewton forces with fluorescence microscopy on single nucleosomes, each nucleosome containing a pair of fluorescent labels at positions making FRET possible. Combining these techniques showed the nucleosome predominantly unwraps from the same end. It was proposed that this unwrapping preference is caused by the fact that the Widom 601 sequence making up the wrapped DNA portion is non-palindromic. This asymmetry makes one-half of the wrapped portion more rigid than the other and the researcher propose the stiffer half unwraps first because it cannot distribute the exerted stress as well as his flexible counterpart. This hypotheses was tested by flipping the inner two quarters of the 601 sequence, resulting in a nucleosome that unwraps from the other end. These experiments have been validated by the development of a theoretical framework by the Schiessel group[48][49]. Their model describes how the possible asymmetric metastable conformations of the nucleosome depend on the distribution of the kinetic energy over the bonds between base pairs.

1.2.2 Nucleosome dynamics

More work from the Widom group[50][51] has shown that nucleosomal DNA is not statically wrapped around the histone core but is in equilibrium between a wrapped and unwrapped state (figure 1.7). Through stopped-flow and time-resolved fluorescence experiments it was shown DNA at the exit of a nucleosome unwraps for 10 to 50 ms and rewraps for 250 ms[52]. This means that DNA is fully accessible for some period of time without being actively dissociated from the nucleosome. The stochastic switching between conformations has important functional implications for DNA-binding proteins that interact with chromatin. Widom and others have implied that nucleosome breathing is the rate-limiting step in some passive binding steps of transcriptional processes[50][53].

Nucleosomes are also able to reposition themselves by sliding DNA through the histone gyres without disrupting the histone octamer. This process is not stochastic but mediated by ATP-dependent chromatin remodelling enzymes[54][55].

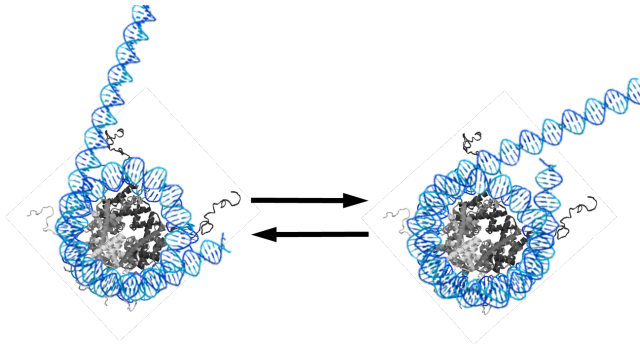


FIGURE 1.7: Depiction of unwrapping and (re-)wrapping of the DNA exits or tails of the nucleosome, also known as nucleosomal breathing.

1.2.3 Histone tail modifications

A way cells regulate transcription is through posttranslational modifications (PTMs) of histone tails. Modifications of the tails such as acetylation, methylation and phosphorylation change the structure and as a consequence the function of the tail and can act as markers for enzymes and proteins[56][57]. Acetylation of H4-tail lysines results in reduced compactness of chromatin, allowing access to DNA in acetylated chromatin regions to transcription factors[58][59]. Some modifications have been associated with increased chances of cancer cell formation, like methylation of histone tail H3K27[60]. Recent studies suggested that during mitosis, chromosome formation is triggered by a combination of modifications of the H3 and H4 tails[61][62][63]. Figure 1.8 provides an overview of most known histone tail modifications. The modification occurring most often is the acetylation of lysine and induces gene expression associated with metabolism[64][65]. Another common modification is methylation, which occurs as mono-, di- or trimethylation. These different degrees of methylation may be the reason why this modification seems more precise than acetylation. Acetyltransferases tend to act on several adjacent lysines to perhaps have a similar effect on chromatin structure as methylation. Histone methylation is associated with both gene upregulation and repression[66], and specific modifications are involved in DNA repair[67] and in some species are even linked to an increased lifespan[68][69].

One of the methylations associated with DNA repair is H3K36me3[70][71][72]. Several proteins involved in DNA mismatch

repair have a high affinity for H3K36me3, and it has been shown that because of elevated activity of mismatch repair, regions of the human genome containing high levels of H3K36me3 are less prone to somatic mutations[73]. H3K36me3 is also associated with heterochromatin[74]. Another protein recruited by H3K36me3 is LEDGF/p75. This protein is a co-activator in transcription, but has gained more attention due to its role in HIV DNA integration into host DNA[75][76][77]. LEDGF/p75 is hijacked by a pre-integration complex containing the HIV DNA and used as a bridge to the host DNA. It is not known whether the LEDGF/p75 binds first to the pre-integration complex and then to the host DNA, as LEDGF/p75 contains both an integrase-binding domain, through which it interacts with integrase proteins, as well as a N-terminal domain with a high affinity for chromatin[75].

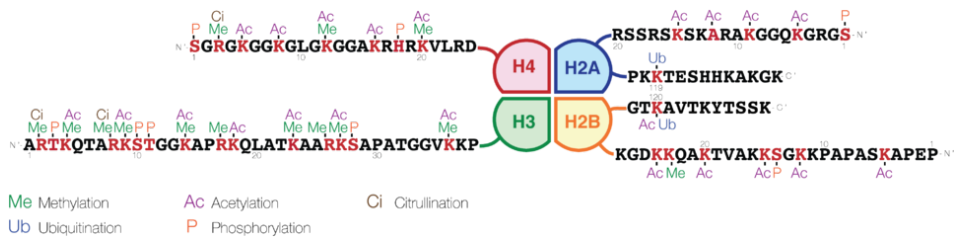


FIGURE 1.8: **Overview of most know posttranslational histone tail modifications.** Most PTMs are found in the tail of H3, presumably due to it having the highest lysine (K) content[61].

1.2.4 Transcription factors

Transcription factors (TFs) are proteins regulating the activation and repression of genes by preparing chromatin for the recruitment of the transcription pre-initiation complex (PIC)[78][79], an ensemble of transcription factors and RNA polymerase. TFs have a DNA binding domain (DBD) through which they interact with a response element (RE) close to the gene that they regulate.

The Glucocorticoid Receptor (GR) is a transcription factor involved in activating as well as repressing gene expression. The GR protein itself is activated by the hormone cortisol[80]. In the absence of hormone, GR is part of a complex including heat shock proteins hsp70 and hsp90 and resides in the cytosol[81][82]. Upon activation GR is released from the complex and translocates via active transport to the nucleus[83]. Depending on the cell

type and presence of other TFs, the GR either binds as a homodimer directly to DNA and transactivates gene transcription, or complexes with other TFs to repress or downregulate the genes these TFs would transactivate[84][85].

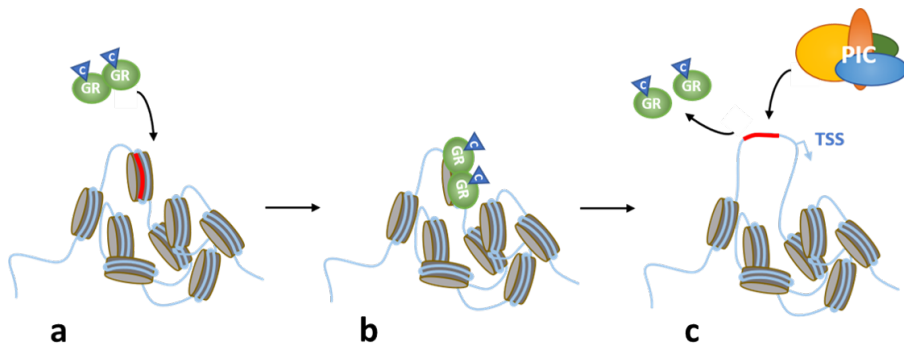


FIGURE 1.9: **Pioneering factors like the glucocorticoid receptor unwrap compacted DNA to initiate transcription.** a) GR prefers to bind to a GRE (red) positioned in nucleosomes. b) As a homodimer, GR is able to bind its response element without other TFs. c) After unwrapping the nucleosome by competing with the histone core, GR detaches and the pre-initiation complex (PIC) moves in to start transcription at a nearby transcription start site (TSS, blue arrow).

Although these two interaction modes of GR are described most often in literature, there is also evidence GR is able to interact with DNA in its monomeric form[86], as a heterodimer with other corticoid receptors[87][88], or even as a tri- or tetramer[89][90]. *In vitro* experiments by Wrangé have shown that GR's affinity for its response element (GRE) is higher when positioned in a nucleosome compared to bare DNA[91][92]. Other *in vitro*, *in vivo* and *in silico* studies have shown the GRE is usually found near the exits of nucleosomes[93][94] and the GR prefers GREs in the minor grooves of wrapped DNA[95]. These findings support the role of GR as a pioneering factor, i.e. a transcription factor pioneering compacted DNA to find its GRE. The pioneering mechanism is depicted in figure 1.9; a dimer of two GR proteins recognizes the GRE in a nucleosome (figure 1.9a) and binds to it (figure 1.9b). By presumably out-competing the histones, the GR dimer unwraps the nucleosome, making the DNA available for the PIC. The GR detaches and transcription will start from the transcription start site (TSS) close to the GRE (figure 1.9c).

1.3 Single-molecule microscopy and Förster Resonance Energy Transfer (FRET) for nucleosome research

Methods such as crystallography, gel shift mobility assays, stopped-flow and bulk fluorescence have been used for years to investigate nucleosome structure, stability, conformation and dynamics[35][96][97][98][99][100]. Newer, single-molecule techniques have been developed more recently and provide an extra layer of information by visualizing characteristics of single molecules. These techniques are often a combination of confocal microscopy with low concentrations of the sample of interest. Fluorescent labels are excellent for following single molecules, as labelling and tracking of the signal are non-invasive techniques offering a high degree of accuracy[101][102]. An additional fluorescence method often used in biology is Förster Resonance Energy Transfer (FRET), which provides conformational information at nanometer scale and has proven itself in recent years in nucleosome dynamics research[98][99][103]. Labelling a nucleosome as depicted in figure 1.10a allows for tracking nucleosome breathing in burst experiments combined with alternating laser excitation (ALEX) where fluorophores are excited by alternating light pulses at microsecond timescale (figure 1.10a) to generate timetraces such as those in figure 1.10b. In experiments performed by Koopmans et al.[53] the concentration of nucleosomes was lowered to be able to distinguish single-molecule burst events. These bursts were characterized by their label stoichiometry S and FRET efficiency E [refs] and plotted in an E, S -histogram (figure 1.10c) to assess the equilibrium between closed ($E > 0.25$) and open ($E < 0.25$) nucleosomes ($S > 0.2$ and < 0.8). Timetraces from burst experiments were also used to determine the difference in diffusion time for closed and open nucleosomes; correlation curves shown in figure 1.10d were obtained by correlating photon arrival times assigned to closed or open nucleosomes. As depicted, closed nucleosomes diffuse faster (curve shifts to smaller τ) than (partially) open nucleosomes. Burst experiments done by Buning et al.[104] have shown this method is so accurate one is able to distinguish the difference in compaction as measured by FRET efficiency through elongating one of the nucleosomes' DNA exits (figure 1.10e-f).

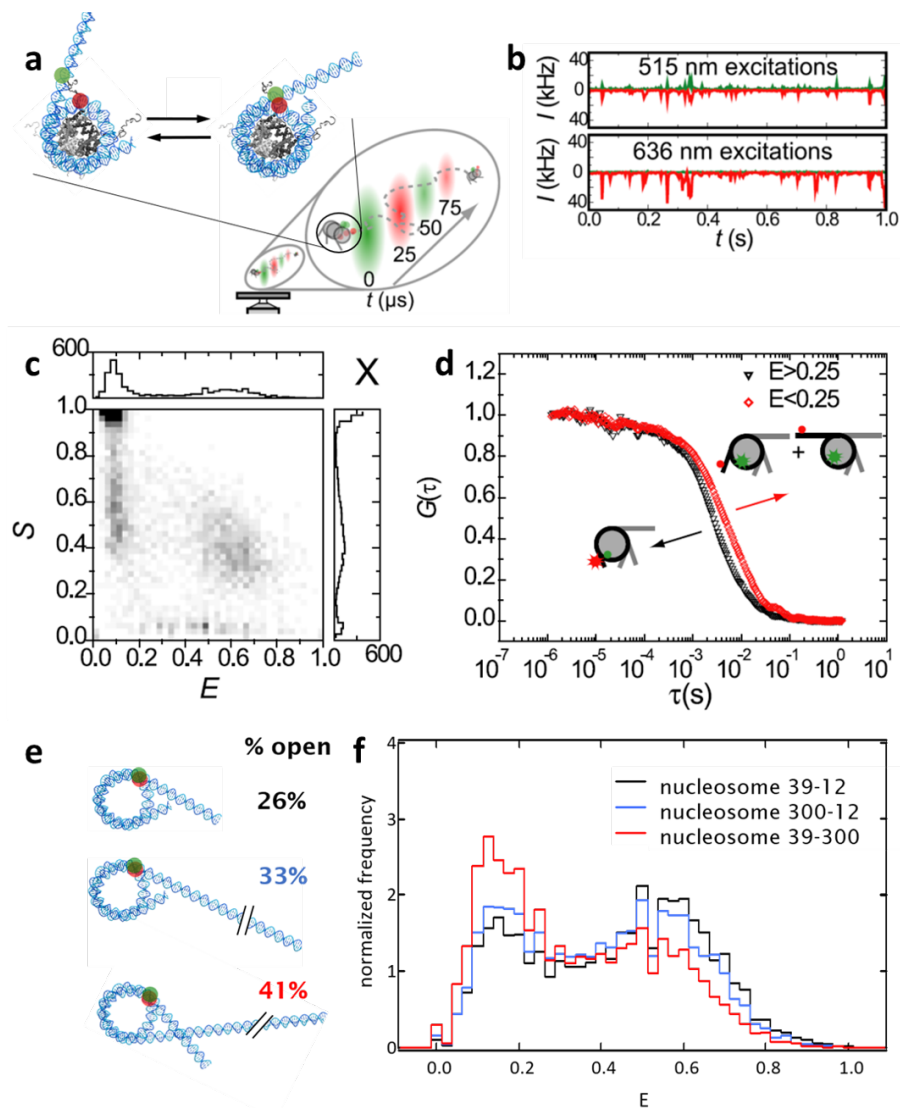


FIGURE 1.10: Alternating laser excitation (ALEX) combined with FRET and nanomolar concentrations in a confocal microscope gives conformational information of the nucleosome on a single-molecule level. a) Nucleosomes were labeled with FRET pair Cy3B-Atto647N. At nanomolar concentrations single nucleosomes diffuse through the confocal spot. b) The diffusion of single molecules generates timetraces of burst events. When a nucleosome comes through the focus in a closed state, both green and FRET emissions are detected (upper timetrace). *caption continues on next page*

1.4 Scope of this thesis

The next chapters revolve around the nucleosome, our unit of interest. We have investigated and quantified when possible the effects of different attributes of the nucleosome itself, as well as the effects of interactors with the nucleosome, focusing on the dynamics, accessibility and stability of the nucleosome. In chapters 2 and 3 we elaborate on the optical, analytical and biological tools we have used and developed to successfully perform experiments sensitive enough to visualize these effects. Both chapters conclude with validations of the methods from experiments.

In chapters 4, 5 and 6 we combined several fluorescent techniques such as fluorescence correlation spectroscopy, spFRET and burst analysis to resolve nucleosome dynamics and binding affinity of different proteins to DNA and nucleosomes. By combining these techniques we have quantified the interactions in and with the nucleosome. In chapter 4 we show the effects of changes in DNA sequence, linker DNA and buffer composition on nucleosomes. We have elucidated how changing a few base pairs near the DNA exit or changing the number of base pairs of linker DNA of a nucleosome alters nucleosome stability and dynamics. In chapter 5 we quantified the effect of histone posttranslational modification H3K36me3 on nucleosome stability and dynamics. We also showed how this PTM affects the affinity of the LEDGF/p75 protein for nucleosomes. Chapter 6 shows how an ensemble of proteins from an extracted nucleus containing an activated and labeled transcription factor GR interact with bare DNA and nucleosomes.

FIGURE 1.10: *Caption figure 1.10 continued:* **c)** Bursts were characterized by FRET efficiency (E) and label stoichiometry (S) and plotted in histogram format, showing two populations ($E < 0.25$ and $E > 0.25$) for $0.2 < S < 0.8$, representing open and closed nucleosome, resp. **d)** Arrival times of photons assigned to bursts of open and closed nucleosomes were correlated to generate (auto)correlation curves, showing closed nucleosomes diffuse faster (black curve) than (partially) open nucleosomes (red curve). **e)** and **f)** Addition of free linker DNA drives nucleosomes to the open state. Noticeable is the difference in FRET distribution for 39-300 compared to 300-12; not only is the closed state less populated (59% vs. 67%) it is also less closed (lower $\langle E \rangle$). Figures adapted from Koopmans et al. 2009 and Buning et al. 2015.



**METHODS AND ADVANCES IN SINGLE-MOLECULE
FLUORESCENCE MICROSCOPY AND
SPECTROSCOPY**

2.1 Introduction

Experimental investigations in the life sciences have traditionally been performed on a population level[105][106]. Analysis of the ensemble average of molecular properties results in loss of information concerning molecular heterogeneity, and may ultimately lead to misinterpretations of the underlying physiological relevance of subpopulations of molecules. Focusing on molecules as the minimal 'functional' units in a biological system, single-molecule biophysics research has an important impact on a range of fields of biological investigation[107].

The true workhorse of the single-molecule methods is fluorescence microscopy. It is a widely-used, and low-invasive method, allowing the biomolecule to remain in an *in vivo* environment. Maintaining *in vivo* conditions saves most, if not all functionality of the biological system. Moreover, fluorescence microscopy methods allow access to useful measurable parameters on time and length scales relevant for the biomolecular processes[106][108].

Wide-field microscopy is how single-molecule microscopy is most easily achieved nowadays. However, confocal imaging has the advantage of less background signal. The principle of confocal imaging has been developed in the 1950's and overcomes several limitations of traditional wide-field fluorescence microscopy. In a conventional microscope, the entire specimen is illuminated evenly. As all parts of the sample in the optical path are excited at the same time, the resulting fluorescence includes a large unfocused background part. In contrast, a confocal microscope uses point illumination and a pinhole in the optically conjugate plane in front of the detector to eliminate out-of-focus signal (fig. 2.2a). The resolution, particularly in the sample depth direction, is much better than that of wide-field microscopes. Scanning the focused beam produces images with resolution close to the Abbe limit in scanning confocal microscopy (SCM)[109][110][111].

To quantify conformational changes of single molecules or interaction between molecules of length scales below the diffraction limit one can revert to super-resolution techniques in which the center of mass of individual molecules is determined[112][113]. However, the limited number of photons, together with background signal, typically limit the accuracy to several 10's of nanometers. For even better accuracy, one can revert to the non-radiative energy transfer between two fluorophores known as FRET

(Forster or Fluorescence Resonance Energy Transfer). FRET can resolve distances of 2-10 nanometers, making it very suited for resolving conformations of and interactions between biomolecules[114][115][116][117].

Though scanning is time consuming, the temporal resolution of the detection of photons can be sub-nanoseconds. Fluorescence correlation spectroscopy (FCS) highlights the temporal rather than the spatial resolution and computes the correlation times of the fluorescence, revealing the mobility of single molecules as well as time constants that characterize the photophysics of the fluorescent molecules[118][119][120][121][122]. When FRET is resolved at the single-molecule level, referred to as single-pair FRET (spFRET), an additional advantage over ensemble measurements comes up: it is possible to track the dynamics of conformational changes, or molecular interactions, even when they proceed stochastically, which most biomolecular processes do. Here we will focus on using spFRET to reveal conformational changes in nucleosomes. We will also address fluorophore choice and setup calibration, data handling and post-fit corrections necessary to obtain reliable data.

2.2 Methods and materials

2.2.1 FRET

Förster's Resonance Energy Transfer (FRET), named after Theodor Förster for first describing the phenomenon, is the energy transfer between two molecules by resonance. The mechanism of FRET can be described as the quantum analog of classically coupled mechanical oscillators. When the electronic states of two molecules are in phase, the energy of the first molecule transfers in a non-radiative way to the second molecule, promoting it from ground state to excited state (figure 2.1). When both molecules are capable of fluorescence, FRET is dubbed Fluorescence Resonance Energy Transfer. Note that the energy transfer is not through fluorescence.

The strength of this dipole-dipole interaction depends on the inter-molecular distance:

$$E = \frac{1}{1 + \left(\frac{R}{R_0}\right)^6} \quad (2.1)$$

where R is the distance between donor and acceptor molecules and R_0 their Förster radius. The FRET efficiency E is derived from the intensities of the

donor and acceptor fluorescence, as we will show in later sections.

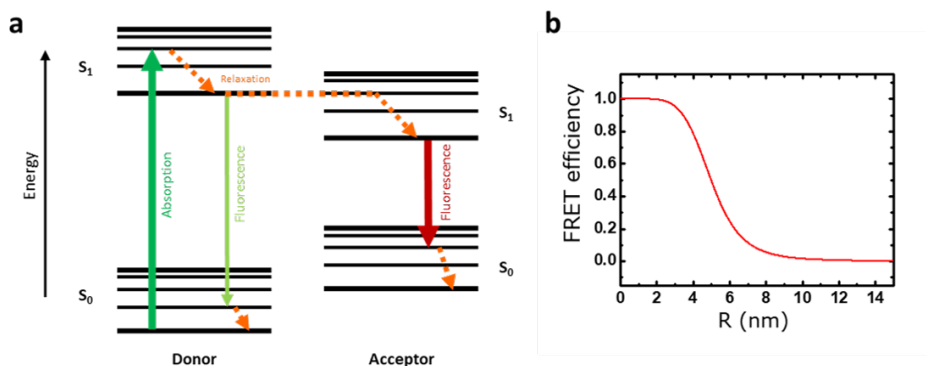


FIGURE 2.1: **Mechanism of FRET at the nanometer scale.** **a)** A Jablonski diagram of FRET, depicting the energy transfer, which only occurs when electronic singlet states S_0 and S_1 are in close proximity. **b)** FRET efficiency as a function of distance R . FRET efficiency E is 50% at characteristic distance R_0 .

2.2.2 Choice of fluorophores

The right choice of fluorophores for single-molecule experiments is paramount; in order to follow a molecule, whether its diffusion or conformational dynamics, one needs a good signal of the fluorophore tagged to the molecule. Fluorophores need to be stable emitters (no bleaching), and their emission should be stable over time, i.e. minimal transitions into dark triplet states ($S_1 \rightarrow T_1$) should occur. Moreover, the fluorophore should have a high emission efficiency (quantum yield). For FRET, to follow dynamics, there should be sufficient spectral overlap between the emission of the donor fluorophore and the absorption of the acceptor fluorophore.

Two fluorophores qualifying this description are Cy3B and ATTO647N (fig. 2.4). Cy3B is a cyanine dye (synthetic polymethines) with a higher quantum yield (0.67) than its siblings Cy3 (0.15), Cy5 (0.27) and Cy7 (0.28)[123]. The high quantum yield is because Cy3B is not capable of cis-trans isomerization around the polymethine group, which can lead to loss of fluorescence after excitation. As a result, Cy3B is not subject to photo-isomerization and is both extremely bright and stable[124].

ATTO647N is derived from carbopyronin and also has a rigid structure, making cis-trans isomerization impossible. It is one of the brightest and

most photostable dyes available. Contrary to Cy5, ATTO647N remains stable in salt buffers and has a high ozone resistance. Cy3B and ATTO647N are an optimal FRET-pair; they have a Förster radius of 6.2 nm, one of the longest radii available at the moment[125][126].

In this thesis nucleosomes were labelled with Cy3B and Atto647N for following breathing dynamics. When quantifying protein binding affinity, DNA and nucleosomes were only labelled with ATTO647N, and proteins were labelled with fluorophores in excitation and emission spectra similar to Cy3B. Although these fluorophores, such as EYFP and ATTO532, are spectrally similar to Cy3B, they have distinct structural and functional features. EYFP is the Enhanced Yellow Fluorescent Protein and is a derivative of GFP, a naturally occurring fluorescent protein. As such, it can be fused into the vector DNA, transcribed, translated and genetically tagged to a protein, resulting in a population of proteins that is completely labelled. The downside of using Fluorescent Proteins for single-molecule studies, especially the YFP's, is their limited optical stability, a phenomenon known as flickering[127]. Such prolonged residence in a dark triplet state can last micro- to milliseconds. In organic fluorophores this relaxation process is much faster (sub-microsecond) and is called blinking. As diffusion times and lifetimes of different conformations are typically in the order of milliseconds, flickering can obscure events. EYFP does have a high quantum yield: 0.60[128].

ATTO532 is a carboxy-derived fluorophore like ATTO647N, and has excellent photostability. It is a strong absorber, has a very high quantum yield (0.90), remains stable in a wide thermal range and has excellent water solubility[129]. These characteristics make ATTO532 a good choice for protein labelling. ATTO532 and ATTO647N form a FRET pair with a Förster radius of 5.1 nm[130].

An other important feature to take into account when doing fluorescence microscopy is the size of the fluorophore. Many fluorescence-based methods to follow interactions rely either explicitly (FCS, stopped-flow cytometry) or implicitly (SCM, TIRFM) on (differences in) diffusion of proteins, DNA or nucleosomes. Organic dyes compare favourable in this respect. ATTO dyes are ~ 2 nm long and have molecular weights of 0.8 - 1 kDa. Cy dyes are even smaller; Cy3B has a length of 1.4 nm[131] and weighs 0.6 kDa. Fluorescent proteins are large compared to ATTO and Cy dyes. The chromophore of the protein is only 1 nanometer long, but the rest of the protein is more than 4 nm long and has a diameter of 3 nm (fig. 2.2b). Its molecular

weight is 27 kDa[132]. This results in a larger hydrodynamic radius, when a biomolecule is tagged with the fluorophore, leading to larger diffusion constants. Moreover, the added structure may sterically hinder interactions

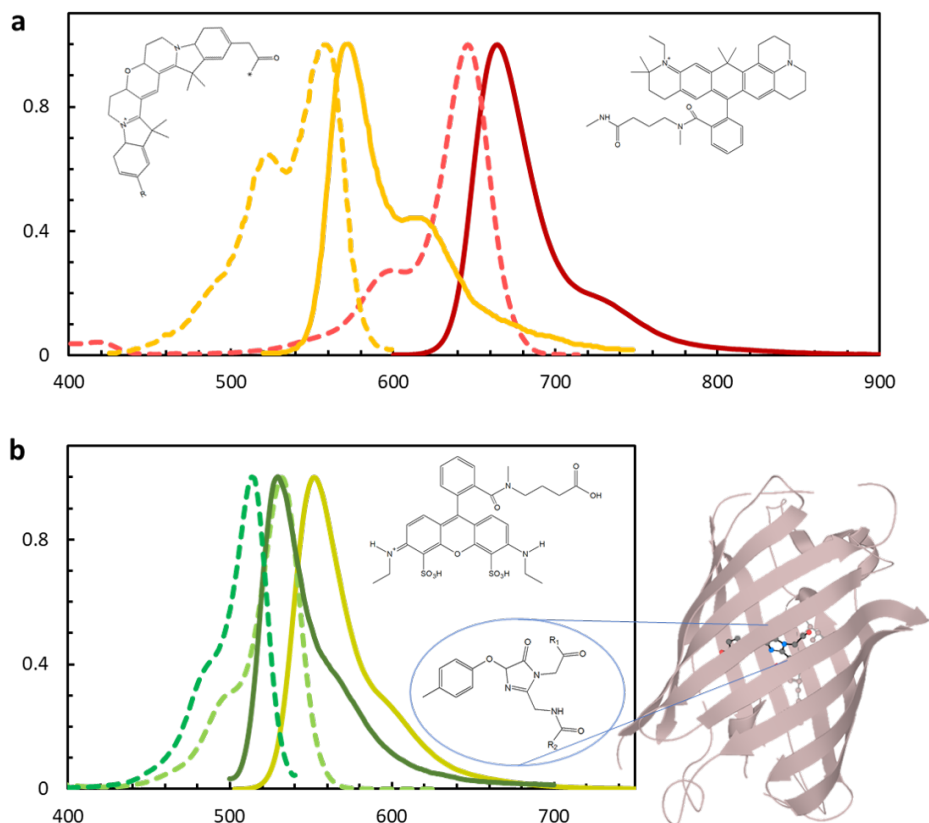


FIGURE 2.2: Excitation and emission spectra of fluorophores and FRET pairs used in this thesis. a) Excitation and emission spectra, as well as molecular structures of FRET pair Cy3B (left molecule, orange curves) and ATTO647N (right molecule, red curves). **b)** Molecular structures and excitation and emission spectra of ATTO532 (top molecule, darker green curves) and EYFP (bottom and right molecule, moss green curves). It should be noted that, even though EYFP emission and ATTO647N excitation spectra partial overlap, due to the large size of EYFP, FRET was not observed.

between or conformational changes within molecules. Finally, the chemical

properties of the fluorophore may induce aggregation of the biomolecules. Though we will not use the FRET efficiency to deduce absolute distances in this thesis, one should be aware that locking the orientations of the dyes may affect the FRET efficiency, and may lead to its own dynamics. However, we are not aware that this is significant in the results we present here.

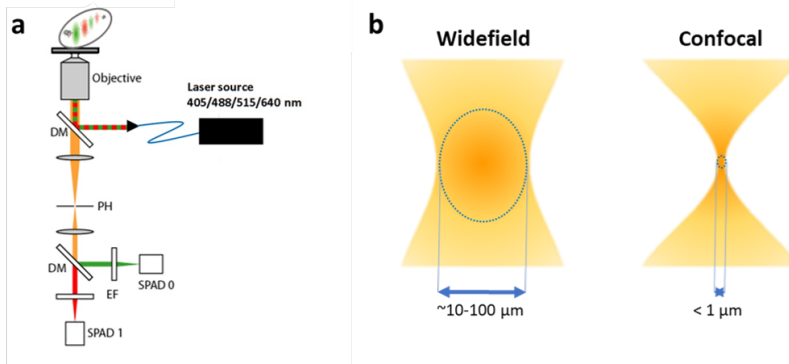


FIGURE 2.3: **Confocal microscopy reduces illuminated volume by orders of magnitude compared to widefield microscopy.** **a)** graphic depiction of the confocal microscope setup; the excitation beam from the laser is collimated and reflected by dichroic mirror 1 (DM1) into the objective. Fluorescence passes through DM1 and is focused onto pinhole PH. Next, the signal is collimated and wavelengths shorter than 640 nm are reflected by DM2 (640dcxr), filtered and focused onto SPAD 0 (Green photodiode). Wavelengths longer than 640 nm are directed to SPAD 1 (Red photodiode). **b)** Visualization of the difference in light collimation between widefield and confocal microscopy.

2.2.3 Confocal microscope setup

Measurements were performed on a home-built confocal microscope as depicted in figure 2.7 equipped with a 60x water-immersion objective (NA 1.2, Olympus). An ICHROME MLE-SFG laser was used as an 514 nm and 632 nm excitation source. From an optical fiber a collimated excitation beam was directed through the objective and focused 25 μm above the glass-sample interface. The excitation power was in the order of 5 μW . The collected fluorescence was focused with a 15mm tube lens (ThorLabs) and spatially filtered with a 50 μm pinhole. After collimating the beam with a 15mm lens (ThorLabs) it was split by a dichroic mirror (640dcxr, Chroma). The two emission beams were further filtered (hq570/100nm

and hq700/75m, respectively) and imaged on the active area of Single Photon Avalanche Photodiodes (SPADs, SPCM AQR-14, Perkin Elmer) using a 10mm lens (ThorLabs). The photodiodes were read out with a TimeHarp 200 photon counting board (PicoQuant). The acquired data was stored in time-tagged to time-resolved data files (*.t3r), which were further processed with a home-built Python program to read out the photon data according to arrival time and SPAD channel.

2.3 Single-molecule burst microscopy

Though it is not possible to discriminate acceptor fluorescence from direct excitation and FRET, one can intermittently use different different excitation wavelengths to check for the presence of both fluorophores. For Alternating Laser EXcitation (ALEX)-spFRET measurements, biological samples were diluted to picomolar concentrations to ensure that only one molecule is in focus during the bin time of 1 millisecond. Light pulses of 514 and 632 nm, each 25 microseconds long, were used to excite either the

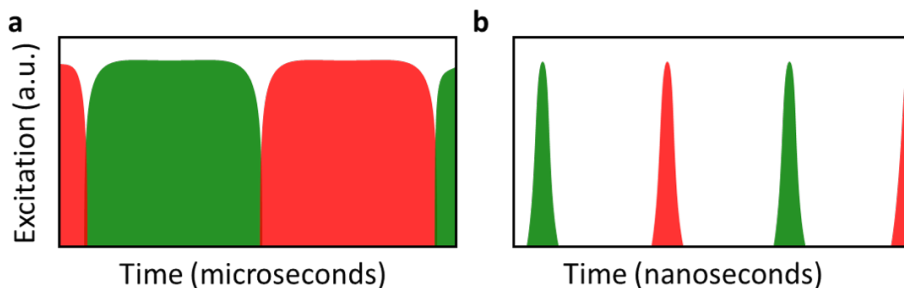


FIGURE 2.4: **Major differences between ALEX and PIE are timescale as well as partial pulse overlap due to equipment.** **a)** Alternating Laser EXcitation entails consecutive laser pulses at microsecond scale. **b)** Pulsed Interleaved Excitation means sub-microsecond pulses, separated by dark periods. These dark periods also assure pulses do not partially overlap.

acceptor fluorophore (632 nm) or the donor (514 nm). Pulsed Interleaved Excitation (PIE) is a similar technique of alternating several laser pulses of different wavelengths but with dark periods at a sub-microsecond timescale. This allows for almost simultaneous recording of the temporal behaviour. For our FCS analysis, FRET pair Cy3B-ATTO647N was excited with 100

ns pulses of wavelengths 514 and 632 nm, separated by intermittent dark periods of 300ns (figure 2.4b). These dark periods prevent residual temporal leakage of the laser.

2.3.1 ALEX-spFRET burst analysis

As the diffusion time of the proteins, DNA and nucleosomes used in our experiments were ~ 100 times slower than the pulse cycle of 50 microseconds, emitted photons from different excitation wavelengths were detected as quasi-continuous bursts in the two detectors. A single burst was defined as a series of at least 50 photons of any color, with an inter photon-photon time less or equal to 100 microseconds. The number of photons in each channel was used to calculate the stoichiometry of the fluorescent labels (S) and the FRET efficiency (E). E and S were plotted in an E, S -histogram as shown in Figure 4.1b.

The approximate stoichiometry and FRET efficiency were defined as

$$E^{raw} = \frac{I_{514}^R}{I_{514}^R + I_{514}^G} \quad (2.2)$$

and

$$S^{raw} = \frac{I_{514}^R + I_{514}^G}{I_{514}^R + I_{514}^G + I_{632}^R} \quad (2.3)$$

where I_{514}^G is the signal on the green APD during 514 nm excitation, I_{514}^R acceptor emission after donor excitation and I_{632}^R the intensity of acceptor emission after acceptor excitation. Stoichiometry S discriminates the populations of molecules labeled with both fluorophores ($0.2 < S < 0.7$), from molecules labeled with either the donor ($S > 0.7$) or the acceptor fluorophore ($S < 0.2$).

The FRET efficiency and stoichiometry were corrected for several effects. The intensity of the background was subtracted from each burst, taking into account duration τ_b of the burst:

$$I^D = I_{514}^G - \tau_b \cdot i_{514}^G,$$

$$I^A = I_{632}^R - \tau_b \cdot i_{632}^R$$

Depending on the donor fluorophore, a significant portion of the donor emission can leak into the acceptor channel. This phenomenon is called spectral leakage (α), and was calculated as

$$\alpha = \frac{E_{Donly}}{1 - E_{Donly}}$$

where E_{Donly} was determined by taking the mean FRET efficiency of the bursts where $S > 0.7$ (nucleosomes labeled with only donor fluorophore). Direct excitation of the acceptor fluorophore during donor excitation was calculated as

$$\delta = \frac{S_{Aonly}}{1 - S_{Aonly}}$$

with S_{Aonly} the mean stoichiometries of the population of bursts for $S < 0.2$. Finally, parameters α and δ were used to correct I_{514}^A and determine I^F :

$$I^F = I_{514}^A - \alpha \cdot I^D - \delta \cdot I^A$$

I^F represents the signal where the emission of the acceptor during donor excitation was only due to FRET. After these corrections a more accurate FRET efficiency and stoichiometry can be defined:

$$E^{pr} = \frac{I^F}{I^F + I^D} \quad (2.4)$$

and

$$S^{pr} = \frac{I^F + I^D}{I^F + I^D + I^A} \quad (2.5)$$

The last correction factor, γ , is to account for differences in quantum yield, excitation intensity and detection efficiencies of the donor and acceptor and can be calculated from tabulated or independently measured parameters. It can also be determined experimentally from the relation between E^{pr} and S_{pr}^* post-hoc. When fitting $\frac{1}{S_{pr}^*} = m \cdot E^{pr} + c$, γ is defined as $\frac{c-1}{c+m-1}$. The fully corrected FRET efficiency and stoichiometry are then computed as

$$E = \frac{I^F}{I^F + \gamma \cdot I^D} \quad (2.6)$$

and

$$S = \frac{I^F + \gamma \cdot I^D}{I^F + \gamma \cdot I^D + I^A} \quad (2.7)$$

We used the FRETbursts toolkit developed by Ingargiola et al.[133] to calculate E and S and to generate E,S -histograms.

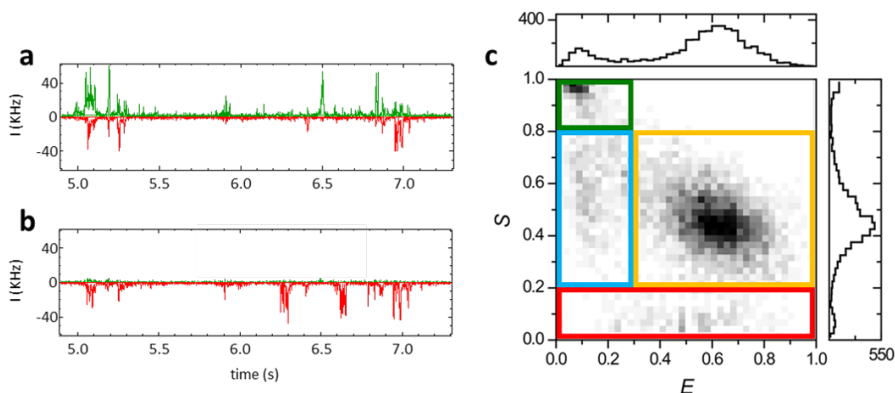


FIGURE 2.5: E,S histograms are derived from single bursts in emission channels. **a)** and **b)** the emission channels after green excitation (a) and red excitation (b). The signals were binned at 1 ms. **c)** The E,S histogram resulting from summing the photons from individual bursts shows the signal consisted of different populations of single- and double-labeled species; in the green rectangle is the population of molecules only labeled with the donor fluorophore, in red only labeled with the acceptor. Blue is the double-labeled population exhibiting no/low FRET, orange the double-labeled population showing high FRET.

2.3.2 Scanning Confocal Microscopy

Next to detecting freely diffusing molecules in a fixed focus, we used Scanning Confocal microscopy (SCM) to follow immobilized molecules over longer times than the diffusion time. The confocal setup as described in the previous section was used to perform scanning measurements combined with ALEX (figure 2.6a) to generate images as figure 2.6b. Laser intensities were $5 \mu\text{W}$ for both 514 and 632 nm excitations. The pixel frequency was 1 kHz (1ms per color) and the line scan rate was 100 Hz, so each pixel was excited 5 times with both colors. Piezo step resolution (P-517 3CD, Physik Instrumente) was 1 nm and travel range $100 \mu\text{m}$ for x,y direction. In figure 2.6b the pixel size was $250 \times 250 \text{ nm}$. Nucleosomes were immobilized on a PEG/biotinPEG-coated surface using a modified version of the protocol

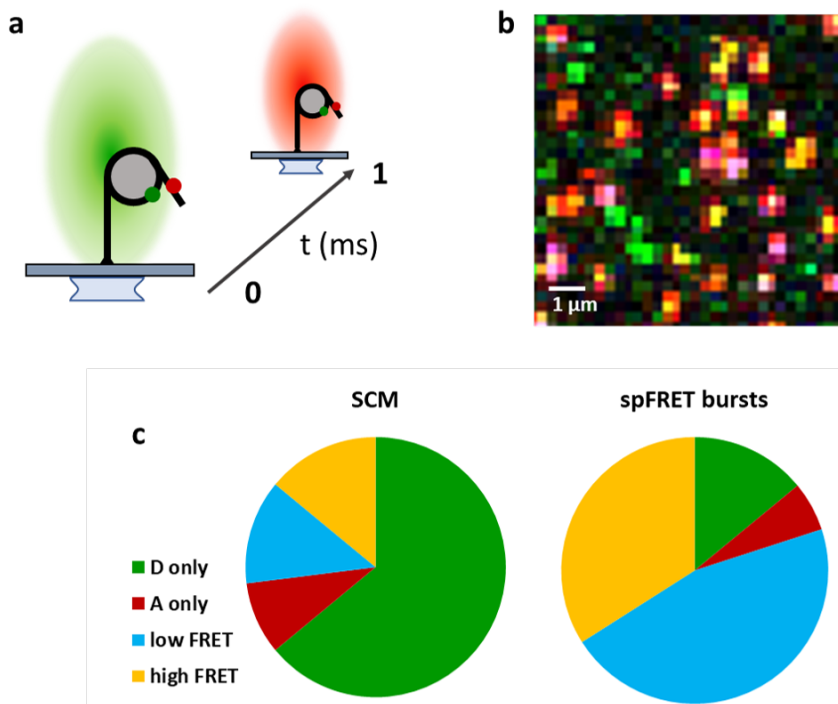


FIGURE 2.6: Immobilization and ALEX-scanning confocal microscopy visualizes nucleosome dynamics at millisecond timescale but bleaches acceptor fluorophore. **a**) Visualization of ALEX-scanning confocal microscopy. **b**) Nucleosomes ($N=35$) on a $72\mu\text{m}^2$ surface show some molecules spectrally overlapping, making it difficult to automatize detection and characterization. **c**) Comparing subpopulations of SCM ($N=200$) with spFRET ($N=8000$) shows a significant part of the acceptor fluorophores quenched. The main cause for this is likely the proximity of ATTO647N to the surface.

from Luo et al.[100]. The complete protocol is discussed in Chapter 3 of this thesis.

Examination of label stoichiometry and FRET efficiency of immobilized nucleosomes showed a significant effect of immobilization on the ratio of populations (figure 2.6c). Although an oxygen scavenger system as well as a photobleaching reductor (Trolox) were added, scanning immobilized nucleosomes showed 64% of the acceptor fluorophores was quenched or bleached, compared to 14% in spFRET burst experiments. The donor fluorophore appeared more resilient, as only 6% (burst) to 9% (SCM)

of nucleosomes was classified as acceptor-only population. Nucleosomes containing both fluorescent labels made up 80% of the total population when freely diffusing compared to only 27% when immobilized. The ratios between low and high FRET were similar; 46% and 34% or 3:2 for spFRET bursts against 13% and 14% or 1:1 for scanning confocal. It is important to note that nucleosomes were selected manually for SCM, as our search algorithm was unable to distinguish between molecules too close to each other. Because homogeneous molecule dispersion could not be attained by altering nucleosome concentration or other steps of the immobilization protocol we did not further use SCM to investigate nucleosome dynamics and nucleosome-protein interactions. These results do show an important benefit of burst-analysis or FCS compared to SCM of immobilized molecules: the limited duration of excitation relieves bleaching effects and allows for higher excitation and emission rates, even in absence of oxygen scavenger and triplet state quenchers.

2.4 Fluorescence Correlation Spectroscopy

Having labeled molecules diffuse through the focus causes the intensity of the fluorescent signal to fluctuate in time. In Fluorescence Correlation Spectroscopy (FCS) these fluctuations are used to determine the concentration, diffusion constant and when possible dynamical properties of molecules. The fluctuations in intensity are analyzed by correlating photon arrival times over increasing time-lag τ :

$$G(\tau) = \frac{\langle \delta I_1(t) \cdot \delta I_2(t + \tau) \rangle}{\langle I_1(t) \rangle \cdot \langle I_2(t) \rangle} \quad (2.8)$$

To assess the diffusion of a molecule, photon arrival times of one channel are correlated to generate an autocorrelation curve ($I_1 = I_2$). The correlation function that fits the diffusional part of a autocorrelation curve is formulated in terms of the concentration and diffusion time of the population of molecules labeled with the same fluorophore, taking into account the confocal volume:

$$G_{diff}(\tau) = N^{-1} \cdot (1 + \tau/\tau_D)^{-1} \cdot (1 + a^{-2} \cdot \tau/\tau_D)^{-1/2} \quad (2.9)$$

where τ_D is the diffusion time and N the average number of molecules in the confocal volume. Parameter a is the ratio between the axial and radial size of the confocal volume. The value of a for the setup used for the measurements presented here was determined through calibration experiments to be 8. The diffusion time τ_D of a molecule is determined by its size and the viscosity of the solvent η . The parameter used to express the size of a molecule is its hydrodynamic radius r_H and can be obtained using the Stokes-Einstein equation:

$$r_H = \frac{k_B T}{6\pi\eta D} \quad (2.10)$$

where diffusion constant $D = \frac{w^2}{4\tau_D}$ with k_B the Boltzmann constant, T temperature and w the radius of the confocal spot in the radial (x,y) direction. Equation 2.10 shows the hydrodynamic radius scales proportional with diffusion time, implying that larger molecules move slower through the focus. This property was used to analyze correlation curves constructed from signals of molecules of different sizes. If we assume the molecule to have a spherical shape, the radius scales with the molecular mass as $r_H \propto M^{\frac{1}{3}}$. In practice this means for the diffusion time to increase two-fold, the mass of a molecule needs to increase a factor of 8.

To quantify the colocalization of two differently labeled molecules the signal of one molecule (I_1) is correlated with the signal of another molecule (I_2) to generate a crosscorrelation curve. Physical interpretation of the crosscorrelation functions requires additional calculations and will be discussed further on.

The Python module `pycorrelate` developed by Ingargiola et al.[133] was used to calculate all correlation curves. The correlation algorithm used in this module was developed by Laurence et al.[134]. The algorithm is based on rewriting the correlation as a counting operation on photon pairs and can be used with arbitrary bin widths and spacing (see figure 2.7).

2.4.1 Photophysics

Photophysics of the fluorophore, i.e. transiting to a triplet or dark state, as well as afterpulsing effects from the APDs need to be included in the fit of a correlation curve

$$G_{total}(\tau) = G_{diff}(\tau) \cdot G_{tr}(\tau) \cdot G_{ap}(\tau) \quad (2.11)$$

where the latter two terms are defined as

$$G_{tr}(\tau) = 1 + \left(\frac{F_{tr}}{1 - F_{tr}} \cdot e^{-\frac{\tau}{\tau_{tr}}} \right)$$

and

$$G_{ap}(\tau) = 1 + \left(\frac{F_{ap}}{1 - F_{ap}} \cdot e^{-\frac{\tau}{\tau_{ap}}} \right)$$

with F_{tr} , F_{ap} the fractions of molecules associated with either triplet state (**tr**) or afterpulsing (**ap**), and τ_{tr} , τ_{ap} their characteristic timescales. As fluorophore photophysics and afterpulsing take place on different timescales[135][136] sensible boundaries were set for fitting these parameters (see Table 2.1 for all parameter boundaries). Figure 2.7a-d shows how a correlation curve is built from the fluorescent signal, culminating in a curve fitted with $G_{total}(\tau)$. Note that PIE leads to additional modulations in the correlation curve at short delays. We therefore refrained from fitting AP in those cases.

2.4.2 Microscope calibration and corrections

Also for FCS we applied post-fit corrections to compensate for the contributions of spectral leakage, background intensity, the difference of confocal volume for different excitation wavelengths and missing part of signal due to pinhole mis-alignment[137][138][139][140][141]. Spectral leakage from 514 nm excitation to the Red APD was corrected as

$$I_{514R} = I_{514R+leak} - (c_{leak} \cdot I_{514G}) \quad (2.12)$$

and eliminates false-positive detection of FRET. c_{leak} is the parameter denoting the percentage of leakage and depends on the fluorophore. For Cy3B $c_{leak} = 0.11$, for Atto532 $c_{leak} = 0.03$ and for EYFP $c_{leak} = 0.15$.

Background photons increase the apparent number of molecules in solution through correlation of random/noise photons (which appear often) with photons from fluorophores (appearing rarely when in low concentration).

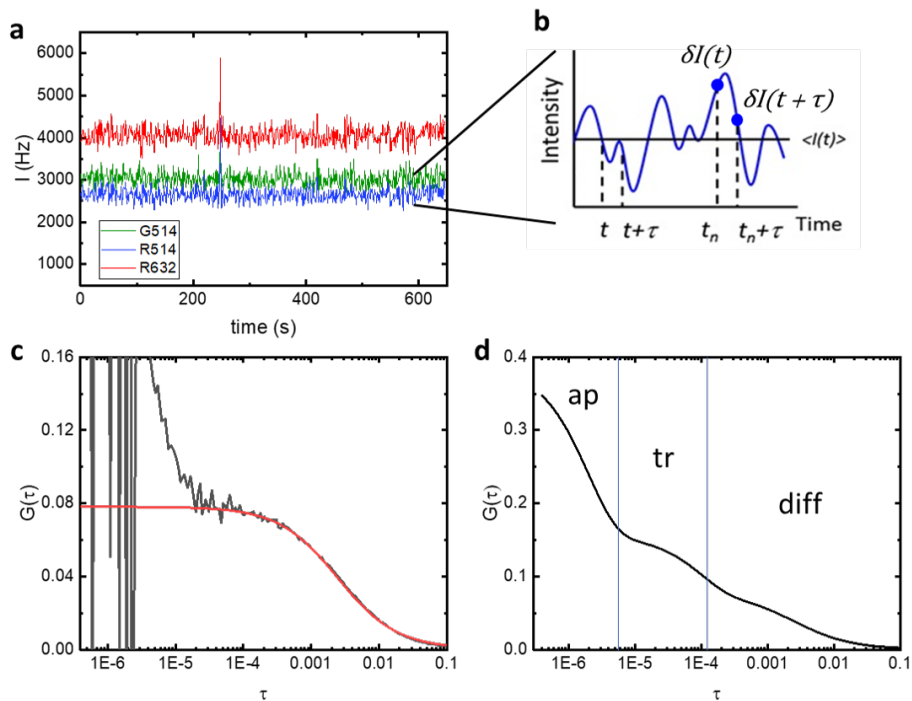


FIGURE 2.7: Correlation curves are built-up by correlating fluorescent signal at increasing time-lag. **a)** and **b)** Fluorescent signal from FCS-PIE measurements is correlated at time t at increasing time-lag τ , characterizing differences in intensity I over increasing timescales. **c)** Taking only the diffusion into account when fitting results in an overestimation of the number of particles, as fluorophores switching in and out of triplet state also contribute to the signal at the time scale of the fit's plateau. **d)** Visualization of the timescales at which diffusion (diff), triplet state photophysics (tr) and afterpulsing (ap) occur. It is shown that overlap of triplet state and diffusion decreases when diffusion time increases.

$$\begin{aligned}
N_{514G,bgcor} &= N_{514G} \cdot \left(\frac{I_{514G} - bg_{514G}}{I_{514G}} \right)^2 \\
N_{514R,bgcor} &= N_{514R} \cdot \left(\frac{I_{514R} - bg_{514R}}{I_{514R}} \right)^2 \\
N_{632R,bgcor} &= N_{632R} \cdot \left(\frac{I_{632R} - bg_{632R}}{I_{632R}} \right)^2
\end{aligned} \tag{2.13}$$

where bg_i is the number of background photons / dark counts on APD G or R during excitation with 514 or 632 nm light of solvent without fluorescent sample. The difference in confocal volume and pinhole alignment were corrected by introducing correction factors based on the number of molecules found in the 632R channel:

$$\begin{aligned}
N_{514G} &= N_{514G,bgcor} \cdot c_{ax514G} \\
N_{514R} &= N_{514R,bgcor} \cdot c_{ax514R} \\
N_{632R} &= N_{632R,bgcor}
\end{aligned} \tag{2.14}$$

Channel 632R was chosen because 632 nm excitation created a larger focal spot (i.e. larger axial radius) hence more emission than with 514 nm and alignment of the pinhole was more optimal for this channel. Table 2.1 and figure 2.8 show how correction factors were determined and used; figure 2.8a shows the apparent difference in concentration of TetraSpec beads (Invitrogen, no. T7279, $d \sim 0.1\mu m$) in different channels (after correction for background). Table 2.1 shows the results of using equations 2.13 and 2.14.

The same diffusion time, $t_D = 12.2 \pm 1.1$ ms, was found for all autocorrelations as well as for all cross-correlations. A DNA construct of 310 base pairs with fluorescent labels Cy3B and Atto647N placed 10 base pairs apart was constructed to provide a stable FRET signal. This construct, dubbed DNAFRET, was used to evaluate the effect of background contributions to the apparent number of molecules N as a function of the actual concentration C (figure 2.8c). Using equations 2.13 and 2.14 on a dilution series of DNAFRET from 30 nM to 60 pM shows in figure 2.8d that the contribution of background was properly corrected. Residual differences were attributed to incomplete double-labelling and photobleaching.

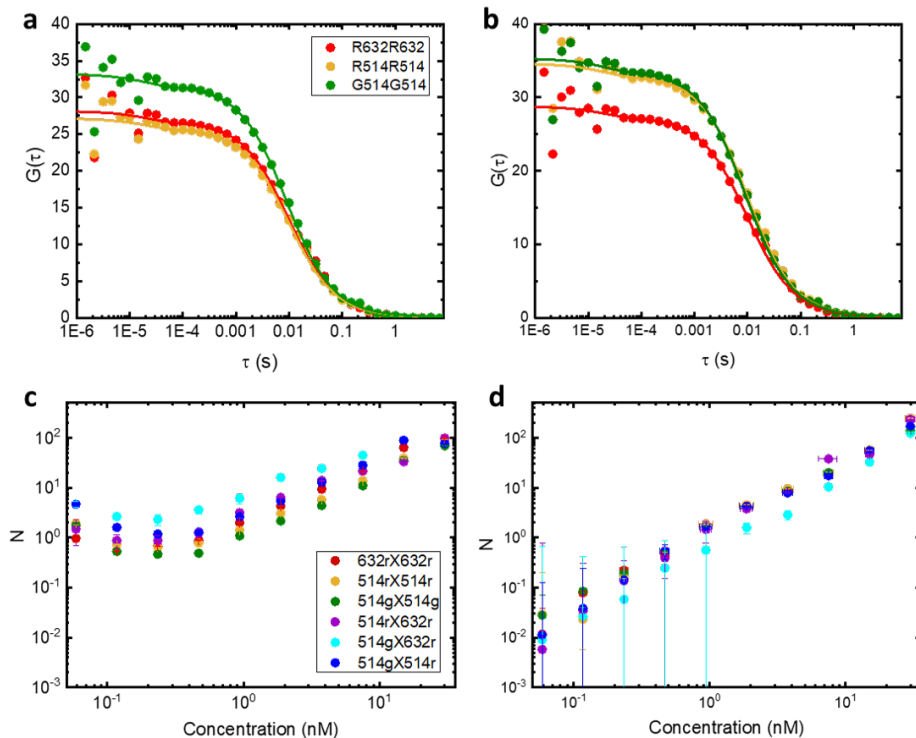


FIGURE 2.8: TetraSpec beads used to determine degree of spot overlap, titration of DNAFRET effect of background to false increase in number of molecules when concentration decreased. **a)** Autocorrelation curves for TetraSpec beads before and **b)** after correction for background. The resulting curves show the imperfect overlap between green (G514 and R514 curve) and red excitation spots. Also a small difference between donor emission from donor excitation (G514) and acceptor emission from donor excitation (R514) can be seen. For TetraSpec beads, R514 signal is not FRET but spectral leakage and shows the degree of overlap of the emission channels, which is nearly perfect (98%). **c)** Titrating DNAFRET from 30 nM to 0.05 nM. Below 1 nM the effect of background photons becomes visible. **d)** After background correction all channels, except for 514G632R, align. The underestimation of this outlier channel was also observed for TetraSpec beads and will be compensated in crosscorrelation fit corrections (next paragraph).

channel	bg (Hz)	I (Hz)	N_{bgcor}	c_{ax}
514G	42	896	0.0298 ± 0.0017	1.24
514R	23	212	0.0304 ± 0.0020	1.17
632R	24	886	0.0366 ± 0.0012	-

TABLE 2.1: **Calibration with TetraSpec beads shows partial focal spot overlap.** Beads were measured in PIE-mode for 1200 seconds.

2.4.3 Fluorescence Crosscorrelation Spectroscopy

Contrary to the value of $G(0)$ of an autocorrelation curve, the amplitude of a crosscorrelation curve scales proportionally with the concentration of molecules in complex. Additionally, the amplitude of the crosscorrelation curve represents the complex molecules as a percentage of the population of molecules present at a higher concentration[142], implying that G_{cc} is reduced when one or more of the concentrations of single labeled molecules are increased. This is illustrated in figure 2.9a and 2.9b where the crosscorrelation curve (blue) is only a fraction of the autocorrelation curve of the Atto647N label on DNA (red).

To calculate the real number of complexed molecules from the crosscorrelation curve, N_{CC} need first be corrected for background photons from both channels involved in the cross-correlation[139]:

$$N_{CC,corr} = \frac{N_{CC} \cdot (I_{514G} - bg_{514G}) \cdot (I_{632R} - bg_{632R})}{I_{514G} \cdot I_{632R}} \quad (2.15)$$

We have used channels 514G and 632R as an example as in this thesis I_{514G} corresponds to the signal of proteins (when labeled), I_{532R} with DNA or nucleosomes. In principle any two different channels (f.i. 514R and 632G) can be cross-correlated. We also need to take into account that confocal spots from different excitation wavelengths do not completely overlap. Not compensating for this incomplete overlap would mean underestimating the number of molecules in complex[141]. The actual number of molecules in a complex is then calculated as

$$N_{514Gx632R} = c_{over}^{-1} \cdot \frac{N_{514G} \cdot N_{632R}}{N_{CC,corr}} \quad (2.16)$$

where c_{over} is used to correct for the incomplete overlap. Calibration experiments with TetraSpec beads performed after each alignment of the setup showed $c_{over} = 0.9 \pm 0.03$, implying without correction $\sim 10\%$ of the number of molecules in complex would be missed. With the actual number of molecules in complex determined, the dissociation constant K_d is calculated as

$$K_d = \frac{[molecule1] \cdot [molecule2]}{[complex1 + 2]} \quad (2.17)$$

The dissociation constant is a measure of the binding affinity and is equal to the concentration of molecule 1 at which half of its available binding sites are occupied by molecule 2. Figures 2.9e and 2.9f show how high and low affinity binding look like in FCS.

2.4.4 Conformational dynamics

Often, the highest time constant in the auto/cross-correlation curve corresponds to the average diffusion time of the molecules contributing to the signal. From the diffusion time the hydrodynamic r_H and molecular weight M can be estimated[143] (eq.s 2.10 and 2.11). By extension it is possible to distinguish between molecules of different sizes combined in an correlation curve. A significant difference in the size or weight of a molecule ($2 \cdot r_H$ or $8 \cdot M$ for $2 \cdot \tau_D$) is required to be able to detect such a difference[144]. This means that small changes such ligand binding or conformational dynamics would not be detectable with FCS.

However, FCS can readily be used for the detection of kinetics occurring on scales much smaller than r_H . In fact, one of the first uses of FCS was to determine the interaction rates of ethidium bromide (EtBr) with DNA[145]. By dividing the correlation curve corresponding to the complex or bound DNA by the curve corresponding to both free and bound DNA the Magde group cancelled the diffusional component, generating a correlation curve exclusively built from molecules of EtBr and DNA associating or dissociation while traversing through the confocal spot. More recently Widom and Langowski showed the same method can be applied to follow nucleosome dynamics[146]:

$$G_{dyn} = \frac{G_{514R}}{G_{632R}} = C(\tau) \cdot \left(1 + K \cdot e^{-\tau(k_o+k_c)}\right) \cdot G_{tr} \cdot G_{ap} \quad (2.18)$$

With $K = \frac{k_o}{k_c}$, the equilibrium between open and closed nucleosomes described by the ratio between their opening (k_o) and closing (k_c) rates. Assuming equal diffusion times for open and closed nucleosomes, as assumed by Magde et al. makes the correction factor $C(\tau)$ equal to 1. However, previous experiments by Koopmans and Buning showed that closed nucleosomes diffuse significantly faster than open nucleosomes[53]. Therefore when calculating G_{dyn} we did not assume $\tau_D^{514R} = \tau_D^{632R}$ and included a correction, resulting in

$$C(\tau) = \sqrt{\frac{\tau_D^{632R} \cdot (\tau_D^{514R} + \tau)}{\tau_D^{514R} \cdot (\tau_D^{632R} + \tau)}} \quad (2.19)$$

Figure 2.9 shows the application of eq. 2.18 to data of molecules with (2.9-b,d, nucleosomes) and without (2.9-a,c, DNAFRET) internal dynamics. At first glance the correlation curves of DNAFRET (fig. 2.9a) and nucleosomes (fig. 2.9b) look very similar, as the two construct have very similar diffusion times. The only observable differences are in the apparent concentrations (height of the curves), which could be due to various other reasons than internal dynamics (or the lack thereof); to the untrained eye these two collections of curves could have originated from similar molecules. In order to determine internal dynamics accurately, we cut up a long measurement into smaller sets (subsets), correlated the smaller sets and calculated the average curves. This decreased effects of random noise from the signal, especially in the time range of diffusion and dynamics, as these characteristic times are unrelated to noise. In order to optimize the fits of the curves, we took the inverse of the standard deviation of a curve as the fits weighing factor. These tactics are independent of the time range, making the fitting algorithm flexible over a large time range, i.e. several magnitudes of molecule size.

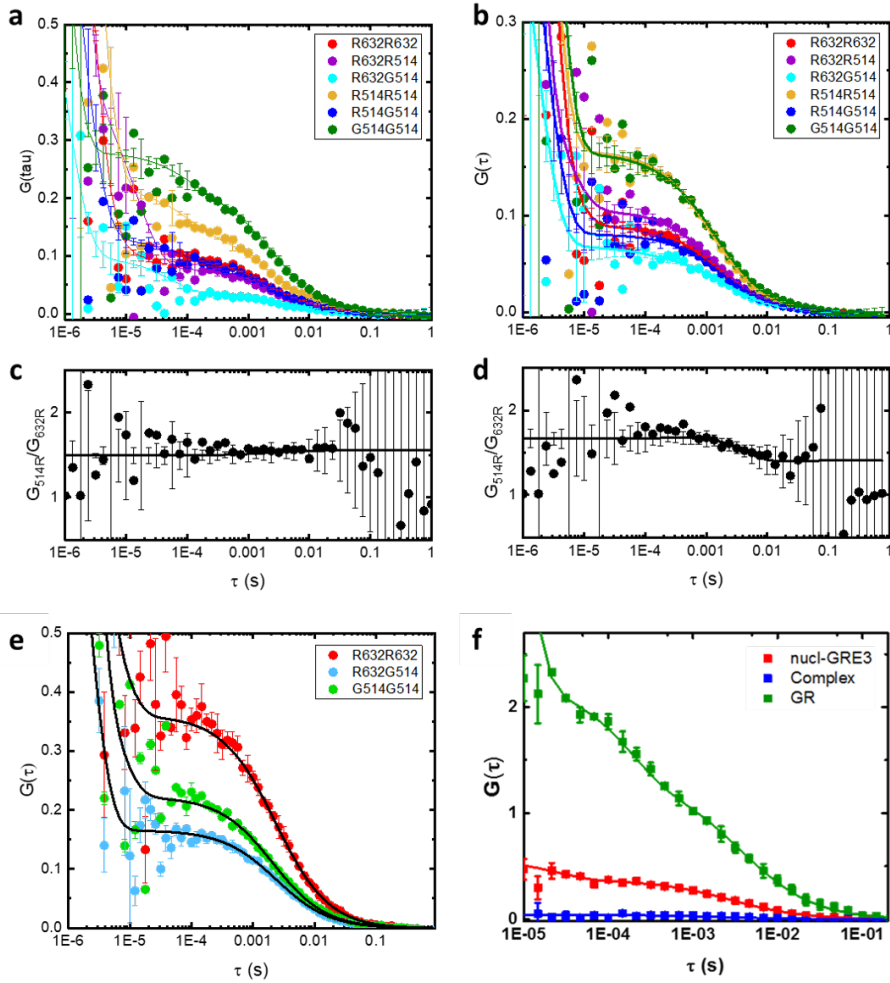


FIGURE 2.9: Dynamics and binding in FCS are often subtle effects on correlation curves and hence need to be extracted through additional analysis. a) and b) are correlation curves generated from signal DNAFRET and nucleosomes, respectively. Looking similar on first glance, DNAFRET displaying more particles in FRET channel, quantifying dynamics shows only nucleosomes (d)) switch between conformational states (K_{eq} for DNAFRET by fitting curve c) is $1.6 \cdot 10^9 \pm 6 \cdot 10^{17}$). e) Example of high affinity binding, observed in the crosscorrelation curve (blue) almost overlapping with the lowest autocorrelation curve. f) When binding is however (almost) absent, the crosscorrelation curve approaches $G(\tau) = 0$.

2.5 FCS data analysis

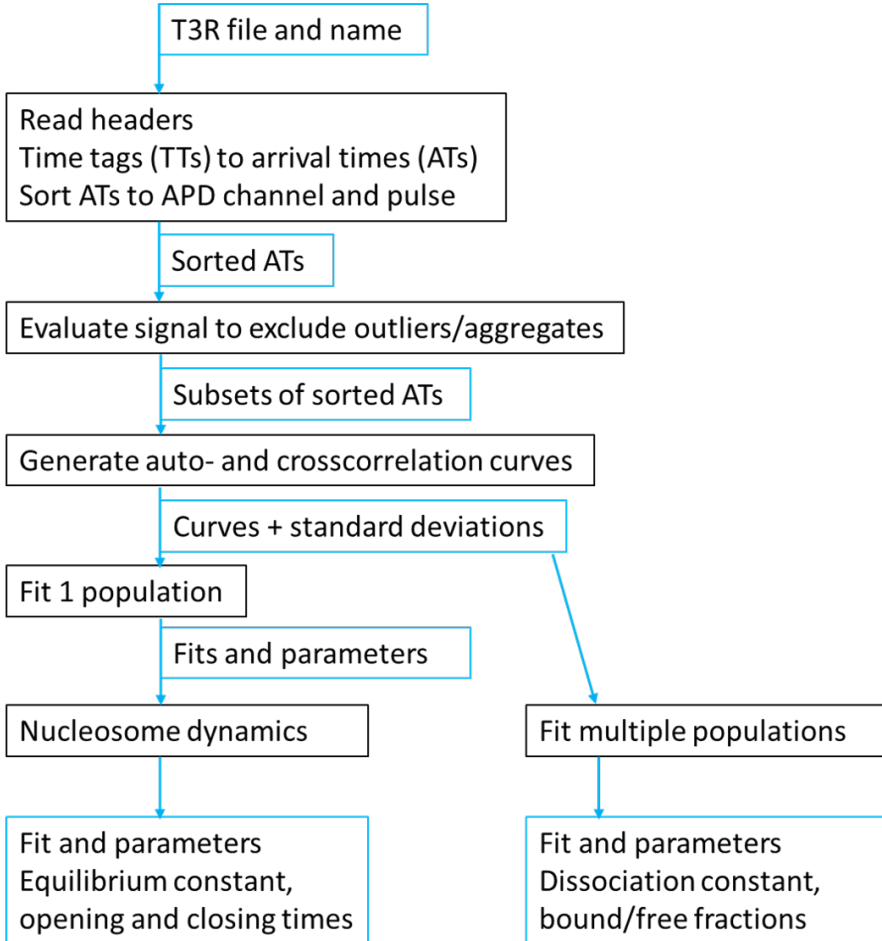


FIGURE 2.10: **Workflow of FCS data analysis.** Black boxes represent the parts of programs, in blue the data files and variables used as input and/or generated as output.

2.5.1 Data acquisition and processing

The signal generated by photons falling on the APD's during measurement was collected with a TimeHarp 200 (Time Measurement Histogram Accumulating Real-time Processor, software v. 6.1, Picoquant). The Time Resolved to Time Tagged (tttr or t3r) mode acquired signals at a 100 ns resolution, which was also the pulse length of our PIE experiments. Measurements were saved in a 32-bit t3r file which consisted of several header lines and t3r records. After reading the header the t3r records were read as followed: first 16 bits containing the timetag, next 12 bits signifying the channel, next 2 bits the APD route, next 1 bit specifying if the timetag is valid. The last bit is reserved for system purposes. 16 Bits for the timetag and a resolution of 100 ns for each 'tick' means the photon arrival time that can be saved into a t3r record could only go to $2^{16} * 100 \text{ ns} = 6553500$ nanoseconds, or 6.5 milliseconds. This limitation is overcome by recording an overflow event. Each time the measurement exceeds $n * 65535$ ticks, an event is recorded in the overflow channel and the 1 bit recording if a timetag was valid becomes 0 (= invalid). We counted the overflow events n and added $n * 65535$ to the timetag. All time tags were multiplied with 100 ns to compute the actual photon arrival time in nanoseconds.

2.5.2 Assigning channels, PIE/ALEX phases and excluding aggregates

As no marker pulse was generated corresponding to the excitation pulses, we needed to relate the photon arrival times to their corresponding phase in the excitation cycle in another way. To accomplish this the excitation scheme and pulse resolution was included in the t3r filename. The arrival times were assigned a position in the excitation cycle.

The photon arrival times were assigned to their corresponding APD as this information is recorded by bits 29 and 30. The arrival times were then accumulated relative to the excitation phase. To determine the unknown phase shift, we evaluated which pulse position contained the highest number of arrival times and used the signals from the Green APD to align this phase with the 514 nm excitation. After determining the position of the 514G pulse, the sorted arrival times were aligned with a correction factor. The relevant photon arrival times were sorted in channels G514 (514 nm excitation, emission on Green APD), R632 (632 nm excitation, emission on Red APD)

and R514 (514 nm excitation, emission on Red APD).

parameter	channel	before	after
τ_D (ms)	R632	2.41 ± 0.7	1.64 ± 0.01
	R514	1.82 ± 1.5	1.18 ± 0.01
	G514	1.81 ± 0.13	1.40 ± 0.01
N	R632	12.24 ± 0.3	10.91 ± 0.1
	R514	6 ± 2	5.7 ± 0.1
	G514	6.4 ± 0.2	5.9 ± 0.5
dynamics	K_{eq}	1.3 ± 1837	2 ± 5
	t_{open} (ms)	361 ± 1262	5 ± 3
	t_{closed} (ms)	499 ± 1335	11 ± 5

TABLE 2.2: **A single aggregate can disturb correlation curves of molecules such, that their diffusion times appear 30% slower.** The fitted number of molecules is less affected by the presence of a single aggregate in figure 2.11a. Kinetic rates were significantly affected, becoming 80 times slower. For all parameters, the fit errors reduced significantly upon exclusion of the aggregate.

Before correlating the photon signals we evaluated the signal stability over time of each channel. The mean intensity per second and standard deviation were calculated and used to exclude parts of the measurement exceeding a threshold of 2.5 of the standard deviation. The threshold could be changes in the main code of the program but was usually kept at 2.5. Time points where the mean signal exceeded $n \cdot \text{std}$ were saved in a separate list and used to divide the signal into shorter subsets of the photon arrival times. These subsets needed to span a measurement time large enough to generate a correlation curve full and accurate. For most measurements the length was set at 100 seconds, experience has shown to not set the subset length below 80 seconds.

The result of the exclusion algorithm is shown in Figure 2.11. Some samples contained PEG from a previous purification step, which caused aggregation of the fluorescently labeled nucleosomes. Even the occurrence of a single aggregate during measurement can distort the resulting correlation curves and dynamics curve (figures 2.11-a,c,e,g). Applying the exclusion algorithm resulted in deletion of 3.3% of the signals but yielded usable subsets and clean correlation curves that could be fitted accurately (figures

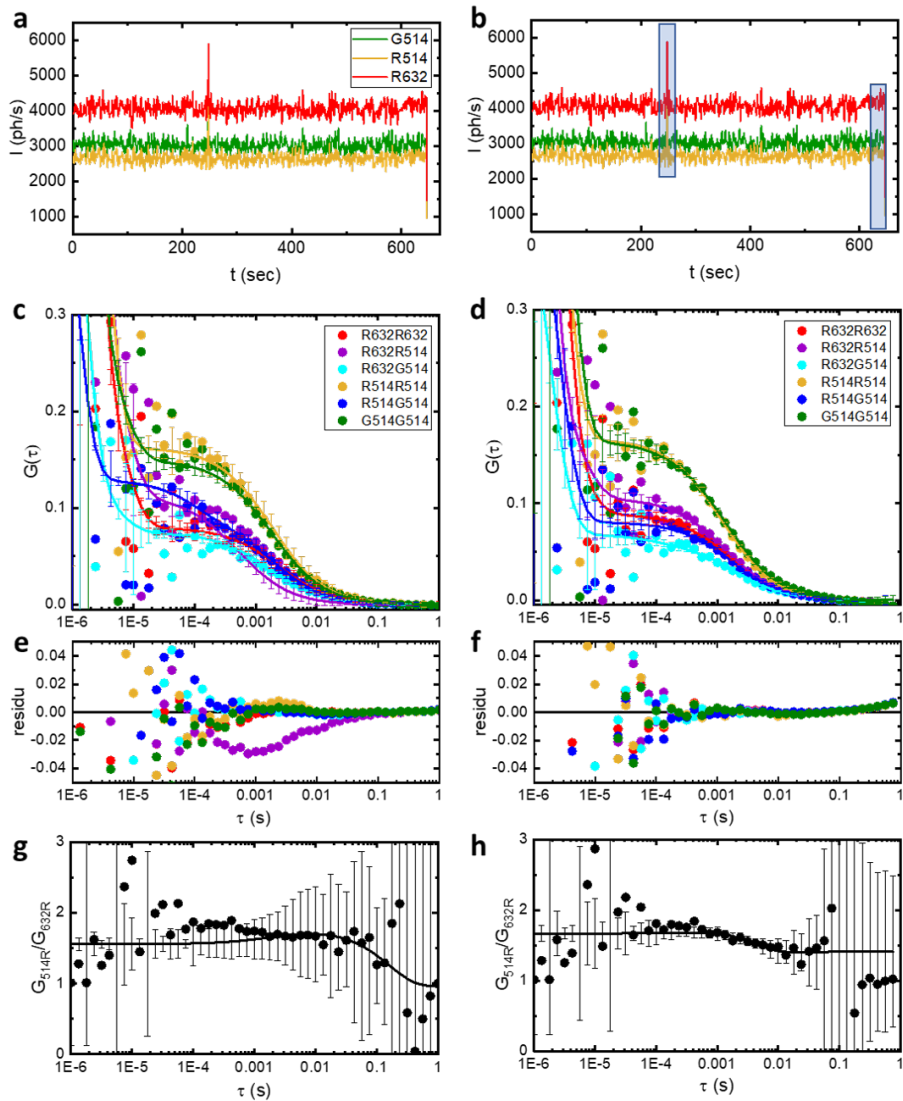


FIGURE 2.11: A single aggregate can disturb fluorescence signals making fitting of diffusion and kinetics more inaccurate. a) A single aggregate (at 250 seconds) changed the shapes of the correlation curves (c) and hence decreased accuracy of the fits (e). Also fitting kinetic rates became a more inaccurate exercise (g). Excluding 3.3 % (or 21 seconds) of the total 647 seconds shows fits becoming more accurate (d) and h)), and residues decreased (f).

2.11-b,d,f,h). Comparing fit parameters shows that diffusion and kinetics are most affected by the exclusion algorithm (table 2.2). The diffusion times and kinetic rates after exclusion resemble those found measurements that appear not disturbed by aggregates.

2.5.3 Correlation method and single-population fit

The hallmark of FCS is the quantification of the fluctuations from the mean intensity of a fluorescent signal, with the fluctuations representing molecules diffusing through a focus. From the correlation function described in equation 2.8 and visualized in figure 2.7 it appears there is always a signal ($I(t) \neq 0$) when binning over a large enough time. However, when reducing the bin size it becomes clear that the fluorescent signal is quite empty. Consider a signal of 1000 photons per second: reducing the bin size to one microsecond results in the signal becoming 0.001 photons per microsecond (or 1 photon being detected every 1000 microseconds). The temporal resolution used in our PIE experiments was 100 nanoseconds, meaning 1 in 10000 chance of detecting a photon (excluding background / dark photons) every 100 nanoseconds. As FCS measurements usually take minutes it is wise to choose an appropriate set of lag times τ that minimizes computational effort. A commonly used method to speed up calculations is the use of the multiple- τ algorithm[147]. This method entails calculating the first 16 time lags at full resolution, decreasing this resolution by half and grouping photons in bins accordingly. The process is repeated for 8 more time lags, and so forth, until a chosen point where minimal correlation is expected. The multiple- τ algorithm offers a dynamic range of time lags, but increasing resolution to sample more τ values also increases computation time. Hence we chose the algorithm developed by Laurence et al.[134] where the values of τ are not rigid but depend only on the time scale of the measurement; a base and the number of points (time lags) per base are defined in a time range in seconds. The scale invariance resulting from choosing an appropriate base speeds up computation time significantly.

As one cycle of excitation pulses in our PIE measurements was 800 nanoseconds long, the correlation time range was set from 10^{-6} to 10^1 seconds. The base was set to 10 (meaning \log^{10}) and number of points per base at 8. Oversampling by increasing the number of points per base lead to larger fluctuations in the correlation curve at small τ stemming from the dark periods in the pulse cycle. Undersampling by decreasing number of points

per base resulted in coarser correlation curves at large τ making fitting less accurate as also described by Laurence[134].

All correlation curves were fitted with equation 2.18; parameter bounds and initial guesses were set as shown in table 2.3. Only the value of a was fixed (at 8), all other parameters were free to be fitted. The standard deviation from dividing the arrival times into subsets was used as weight factor to minimize the residue of the data and fit. The `Minimizer` function in our Python program used the Levenberg-Marquardt algorithm to compute the best fit.

parameter	initial guess	$bound_{min}$	$bound_{max}$
N	1	$1E-4$	$1E3$
τ_D (s)	$1E-3$	$5E-4$	1
F_{tr}	0.1	0	0.9
τ_{tr} (s)	$7E-6$	$5E-6$	$1E-4$
F_{ap}	0.1	0	0.9
τ_{ap} (s)	$1E-6$	$1E-7$	$5E-6$

TABLE 2.3: **By choosing physical sensible initial guesses, bounds can be set wide to capture a wide range of possibilities.** Also setting bounds of characteristic times for diffusion, triplet states and afterpulsing to overlap did not result in fits capping on a bound.

parameter	initial guess	$bound_{min}$	$bound_{max}$
A	1	0.97	1.05
k_{on} (s^{-1})	120	0	2000
k_{off} (s^{-1})	80	0	2000
F_{tr}	0.1	0	0.9
τ_{tr} (s)	$3E-6$	$1E-7$	$5E-5$

TABLE 2.4: **Parameter bounds for fitting nucleosome dynamics.** The wide ranges made it possible to accurately fit the different dynamics when batch processing files of measurement of nucleosomes at different salt concentrations.

When differences in diffusion coefficient were expected, the relative correlation curve of R514/R632 was fitted with equation 2.19, with bounds and initial guesses as in table 2.4. We expected the contribution

of afterpulsing (ap) to vanish by dividing the correlation curves and leave only the effect of ATTO647N going into the triplet (tr) state. The fit was optimized using the LM algorithm and weighted with the relative errors of correlation curves R514 and R632.

2.5.4 Multi-population fit strategies

To determine stoichiometry of populations in a sample with two interacting molecules, or when protein labelling efficiency or concentration is known. The correlation curve is composed of the product of two fractions, for instance closed and open, or bound and free as represented in the diffusional part of $G(\tau)$ for different molecules:

$$G_{diff}(\tau) = N_{total}^{-1} \cdot (F_1 \cdot (1 + \tau/\tau_{D1}) \cdot (1 + a^{-2} \cdot \tau/\tau_{D1}))^{-1/2} \cdot (F_2 \cdot (1 + \tau/\tau_{D2}) \cdot (1 + a^{-2} \cdot \tau/\tau_{D2}))^{-1/2} \quad (2.20)$$

with $F_1 + F_2 = 1$. For nucleosomes the closed fraction is obtained from the ratio between the autocorrelation curve from the FRET channel and the direct excitation of the acceptor ($F_{closed} = \frac{N_{closed}}{N_{total}}$). From the fit of the FRET channel, we also obtained the characteristic diffusion time ($\tau_{D,closed}$), leaving only the diffusion time of open nucleosomes $\tau_{D,open}$ to be fitted by the multi-population fit.

The multi-population fit algorithm can also accurately fit more than one unknown parameter. When estimating labelling efficiency of a protein with only the diffusion time of free dye known, the algorithm is able to find from the autocorrelation curve the characteristic diffusion time of the labeled protein as expected from calculations. The ratio of the fractions was confirmed by gel electrophoresis. The multi-population algorithm can be expanded to estimate a third population, though this requires several different baseline experiments to reduce variable parameters.

2.6 Conclusions

In this chapter we have described the procedures for proper preparation, calibration, characterization and correction of samples and setup, as well as the analysis process for single-molecule experiments. Quantifying the intricacies of fluorophore signals in the microscope setup and optimizing alignment of the setup yielded correct physical parameters of fitting the correlation curves from various channels.

The use of ALEX or PIE allowed to distill in addition to the concentration and diffusion times, kinetic rates and multiple populations. The algorithm presented here to exclude aggregate effects from long measurements is a novelty in the FCS field. By using this algorithm, one does not have to measure 'around the aggregates' as was the recommended method[139]. The excluding method can also be used inversely to investigate condensates. Overall, using multiple excitation and detection colors in combination with multiple fluorophores and advanced correction and analysis protocols makes it possible to accurately quantify concentrations, diffusion times and interaction rates within a single experiment with relatively little sample. These features go beyond the capabilities of traditional single color FCS.

**OPTIMIZING DNA SYNTHESIS, PURIFICATION,
AND HANDLING FOR SINGLE-PAIR FRET
EXPERIMENTS ON NUCLEOSOMES**

3.1 Introduction

Recent years have seen a flux in chemical and biological methods and equipment for more reliable synthesis, purification and identification of biomolecules[148][149]. The emergence of bioinformatics, computational biology and -omics sciences have simplified and made accessible computational tools to design and predict biochemical compounds[150][151]. Smaller detection volumes facilitated by technologies like nanoholes[152], nanojets[153], nano-antennas[154] and sub-microfluidic channels[155], have decreased the need for large amounts of samples and hence the need for bulk production of such samples.

An ongoing issue in biological chemistry is that protocols of others are difficult to reproduce, as some information, knowledge or expertise is assumed to be, but in fact is not, trivial[156][157][158][159]. For parameter settings of computational predictions[160], temperature steps and cycles for synthesis through PCR[161] or biochemical reaction steps for surface functionalization[162][163] one sometimes needs to take into account the impact of something as trivial as room temperature [164].

In this chapter we expand on the detailed protocols used for synthesis and purification of relatively short DNA strands ranging between 200 to 500 base pairs from 80 bp long primers containing fluorophores and either a protein recognition element at specific positions, or elongated or shortened DNA arms. The unusual length of the primers and the DNA construct, the reconstitution into nucleosomes and the application of spFRET required adjustments of standard protocols. Here, we have optimized PCR, ligation, PEG and ethanol precipitation protocols to acquire high yields of the desired end product. We will show the consequences of non-optimized steps or the absence of some of these steps on single-molecule fluorescence microscopy and spectroscopy data and the conclusions one might erroneously draw from these kind of results.

3.2 Construct design

The Widom 601 sequence was incorporated in all DNA and subsequent nucleosome constructs used in this thesis (with the exception of DNA-FRET) and was chosen because of its high affinity to, as well as its positional accuracy of the histone octamer[41]. The 601 sequence was inserted into a plasmid (pGem3z) which was used as the template in PCR amplification.

Also included in the plasmid, flanking the 601 sequence, were two recognition sites for restriction enzymes. After synthesis through PCR, the base DNA construct (Figure 3.1a) was 198 base pairs long and included fluorophores ATTO647N (@T41) and Cy3B (@C122), recognition sites for BsaI (bp19-24, magenta) and BseYI (bp187-192, blue). Additional DNA was included in the hinges (capital letters, bp 1-40 and 187-198) to ensure high yields for restriction. In order to investigate the binding efficiency of the Glucocorticoid Receptor (GR), as well as to quantify the effect on nucleosome dynamics of the protein's recognition site (GRE), as we have done in Chapters 6 and 4 of this thesis, we inserted the GRE into the Widom601 sequence at 4 different sequences (Fig. 3.1c).



FIGURE 3.1: **a**) Blueprint of the 198 basepair DNA construct containing Widom 601 sequence. **b**) The forward primer contains label ATTO647N, a recognition site for BsaI and is 80 bp long. The reverse primer contains label Cy3B, a recognition site for BseYI and is 85 bp long. **c**) GRE sequence substitutions inserted in the forward primer.

3.3 DNA synthesis and purification

DNA strands were synthesized via Polymerase Chain Reaction (PCR). During PCR a mix of nucleotides, primers (single-stranded DNA / oligonucleotides), template (double-stranded DNA) and a DNA polymerase enzyme were

cyclically heated and cooled to amplify the template. The first step was activation of the DNA polymerase; after this step, each cycle started at high temperature to melt the double stranded DNA template. The temperature was then lowered to allow for annealing of the primers to the melted DNA. For the final step in the cycle the temperature was changed to an intermediate of the melting and annealing steps to elongate the primers bound to the strands of the DNA template by the DNA polymerase. The details of the program will be discussed below.

After PCR synthesis, the double-stranded DNA needed to be extracted from the PCR solution to properly determine the yield, as well as omit effects of the solution on subsequent single-molecule experiments. Also, the product needed to be separated from unused primers, as free, labeled primers would affect the fluorescence signal.

3.3.1 Decelerated PCR to optimize synthesis of DNA constructs from long primers

As the length and the high GC-content of the primers for constructing the DNA containing the 601 sequence required a relatively high annealing temperature[165][166], bringing it close to the elongation temperature, the PCR protocol was optimized by trying a range of annealing temperatures between 60-72°C. Also, compared to the previous protocol used by Buning[104], we increased the times of the amplification steps as well as the number of cycles[167]. To further optimize the PCR protocol the ratio of the forward and reverse primers was also investigated. The optimized PCR protocol was as follows:

- Activation: 4 minutes at 95°C
 Followed by 50 cycles of
- Denaturation: 45 seconds at 95°C
- Annealing: 30 seconds at 68°C
- Elongation: 1 minute at 72°C.

The protocol was concluded with an additional 5 minutes at 72°C, and cooled down (on hold) for infinite time at 4°C. The optimized mixture for the primers was 1:3 or 1:4, regardless of which primer is in excess for synthesizing double-labeled constructs, and a ratio 1:6 of forward (ATTO647N) : reverse (unlabeled) to produce single-labeled constructs,

see figure 3.2b. Final concentrations of the DNA constructs were between 150-400 ng/ml.

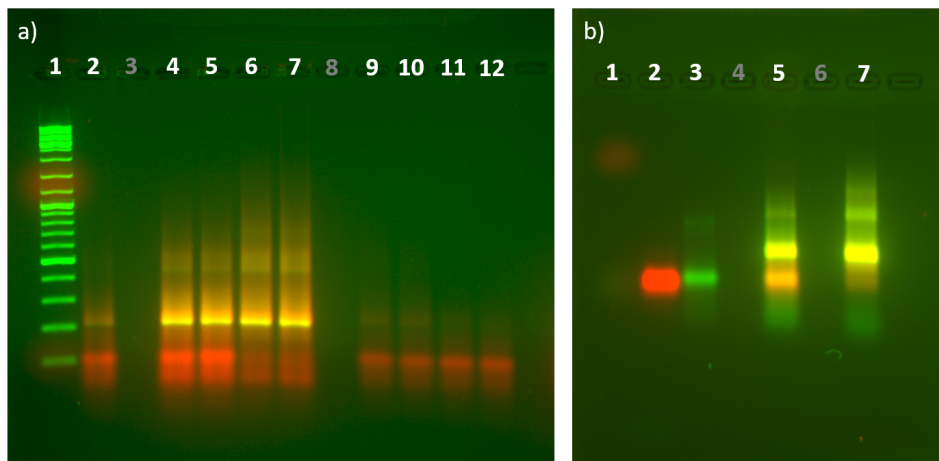


FIGURE 3.2: Optimization of PEG-NaCl precipitation showed that the protocol is optimal at room temperature and subsequent ethanol washing. a) After PCR (lane 2) DNA product is visible at 200 bp (GeneRuler DNA Ladder (Thermo Fisher Scientific) in lane 1) as well as residual forward primer (red band at 100 bp), which was added in excess (forward:reverse 8:1) for testing the PEG-NaCl protocol. Incubating the PCR product overnight in 24% PEG and 1.8 M NaCl at 0°C resulted in incomplete separation of product and primer; there was still primer present in the pellets, and DNA product in the supernatant (pellets: lanes 4 and 5, supernatants: lanes 9 and 10). Performing the protocol at 20°C resulted in pellets practically free of primer, and less than 10% of the product left in the supernatant (pellets: lanes 6 and 7, supernatants: lanes 11 and 12). The 1.5% agarose gel was stained for 2 hrs with 1% EtBr solution, image is an overlay of fluorescence channels 515 nm and 647 nm. b) When primers are added in lower excess (ratio forward:reverse 3:1) after PCR the ratio product to primers was 1:1 (lane 5). After PEG-NaCl precipitation, less than 5% of the product was primer. Moreover, both primers did not seem to be present in a clear band. This gel was not stained with EtBr, so the DNA ladder was only visible in lane 1 through red marker 1200bp. The image is an overlay of fluorescence channels 515 nm and 647 nm.

3.3.2 PEG and salt-induced precipitation optimized for long primers and short DNA strands

With the length of the primers (of at least 80 nucleotides) being relatively close to the length of their product (198 base pairs), purification became a non-trivial exercise. As excision from agarose gel and subsequent ethanol purification proved a time-intensive and low-yield method[104], separation through PEG precipitation was investigated. The principle of this method is that DNA can be precipitated from a solution by neutralizing its charge with salt ions. The polymer, here polyethylene glycol (PEG) 6000 ($\text{H}(\text{OCH}_2\text{CH}_2)_n\text{OH}$, $n=6000$), functions as a crowding agent that facilitates the aggregation of DNA. This technique works best when the sizes of the fragments to be separated differ at least by a factor of two. This separation threshold can be modulated by altering the percentage of PEG in the solution; smaller DNA-fragments will precipitate at a higher PEG percentage, larger DNA-fragments at a lower PEG percentage. Titrating PEG percentages, we determined the separation threshold for our 198 bp DNA strand is around 24% PEG. Other parameters influencing the efficiency of the precipitation include salt valency and concentration, incubation temperature, as well as centrifuge time and rotor speed. Based on the previous findings of Schleif[168] and Ran[169] titrations of NaCl (up to 2 M) and MgCl_2 (up to 40 mM) were tested; we found monovalent NaCl at a final concentration of 1.8 M to be most optimal for our construct. Incubation temperature was tested at 0, 20 (RT) and 37°C (fig. 3.2a: lanes 4, 5, 9, 10 at 0°C, lanes 6, 7, 11, 12 at 20°C. 37C not shown); between 20 and 37 degrees no significant differences were observed in efficiency. Between 0 and 20 degrees Celsius we quantified the concentration differences by assessment of the fluorescent intensity in ImageJ. The ratio DNA:primer in the PCR mix is 2:7 (Fig. 3.2a, lane 2) after precipitation; at 0°C this ratio is 2:3 (lanes 4 and 5), at 20°C it is 1:1 (lanes 6 and 7). At 20°C the primer is not present at one specific size (no band visible), which might indicate the presence of hair-pinned (non-functional) primers[170]. Moreover, in the supernatant the 198 DNA product was visibly present at 0°C (lanes 9 and 10) at a ratio of 2:5, whereas the ratio at 20°C was 1:10 (lanes 11 and 12). The optimized PEG-NaCl protocol was as follows:

- Mix PCR sample (up to 400 μl) with PEG (to 24%) and NaCl (to 1.8M) to a total volume of 1 ml

- Incubate overnight at 20°C (RT)
- Centrifuge for 2 hours at 14.000 rpm
- Remove supernatant and resuspend pellet in MilliQ (50-100 μ l)

Using this protocol it was possible to obtain products with concentrations up to 700ng/ml. Figure **3.2b** shows the results after PCR (with primers in ratio 1:3) (lane 5), and after PEG-NaCl precipitation (lane 7). Based on fluorescence intensity assessed with ImageJ we estimated less than 5% of the DNA in the sample after PEG-NaCl was primers. Ethanol precipitation was necessary as an additional cleaning step due to remnant PEG; the yield after ethanol washing (with Promega DNA Purification Kit) was between 50-70%, with concentrations of 350 ng/ml. Compared to extraction from gel and subsequent ethanol precipitation, where yields were on average 40%, with concentrations of \sim 100ng/ml, PEG-NaCl precipitation proved a clear improvement. Compared to loading and excising constructs from gel, PEG-NaCl is significantly less time and labour consuming.

3.4 Nucleosome reconstitution

Nucleosomes were reconstituted from DNA and histones (recombinant human, EpiCypher) via salt-gradient dialysis. DNA substrate containing the 601 sequence and histones were mixed in molar ratios ranging from 1:0.5 (Fig. **3.3a** lane 4) to 1:2.5 (Fig. **3.3a** lane 8) and complemented with competitor DNA; the latter was added to prevent aggregate formation from a surplus of histones. Final concentrations of the DNA construct and competitor DNA were 100 nM and 40 nM. TE (Tris/EDTA) and NaCl were added to final concentrations of 1x (TE) and 2 M (NaCl) and the samples were diluted with MilliQ to 50 μ l. They were then loaded in mini dialysis tubes (Thermo Scientific, Slide-A-Lyzer mini dialysis tubes 3500 MWCO) and secured in a home-made tube holder. The holder was placed in 200 ml high-salt buffer (2 M NaCl, 1x TE, MilliQ) in a 1L glass beaker, containing a magnetic stirrer. The beaker was placed in a cold room (4°C) and connected via an Econo gradient pump (Bio-Rad) to 1 L of low-salt buffer (1x TE, MilliQ). The magnetic stirrer was set to low speed to mix inflowing low-salt buffer with the high-salt buffer. Depending on how fast reconstituted nucleosomes were needed, the flow rate was set to 1.2 ml/min for overnight, or to 1.9-2.2 ml/min for daytime reconstitutions. After dialysis was completed, samples

were collected in low-binding 1 mL Eppendorf tubes and stored in 4°C.

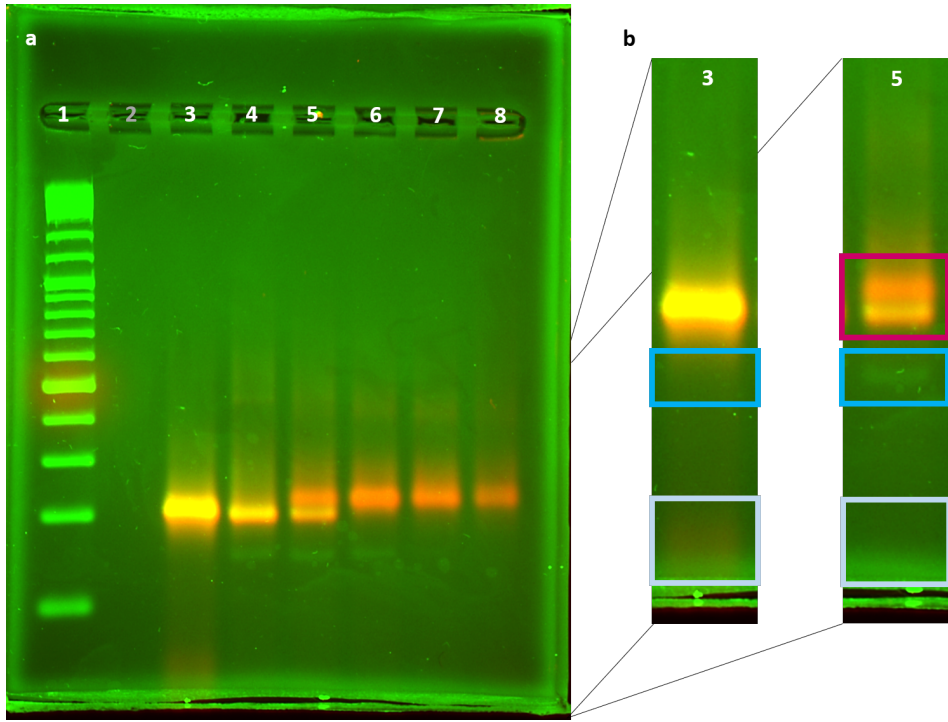


FIGURE 3.3: DNA reconstitution through automated dialysis showed robust results from histone titration. a): gel with DNA ladder (lane 1), EtBr stained. lane 3: DNA, lane 4: DNA:histones (HO) 1:0.5, lane 5: DNA:HO 1:1, lane 6: DNA:HO 1:1.5, lane 7: DNA:HO 1:2, lane 8: DNA:HO 1:2.5. b) excerpts of lane 3 and lane 5; grey squares = left over primers (lane 3) disappeared (lane 5) through dialysis, blue squares = competitor DNA (lane 5), red square = incomplete reconstitution.

Mononucleosomes reconstituted via this protocol can be stored at 4°C for years. The reconstitution protocol described here was used in this thesis and is an optimization of an earlier protocol used by Buning[104], where the salt-gradient was applied in discrete steps. The protocol also differs from the one used for the reconstitution of chromatin fibers by Kaczmarczyk et al.[171], which used 10.000 MWCO mini dialysis tubes and maintained a dialysis flow rate of 0.9 ml/min.

Results of a nucleosome reconstitution were assessed on gel (0.2 TB) as depicted in figure 3.3. Despite the small size difference a clear distinction

can be made between free (lane 3) and reconstituted (lanes 5-8) DNA. The difference was most obvious in lane 5, where both forms were present due to an incomplete reconstitution. Next to gel shift, the difference was also visible from fluorescence. Nucleosomes appear as an orange band, caused by a decrease of green emission from green excitation due to FRET (fig. **3.3b**, right lane (5), yellow and orange band in red square).

Another indicator of incomplete reconstitution is the presence of unreconstituted competitor DNA (fig. **3.3b**, lanes 3 and 5, blue square) around 150 bp. This band, which is visible through EtBr staining of DNA, disappears in higher reconstitutions due to reconstitution of the competitor DNA as nucleosomes don't stain well with EtBr. Lastly, it was observed that leftover primers were removed in the reconstitution process (fig. **3.3b**, lane 5, grey square) despite that their molecular weight (~ 25 kDa) was larger than the cut-off of the dialysis membrane.

3.5 Surface passivation and molecule immobilization

Scanning confocal microscopy (SCM) has been used to study nucleosomes dynamics[172][126] and DNA/nucleosome interactions with proteins by immobilizing (one of) the molecules on a passivated surface[95]. In principle, SCM allows for tracking of separate, single molecules. However, surface passivation and immobilization puts high demands on the used protocols.

During sample preparations in our lab, it was observed that chemicals needed to be fresh (APTES), well-mixed (PEG-bPEG), fresh, uncontaminated and well-solvated (Neutravidin) and at appropriate concentrations (molecule of interest, several picomolar) to ensure a certain homogeneous surface cleaning, surface coverage and evenly separated binding positions. Even an optimized passivation and immobilization protocol for nucleosomes can however cause non-optimal results; some of the molecules are immobilized too close to one another for optical resolving (figure **3.4a**, light blue circle). A subsequent issue is bleaching of fluorophores by long exposure times: in figures **3.4a-b** the fluorophores on the nucleosome tracked in the white circle were bleached after measuring for 180 seconds. However, the timetraces in figure **3.4c** showed that the signal from Cy3B already disappeared after 22 seconds; the red emission from red excitation appeared quite unstable over time; this was likely caused by

small movements of the sample stage.

The surface passivation protocol consisted of four steps:

1) Cover slide cleaning: performed in a beaker glass that fits a cover slide holder. Typical volume needed: ~350 ml. Sonicate glass cover slide in MilliQ (10 minutes), 1M KOH (10 minutes), MilliQ (10 minutes), 1M KOH (10 minutes), then MilliQ (10 minutes) again.

2) Aminosilanization: prepare a 4% solution of 3-aminopropyltriethoxysilane (APTES) in acetone (Volume should be sufficiently large to cover surface if slide is not on flow cell yet). Immerse cover slide in reagent for 3-5 minutes. Rinse surface with acetone, MilliQ. Blow dry, attach to flow cell, rinse with NaHCO₃.

3) PEG incubation: treat surface for 20-30 minutes with 100:1 methoxyPEG-succinimidyl succinate : biotin-PEG-OCH₂CH₂-CO₂-NHS (PEG:bPEG) in 100 mM NaHCO₃ (pH 8.3). Rinse with Tris 10 mM.

4) Sample preparation: treat surface for 20-40 minutes with Neutravidin (1 μ M) in buffer of 10 mM Tris-HCL (pH 8.0) and 10% BSA. Rinse with MilliQ. Add molecule of biotinylated DNA (10 pM) in a buffer containing at least 10 mM Tris and 10% BSA. NP-40 and Trolox can also be added; however, when added during our experiments no improvement in signal stability was observed.

Typical results of this protocol are shown in figure **3.4a-b** (double-labeled nucleosomes) and figure **3.5a-d** (single-labeled DNA, red). Examining label stoichiometry and FRET efficiency of immobilized nucleosomes showed the effect of immobilization on the ratio of populations, as discussed in the previous chapter. Although an oxygen scavenger system as well as a photobleaching reductor (Trolox) were added, scanning immobilized nucleosomes showed 64% of the acceptor fluorophores was quenched or bleached, compared to 14% in spFRET burst experiments. Only 9% of nucleosomes lost their donor fluorescence through immobilization in SCM. In figure **3.4a** the the donor- and acceptor-only nucleosomes show as green, respectively red blots. Nucleosomes containing both fluorescent

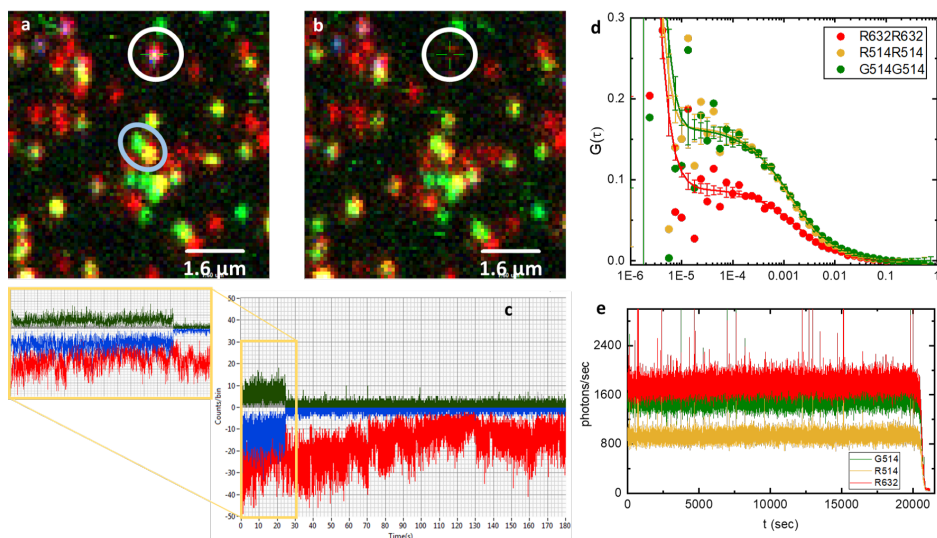


FIGURE 3.4: Surface passivation with PEG/bPEG conserves DNA compaction in nucleosomes but makes separation of single molecule difficult for further analysis. **a)** Surface passivation resulted in intact immobilized nucleosomes (white circle), visible from the overlay of the red, green and FRET (blue colored) channels. Overlay showed nucleosomes having a pink hue, whereas dissociated nucleosomes showed up as yellow/orange dots (lower dot in light blue circle). **b)** Imaging caused however irreversible bleaching of both fluorophores (white circle). **c)** In the first 23 seconds of the point scan (inset), it was not clear from the timetraces if nucleosome dynamics in the order of seconds was occurring. Also, from investigating its time-trace, it was uncertain if the red fluorophore had survived the scan. **d)** Although not as visually direct as SCM images, FCS correlation curves from nucleosomes contain similar information on nucleosome breathing dynamics. **e)** FCS measurements were performed on diffusing nucleosomes in solution, which lowered bleaching events to practically zero. In solution, nucleosomes could be measured for more than 22.000 seconds (= 6.1 hours) without changes in fluorescence intensity; the measurement was only stopped because the water droplet between the objective and glass slide had evaporated.

labels made up only 27% when immobilized, compared to 80% of the total population when freely diffusing. Of the population of double-labeled nucleosomes, about half was observed having a FRET signal (pink blots in fig. 3.4a, designated as high-FRET fraction), and the other half having no or a minimal FRET signal (yellow blots in fig. 3.4a, designated as low-FRET fraction). Performing a point scan on a high-FRET nucleosome (fig. 3.4a,

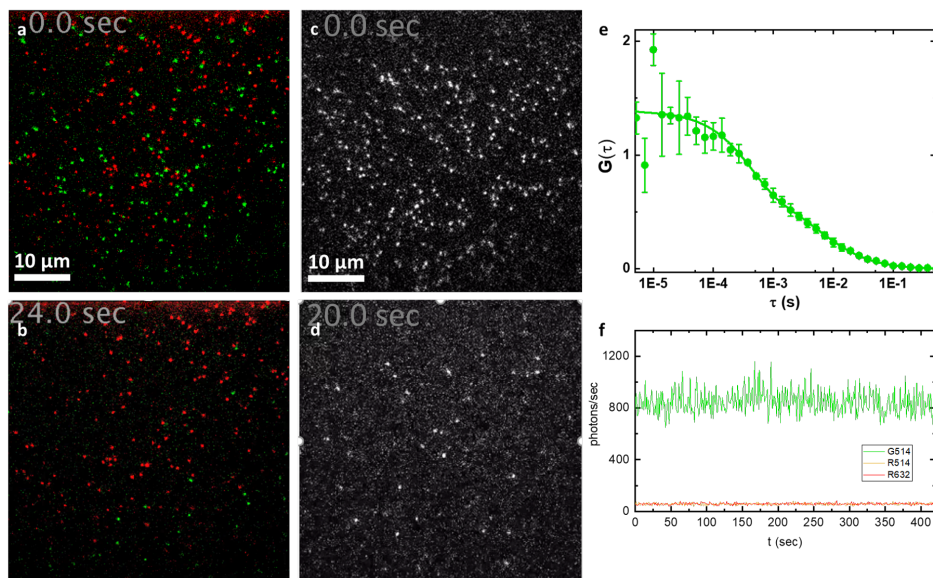


FIGURE 3.5: Surface passivation with PEG/bPEG causes nonspecific binding of the Glucocorticoid Receptor to the surface and not to specific DNA. a) Investigating binding of the GR protein (green, labeled with EYFP) to DNA containing a GR specific binding sequence (red, labeled with ATTO647N) in TIRF did not result in colocalization (3x) of the red ($\sim 250\times$) and green ($\sim 180\times$) signals. **b)** After several seconds, the green signals decreased, implying bleaching of EYFP, due to the GR not dissociating, nor swapping with other GR from the solution, but staying bound to the surface, likely saturating it so no new GR was able to bind. **c)** When GR was added to a surface not containing any DNA (either containing a specific binding sequence or not) similar binding **d)** and staying bound was observed. **e)** Using FCS it was possible to create a robust correlation curve, **f)** from a stable fluorescent signal not showing any signs of non-specific sticking and staying bound to the glass surface.

white circle) as described in the previous chapter resulted in time traces of donor (forest green), acceptor (red) and FRET (dark blue) fluorescence, plotted in figure 3.4c. For 23 seconds, until bleaching of the donor fluorophore terminated the donor as well as FRET signal, the three time traces were clearly distinguishable from background. However, unlike observations from TIRF measurements on immobilized nucleosomes by Koopmans et al.[172] intensity switching in the order of seconds in the donor and FRET channel was not observed in our experiments. Apart

from one of the fluorophores (most often the donor) bleaching after 5-25 seconds of point scanning (fig. 3.4b, 3.4c, inset) time traces also showed fluctuations, likely originating from not only movement of the nucleosome around the immobilization point, but also vibrations/instabilities in the confocal setup (fig. 3.4c, red time trace). In addition, in SCM nucleosomes were designated manually, as our search algorithm was unable to distinguish between molecules too close to each other (fig. 3.4a, blue circle). Compared to the highly automated FCS data acquisition and analysis this was a very time-consuming step.

Surface passivation is also used in interaction experiments with immobilized DNA or nucleosomes and proteins from solution[50][95][100].

3.6 Conclusions

In this chapter we have shown that optimizing the synthesis, separation and purification of DNA constructs resulted in higher yields, higher purity of the end product, were less labor intensive and less prone to errors; i.e. more control over DNA substrates. It is however prudent to keep in mind that product optimization is still very construct dependent.

Surface passivation and immobilization protocols were optimized as well and resulted in fluorescent signal clearly distinguishable from background noise. However, signal from single nucleosomes were still difficult to attain due to clustering. Interactions with the surface also seemed to decrease the high-FRET population, compared to nucleosomes measured in solution, and irreversible bleaching together with clustering made finding suitable nucleosome very labor and time intensive. Also, when nucleosomes survived surface immobilization no dynamics in order of seconds was observed. The absence of dynamics might be caused by the addition of stabilising agent Nonidet P40 (NP-40), which is known to prevent surface adsorption[173]. It is also associated with nucleosome dissociation at higher concentrations of NaCl. We will show in chapter 4 addition of NP-40 slows down nucleosome dynamics significantly.

For DNA/nucleosome - protein interactions, minimal specific interactions and predominantly nonspecific interactions were observed when samples were deposited on PEG/bPEG coated surfaces. These interactions were not observed during spFRET burst and PIE-F(C)CS measurements in samples on untreated glass (data shown in next chapters).



NUCLEOSOME STABILITY AND ACCESSIBILITY DEPENDS ON LINKER DNA LENGTH, NUCLEOSOMAL DNA SEQUENCE, BUFFER COMPOSITION

To facilitate access of proteins like transcription factors to the nucleosomal DNA, nucleosomes spontaneously unwrap DNA from their ends. Transcription factors bind to specific DNA sequences often located at the DNA exits of the nucleosome. To study the effects of the linker DNA and sequence on nucleosome stability and dynamics we constructed sets of mononucleosomes based on the Widom 601 sequence with small variations in these features. We combined Fluorescence Correlation Spectroscopy (FCS) with Pulsed Interleaved Excitation (PIE) and FRET Forster Resonance Energy Transfer (FRET) to quantify DNA unwrapping. Extending the nucleosome with several 10's of base pairs of linker DNA has a stabilizing effect on the nucleosome at low ionic conditions. The effect is reversed at a critical salt concentration inversely proportional to the length of both DNA linkers. A Glucocorticoid Response Element (GRE) in the 601 nucleosome increases the opening and closing rates and affects nucleosomal stability by decreasing electrostatic interactions between DNA and histones, depending on its position with respect to the minor grooves of wrapped DNA. Lastly we show the effect of small changes in buffer composition have on nucleosome dynamics, and discuss irreversible unwrapping occurring on longer timescales. By taking into account these external components and combining PIE-FCS with FRET we quantified the effects of small changes in linker DNA length and nucleosomal DNA sequence on dynamics and stability with increased accuracy and reliability. Hence our technique holds the promise to be suited for probing nucleosomes reconstituted from natural DNA sequences or modified histones, representing the rich but subtle variety of nucleosomes occurring in vivo.

4.1 Introduction

In order to fit inside the nucleus but also be readily available for transcription, DNA needs to be compacted in a non-trivial way. The first level of DNA compaction is the nucleosome, in which the 147 base pairs of DNA are wrapped around an octamer of histones[34][35]. In vivo, nucleosome compaction is modulated by remodelling proteins, transcription factors and other cofactors[96][97][174]. To provide these proteins access to the nucleosomal DNA, nucleosomes spontaneously unwrap DNA from their ends[175][37][51]. This reversible process is called nucleosomal breathing. Forster Resonance Energy Transfer (FRET) has been used to follow nucleosome formation and compaction at nanometer resolution[172][176][53][103][177]. These experiments showed that DNA unwraps at the nucleosomes' exits, yielding access to the nucleosomal DNA. These conformations are referred to as 'open' in contrast to fully wrapped 'closed' nucleosomes. Various in vitro experiments have shown that the interactions between DNA, histones and transcription factors depend strongly on the ionic concentration of the buffer[50][178].

Other single-molecule FRET experiments showed that an increase of linker DNA length in a single nucleosome changed the equilibrium between the open and closed states[104][98][99]. In native chromatin the linker length varies between 10 to 90 base pairs[179][180]. Nucleosomes with longer linker DNA prefer compaction over unwrapping, but the level of compactness is on average lower and has a wider spread[104], indicating increased competition for DNA binding to the histone core. To quantify the role of linker DNA in nucleosome stability and accessibility we designed mononucleosomes with varying linker DNA lengths.

Previous single-molecule studies by Luo et al. have proposed that nucleosomal breathing is the rate-limiting step for specific binding of the LexA protein to its recognition site[100]. For other transcription factors such as the Glucocorticoid Receptor (GR) it has been shown that the position of proteins' recognition sequence in the nucleosome affects binding affinity[39][181][182]. GR is a member of the nuclear receptor family and is translocated to the nucleus upon activation through hormone binding[183][184]. In the nucleus GR interacts directly with DNA, influencing gene expression[185][186][187][188]. According to Wrangé et al. the GR prefers binding to a recognition site positioned at a nucleosome exit[94][95] compared to sites closer to the dyad; Jin et

al. showed that the GRs' DNA Binding Domain (DBD) prefers recognition sequences positioned in outward facing minor grooves of the DNA [95]. These and other interaction experiments so far have focused on the binding affinity[94] or bound time[95] of GR to nucleosomes without taking into account the effect of the position of the recognition sequence on nucleosome stability itself. It has been previously shown that nucleosome stability is affected by sequence dependent variations in the nucleosomal DNA[189][190][41][191]. Here we investigate whether the position of a protein recognition sequence has an effect on nucleosome dynamics. Extensive probes have shown transcription factor recognition sites are often located near the nucleosomal DNA exit [192][193][194][195]. To mimic this we have inserted the Glucocorticoid Response Element (GRE) at different positions in a nucleosome and quantified the effect on nucleosome accessibility.

Stabilizing agents like NP-40 are often added to keep nucleosomes from unwrapping in order to study the equilibrium of states[51][50][178][104]. These stabilizers were also added when investigating the affinity of proteins that interact with nucleosomes[100]. Here we will show that addition of NP-40 slows down nucleosome dynamics. Assuming the nucleosome dynamics is the rate-limiting step in protein-nucleosome interactions[50], this means the use of stabilizers in the investigation of these interactions leads to underestimating the affinity.

4.2 Theory

4.2.1 Nucleosome dynamics

Nucleosomal breathing, i.e. switching between an open and closed conformation, is a reversible process governed by the electrostatic interactions between the wrapped DNA and histone tails



where N_{open} , N_{closed} represent the open and closed conformations of the nucleosome. The equilibrium between the open and closed states is defined by equilibrium constant

$$K = \frac{[N_{open}]}{[N_{closed}]} \quad (4.2)$$

When nucleosomal DNA unwraps, electrostatic interactions between DNA and histones are broken. After (partially) unwrapping the released DNA attracts m number of cations X^+ from the buffer to replace the positively charged histone residues. Taking these explicitly into account, eq. 4.2 can be rewritten:



making the equilibrium salt dependent

$$K_X = \frac{[N_{open} \cdot X_m]}{[N_{closed}] \cdot [X^+]^m} = \frac{K}{[X^+]^m} \quad (4.4)$$

Previous experiments on nucleosome breathing indeed showed K to scale exponentially with $[Na^+]$ [173]. In order to determine the order of the dependence on the salt concentration from experiments, we rewrite eq. 4.4 such that the number of ions released upon rewinding of the nucleosomal DNA can be easily extracted from the exponent of the salt dependence of the measured equilibrium between the measured open and closed nucleosomes in the absence of salt[196]:

$$K = K_X \cdot [X^+]^m \quad (4.5)$$

An additional parameter K_0 was added because at low NaCl concentration the equilibrium did not depend on the salt concentration:

$$K = K_X \cdot [X^+]^m + K_0 \quad (4.6)$$

We defined transition concentration c_0 as the concentration where the equilibrium started to be affected by NaCl, i.e. where the first term of eq. 4.6 equals the second term.

4.2.2 Fluorescence Correlation Spectroscopy (FCS)

We used FCS to measure nucleosome dynamics. For this, we used nucleosomal DNA labeled with two fluorescent dyes that form a FRET pair, positioned at the nucleosome dyad and one of the nucleosomal exits. Due to Brownian

motion, the nucleosomes diffuse in and out of the confocal volume, which causes the fluorescence intensity to fluctuate in time[197]. The fluctuations of the intensity were analyzed by correlating the photon arrival times over increasing time-lag τ :

$$G(\tau) = \frac{\langle \delta I(t) \cdot \delta I(t + \tau) \rangle}{\langle I(t) \rangle^2} \quad (4.7)$$

As the fluctuations of fluorescence intensity depend on the concentration and diffusion of the nucleosomes and the confocal volume which they diffuse through, $G(\tau)$ is described by

$$G(\tau) = (V_{eff}C)^{-1} \cdot (1 + \tau/\tau_D)^{-1} \cdot (1 + a^{-2}\tau/\tau_D)^{-1/2} \quad (4.8)$$

with diffusion time τ_D and average number of nucleosomes N in focal volume V_{eff} at concentration C .

4.2.3 Nucleosome dynamics measured with FCS-PIE

The equilibrium between open and closed nucleosomes can also be described kinetically:

$$K_{kin} = \frac{k_{opening}}{k_{closing}} \quad (4.9)$$

As shown by Torres[198] and Tims[199], FCS provides a unique way to obtain these rates. Dividing the autocorrelation curve of the closed nucleosomes as obtained from the nucleosomes that exhibit FRET (G_{514}^R) by the autocorrelation curve of all nucleosomes quantified by the fluorescence of the acceptor dye when excited directly (G_{632}^R) cancels out the diffusion contribution. Instead of performing two separate FCS experiments to obtain these autocorrelation curves[198] or measuring a single sample consecutively with different excitation wavelengths[199], we combine multiple excitation wavelengths through Pulsed Interleaved Excitation (PIE)[137] and use the curves acquired from a single FCS-PIE experiment to prevent effects of different concentrations of nucleosomes between experiments[198] or from decay occurring on longer timescales[199]. The resulting curve mainly represents the nucleosomal dynamics, but also contains a contribution of different photophysical phenomena and detector responses, collectively captured in $G_{photophysics}$:

$$\frac{G_{514}^R}{G_{632}^R}(\tau) = C(\tau) \cdot \left(1 + K_{kin} \cdot e^{-\tau(k_{opening} + k_{closing})}\right) \cdot G_{photophysics} \quad (4.10)$$

Assuming equal diffusion times for open and closed nucleosomes, as done by Torres[198] and Bohm[173] makes the correction factor $C(\tau)$ equal to 1. However, previous experiments by Koopmans and Buning on similar nucleosomes as used in this chapter have shown that closed nucleosomes diffuse significantly faster than open nucleosomes[176][53]. Therefore, when calculating G_{514}^R/G_{632}^R , we assumed $\tau_D^{514R} \neq \tau_D^{632R}$ resulting in

$$C(\tau) = \sqrt{\frac{\tau_D^{632R} \cdot (\tau_D^{514R} + \tau)}{\tau_D^{514R} \cdot (\tau_D^{632R} + \tau)}} \quad (4.11)$$

4.3 Materials and methods

4.3.1 Nucleosome reconstitution and sample preparation

DNA containing one Widom 601 sequence and a Cy3B-Atto647N fluorophore pair was produced with PCR. The fluorophores were positioned 80 base pairs apart, thus FRET was possible only when the DNA was reconstituted into a nucleosome. One of two features was added: 1) different lengths of linker DNA or 2) a GR response element (GRE) at the DNA exit of the nucleosome where the fluorophore pair was positioned. Different linker DNA lengths were created by restriction and/or ligation. Nucleosomes were assigned according to their linker lengths with the acceptor dye positioned at the nucleosomal exit near the first linker; e.g nucleosome 39-12 has 39 bp of linker DNA on the Atto647N side and 12 bp of linker DNA on the opposite side. The GRE was inserted through a modified primer at the PCR step (see Supplement for primers and protocols). All nucleosomes were reconstituted by salt gradient dialysis from 2 M to 0 mM NaCl overnight. DNA was mixed with human recombinant histones in a titration of molar ratios ranging from 1:1 to 1:3. Only titrations where no unreconstituted DNA substrates were detected after gel electrophoresis were used for spFRET experiments. Measurement buffers contained 10 mM Tris and 1 mM NaCl, unless stated otherwise. For spFRET burst experiments

nucleosomes were diluted to 80 pM. Nucleosome concentrations in FCS measurements were between 3 and 7 nM. Samples of 20 to 40 μl were placed in a closed flowcell to minimize evaporation. After addition of NaCl, samples were incubated for 2-3 minutes before starting FCS measurements.

4.3.2 Single-molecule fluorescence spectroscopy

Measurements were performed on a home-built confocal microscope with a water-immersion objective (60x, NA 1.2, Olympus), using an ICHROME MLE-SFG laser module (Toptica) as excitation source. The excitation beam was directed via fiber coupler and a dichroic mirror (z514/640rpc, Chroma) through the objective and focused 50 μm above the glass-sample interface. Fluorescence was spatially filtered with a 50 μm pinhole in the image plane and split by a second dichroic mirror (640dcxr, Chroma). The fluorescent signals were further filtered (hq570/100nm and hq700/75nm, for green and red detection resp.) and focused on the active area of single photon avalanche photodiodes (SPADs, SPCM AQR-14, Perkin Elmer). The photodiodes were read out with a TimeHarp 200 photon counting board (Picoquant), and the arrival times were stored in t3r (time-tagged to time-resolved) files. These files were further processed with home-built Python analysis programs based on PyCorrelate[133]. spFRET experiments were done by alternating 514 (60 μW) and 632 nm (60 μW) 25 μs excitation pulses with no intermittent dark periods (alternating laser excitation, i.e. ALEX mode). Data was collected in ALEX-spFRET measurements for 30 to 60 minutes, in which 4000 - 8000 bursts were detected. FCS experiments were performed in pulsed interleaved excitation (PIE) mode by alternating 514 (30 μW) and 632 nm (20 μW) 100 ns excitation pulses with 300 ns intermittent dark periods. PIE-FCS measurements were done for a least 60 minutes, in recordings of 10 minutes.

4.3.3 Burst analysis

The FRET efficiency and stoichiometry were determined from the intensities of photon bursts associated with the donor (I^D) and acceptor (I^A) emission, and FRET signal from the acceptor (I^F). FRET and acceptor bursts were corrected for spectral leakage (α) and direct excitation (δ)[200]. To correct for differences in quantum yield, excitation intensities and detectors (γ),

the FRET efficiency E and stoichiometry S were calculated for each burst as

$$E = \frac{I^F}{I^F + \gamma \cdot I^D} \quad (4.12)$$

and

$$S = \frac{I^F + \gamma \cdot I^D}{I^F + \gamma \cdot I^D + I^A} \quad (4.13)$$

The bursts representing nucleosomes containing both fluorophores ($0.2 < S < 0.8$) were selected and fitted with a double Gaussian. We used the FRETbursts toolkit developed by Ingargiola et al.[133] to calculate E and S and to generate E, S -histograms. We found little variation in the correction factors for all experiments: α : 0.15 ± 0.03 , δ : 0.1 ± 0.01 , and γ : 1.3 ± 0.1 .

4.3.4 Averaged fluorescence intensity analysis

Fluorescence intensity of PIE-FCS measurements of nucleosomes in increasing salt concentrations were first averaged over time (number of photons per second). After corrections for background intensity and spectral leakage the average FRET efficiency was calculated from the average intensities similar to equation 4.10:

$$\langle E \rangle = \frac{\langle I_{514}^R \rangle}{\langle I_{514}^R \rangle + \langle I_{514}^G \rangle} \quad (4.14)$$

and plotted as a function of the NaCl concentration. The result was fitted with the Hill function to investigate the cooperativity of the electrostatic interactions in the nucleosome:

$$\langle E_H \rangle = \langle E_{min} \rangle + \frac{\langle E_{max} \rangle - \langle E_{min} \rangle}{1 + ([X^+]/c_{1/2})^{-H}} \quad (4.15)$$

where E_{min} is the bottom asymptote of the average FRET efficiency and E_{max} the top asymptote, $c_{1/2}$ the concentration of NaCl where 50% of the maximal average FRET efficiency is observed The Hill coefficient H indicates the cooperativity of the DNA-histone interactions in the presence of increasing NaCl concentration.

4.3.5 FCS analysis

We used the Python pycorrelate module developed by Ingargiola et al.[133] to calculate all correlation curves. The correlation algorithm used in this module was developed by Laurence et al.[134]. The algorithm is based on rewriting the correlation as a counting operation on photon pairs and can be used with arbitrary bin widths and spacing.

Parameter a (eq. 4.8) is the ratio between the axial and radial dimensions of the confocal volume and was determined through calibration experiments to be 8. Post-fit corrections were done to correct for the effects of background intensity, spectral leakage, the difference of confocal volume for different excitation wavelengths and imperfect volume overlap due to misalignment[138][139] on the number of nucleosomes. From the corrected numbers of open and closed nucleosomes we calculated the equilibrium constant K (eq. 4.2). Kinetic rates $k_{opening}$, $k_{closing}$ were determined by fitting eq. 4.7 to G_{514}^R/G_{632}^R . K_{el} , K_0 and m were found by fitting eq. 4.5 to K . c_0 was calculated by taking the intersect of K_{ind} with $K_{el} \cdot [Na^+]^m$. Error bars in all graphs show the standard deviations from $N > 5$ measurements.

4.4 Results

4.4.1 Nucleosome conformation at low NaCl concentration

To determine the intrinsic equilibrium constant for nucleosome breathing nucleosome 39-12 was measured in spFRET-ALEX at picomolar concentration. The corrected E, S -histogram in Figure 4.1b highlights the population of bursts containing both fluorescent labels ($0.2 < S < 0.7$). The FRET distribution of these bursts was fitted with a double Gaussian and revealed a high-FRET population (69%) centered around $E = 0.5 \pm 0.2$ (center \pm width) containing 3202 bursts. The low-FRET population was at $E = 0.04 \pm 0.15$ and contained 1404 bursts. The ratio of the high-FRET and low-FRET bursts yielded $K_{eq} = 0.4$. So, at low ionic concentration, the nucleosome is 70% of the time in the closed conformation.

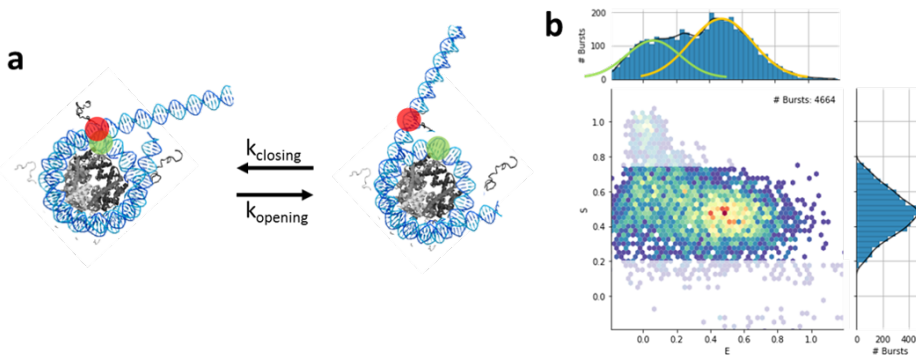


FIGURE 4.1: Burst analysis of spFRET-ALEX measurement reveals the closed state as the preferred conformation of nucleosome 39-12 at low NaCl concentration. a) Nucleosomes switch between an open and a closed conformation; when closed, the nucleosome is more compacted and FRET occurs. b) The E, S -histogram of a spFRET-ALEX measurement on nucleosomes as depicted in a) shows the majority of the bursts to have a high FRET value ($E = 0.48$). A double Gaussian fit reveals the low FRET population around $E = 0.04$. The high FRET population accounted for 3202 bursts and consisted of 69% of all bursts.

4.4.2 Electrostatic interactions in nucleosome 39-12

Nucleosome 39-12 was diluted to nanomolar concentration in 10 mM Tris and NaCl was titrated up to 50 mM. The fluorescence signals of the labels were acquired in PIE-FCS measurements to quantify the concentration and diffusion of the nucleosome and the rates of nucleosome opening and closing.

Figure 4.2a shows a difference in number of nucleosomes in the closed conformation at 6 mM and 36 mM NaCl. At 6 mM NaCl, the equilibrium constant was approximately 0.5. At 36 mM NaCl, K_{eq} increased to 2. Correlation curves were normalized by the number of nucleosomes detected in the the 632R channel for comparison. The effect of NaCl on the equilibrium is depicted in Figure 4.2b; the opening rate (bold arrow) increased, while the closing rate (slim arrow) decreased. Cations like Na^+ compete with positive residues on the histones to bind to the negatively charged linker DNA, decreasing nucleosome compaction.

Figure 4.2c shows a decline of average FRET efficiency $\langle E \rangle$ at NaCl concentrations between 10 mM and 30 mM NaCl. In that same range the increase *cq.* decrease in open and closed fractions of nucleosomes seemed to be linear (Figures 4.2d and 4.2e).

K_{eq} , the ratio of the open and closed nucleosome fractions, was fitted with equation 4.6. This yielded a salt-independent equilibrium K_0 of 0.71, a transition concentration c_0 of 20 mM, and salt stoichiometry m of 3.6 ion pairs (see also table 4.1).

To produce the data for the panels of Figure 4.3, equation 4.10 was fitted to G_{514}^R/G_{632}^R of each measured concentration of NaCl. Figure 4.3a shows a typical G_{514}^R/G_{632}^R curve plus fit at 2 mM NaCl. The larger standard deviations for τ smaller than 0.1 ms were caused by photophysics and afterpulsing, at $\tau > 50$ ms the timescale exceeded the nucleosome diffusion time, resulting in large errors due to the division of small values. For NaCl concentrations lower than 30 mM, nucleosome 39-12 opened 17 times per second and closed 32 times per second, corresponding to an open time of 31 ms and a closed time of 58 ms. The accompanying equilibrium constant (Figure 4.3d) $K_{eq} = 0.53$ was similar to the value we found through spFRET burst analysis (0.43). At $[\text{NaCl}] = 25$ mM, a drop occurred for K_{eq} . This seemed to be caused by a decrease of the closing rate to 10 s^{-1} while the opening rate remained 40 s^{-1} . For higher NaCl concentration we saw opening rates increasing significantly, with closing rates remaining

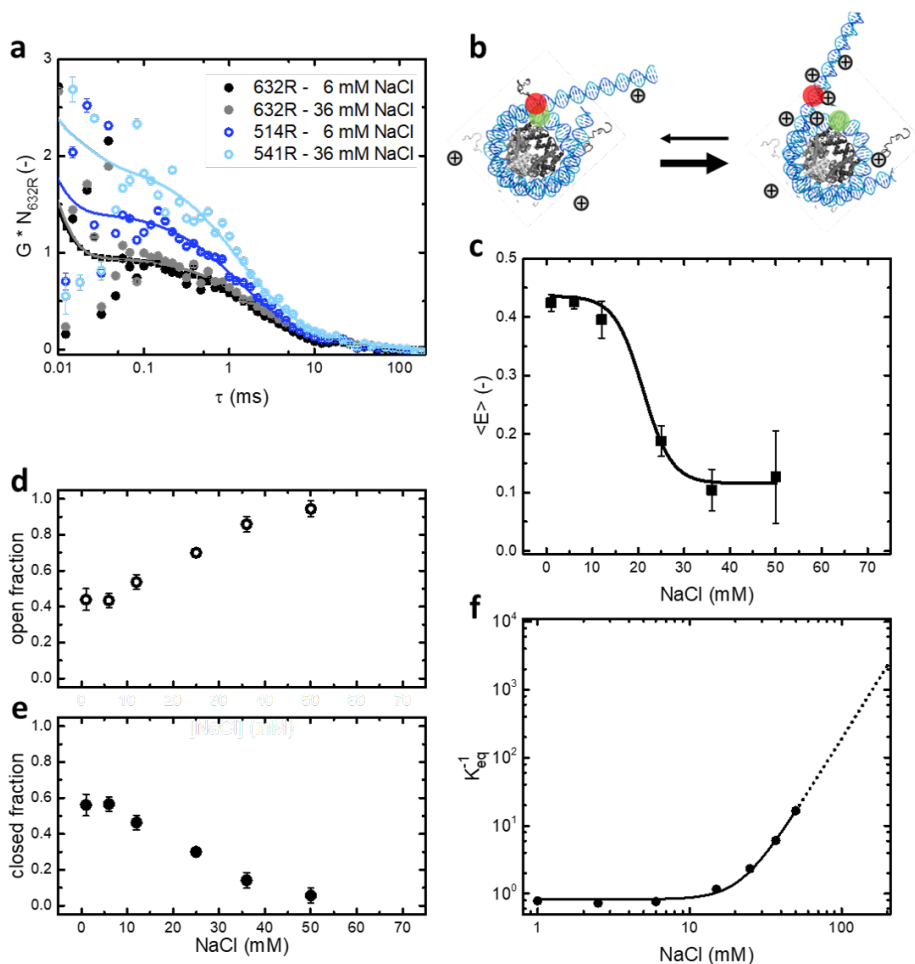


FIGURE 4.2: **Increasing NaCl concentration drives nucleosome 39-12 to the open conformation.** **a)** Autocorrelation curves of nucleosome 39-12. At 6 mM NaCl the ratio between open and closed states was 1:2. At 36 mM NaCl the ratio was 2:1. **b)** Representation of the ion distribution around the nucleosome. **c)** Increasing [NaCl] lowers the average FRET efficiency non-linearly. Fitting gave $c_{1/2} = 21 \pm 1$ mM and Hill coefficient: 0.14 ± 0.03 . **d)** and **e)** Fractions of open and closed nucleosomes increased cq. decreased approximately linearly with the NaCl concentration. **f)** Fitting eq. 4.4 to K_{eq} gave $K_0 = 1.2 \pm 0.07$ and $m = 3.6 \pm 0.1$; c_0 was 20 mM, resembling $c_{1/2}$ of the Hill fit.

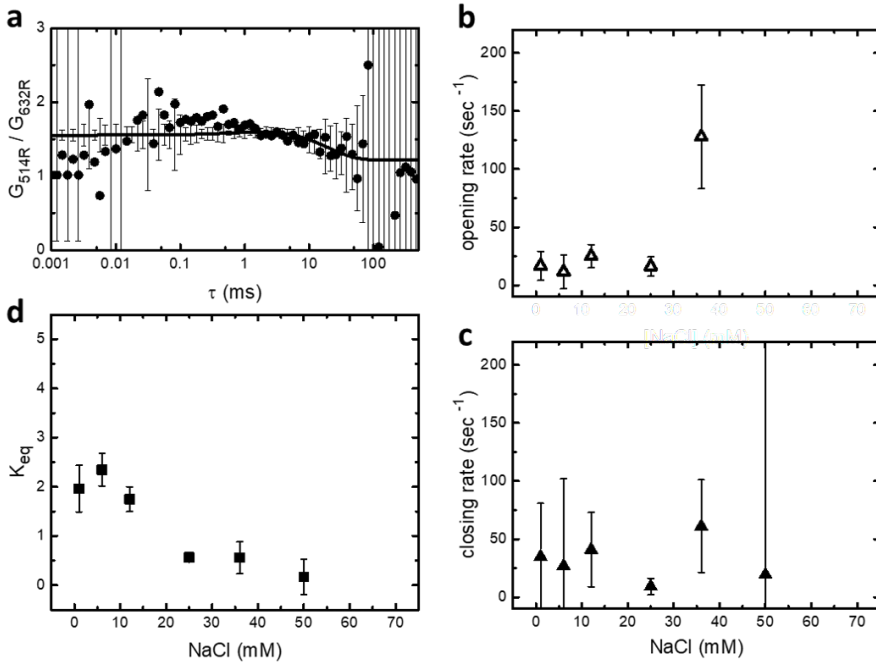


FIGURE 4.3: **Increasing NaCl concentration increased the opening rate; the closing rate remained constant. a)** Dividing ACF 632R by ACF 514R cancels out the diffusional contributions to the curves, the remaining curve represents switching between the open and closed state. **b)** and **c)** Above 30 mM NaCl, the opening rate increased significantly from an average of 17 s^{-1} , to 130 s^{-1} . At 50 mM $k_{opening} = 1227 \text{ s}^{-1}$ and $k_{closing} = 32 \text{ s}^{-1}$. **d)** K_{eq} shows an abrupt drop around 20 mM NaCl, concurring with $c_{1/2} = 21 \pm 1 \text{ mM}$.

constant. However, the errors in the fits were relatively large. Nevertheless, the change in K_{eq} at 25 mM NaCl was confirmed by the dynamics analysis, providing credibility to this analysis, despite the relatively large error.

4.4.3 Effects of linker DNA

In chromatin, a nucleosome is flanked by linker DNA of different lengths[179][180]. To test whether the length of the linker DNA has an effect on nucleosomal dynamics we prepared nucleosomes 26-5, 39-100 and 300-12 in addition to nucleosome 39-12. The first number represents the number of base pairs at the exit where the fluorophore pair was positioned, the second number represents the number of base pairs at the opposite exit. The nucleosome dynamics at low salt concentration was first characterized by spFRET burst analysis. Fitting the bursts of nucleosome 26-5 as shown in the E, S -histogram in Figure 4.2a yielded a high-FRET fraction of 77 % around $E = 0.42 \pm 0.2$ which contained 2893 bursts (77% of total). The low-FRET fraction was found at $E = 0.05 \pm 0.07$. Compared to nucleosome 39-12, the fractions of 26-5 were better separated in the E, S -histogram. The bursts of nucleosome 39-100 appeared more convoluted in Figure 4.4b. Note that this is the only nucleosome that we tested which had linkers long enough to cross in the closed conformation, bringing the DNA arms in close proximity. Fitting a double Gaussian resulted in a low-FRET population at $E = 0.08 \pm 0.14$ and a high-FRET population at $E = 0.47 \pm 0.2$, which consisted of 77% of the 3274 bursts. The E, S -histogram of nucleosome 300-12 displayed two clearly defined populations of bursts (Figure 4.4c). The high-FRET population consisted of 3551 bursts (65%) with $E = 0.44 \pm 0.2$. For the low-FRET population we fitted $E = -0.03 \pm 0.1$. Nucleosome 300-12 thus had the smallest high-FRET population, followed by 39-12 with 69%. Nucleosomes 26-5 and 39-100 both had 77% of open nucleosomes. Next to characterizing FRET efficiency E and label stoichiometry S , defining the low- and high-FRET populations enabled us to compute the burst widths of these populations. Figure 4.4d shows that the low-FRET fractions of 26-5 and 39-12 had longer burst widths compared to their high-FRET counterparts. For 39-100 the opposite applies; the low-FRET fraction is 0.5 ms faster than the high-FRET fraction. This suggests that 39-100 nucleosomes were more compacted in a low-FRET conformation. This could be because the 39 base pair linker is unwrapped and the 100 base pair linker wraps towards the histone core. The burst widths of the low- and high-FRET fractions of nucleosome 300-12 are equal. The diffusion of this nucleosome in both open and closed state would be dominated by the 300 base pair DNA linker, which was 10 times larger compared to the diameter of the nucleosome core (100 nm versus 10 nm). The difference in

diffusion times was also visible in the autocorrelation curves of the FRET signal (channel 514R) shown in Figure 4.5a. The shift to larger τ for longer nucleosomes indicated that diffusion time depends on the length of the linker DNA. The salt dependence of the average FRET efficiency $\langle E \rangle$ also depended on the linker DNA, but in a different way. Figure 4.5b shows the FRET efficiency of 39-100 nucleosomes dropped off first, followed by that of 300-12, 39-12 and last 26-5. This means that not only the length of linker DNA, but also the proximity of both linkers (i.e., crossing linker DNA) had a significant effect on nucleosome stability. Fitting the Hill function resulted in $c_{1/2}$'s of 24 ± 4 mM for 26-5, 21 ± 1 mM for 39-12, 13 ± 1 mM for 39-100 and 22 ± 2 mM (300-12). The Hill coefficient showed negative cooperativity for all nucleosomes: 0.05 ± 0.02 (26-5), 0.14 ± 0.03 (39-12), 0.1 ± 0.02 (39-100) and 0.12 ± 0.06 (300-12). Thus unwrapping becomes increasingly unlikely as more DNA unwraps. It should be noted that the Hill coefficient heavily depends on the highest and lowest value of $\langle E \rangle$ for each titration. We observed a difference in average FRET efficiency of the nucleosomes at low salt concentration.

At low NaCl concentration, nucleosomes 26-5, 39-12 and 300-12 all had a closed fraction of ~ 0.6 , despite having different average FRET efficiencies. Nucleosome 39-100 had the highest fraction of closed nucleosomes (~ 0.8), an indication that the crossed linker DNA contributed to nucleosome compaction in the absence of cations. The shortest linker DNA had the weakest dependence on NaCl concentration, indicating that electrostatic interactions between the linker DNA and the histones stabilize the nucleosome.

Fitting the number of additional ion pairs m that bind to the nucleosome in the open state quantified this observation. Nucleosome 39-100 had the highest equilibrium constant K_0 (3.8), and 2.3 ± 0.1 ion pairs bound at the lowest transition concentration c_0 of 13 mM NaCl. There appeared to be a trend for both m and c_0 ; with increasing linker DNA. The number of bound ions increased from 3.3 ± 0.1 for 26-5, 3.6 ± 0.1 for 39-12 to 4 ± 0.1 for 300-12. The transition concentration decreased from 35 ± 0.02 mM for 26-5, 22 ± 0.04 mM for 39-12 to 20 ± 0.01 mM for 300-12. The increase in bound ions implies that more cations were needed to replace the interactions between histones and DNA when more linker DNA was available in the nucleosome. The decreasing trend for the transition concentration also implies a stronger dependence of nucleosome stability on salt concentration.

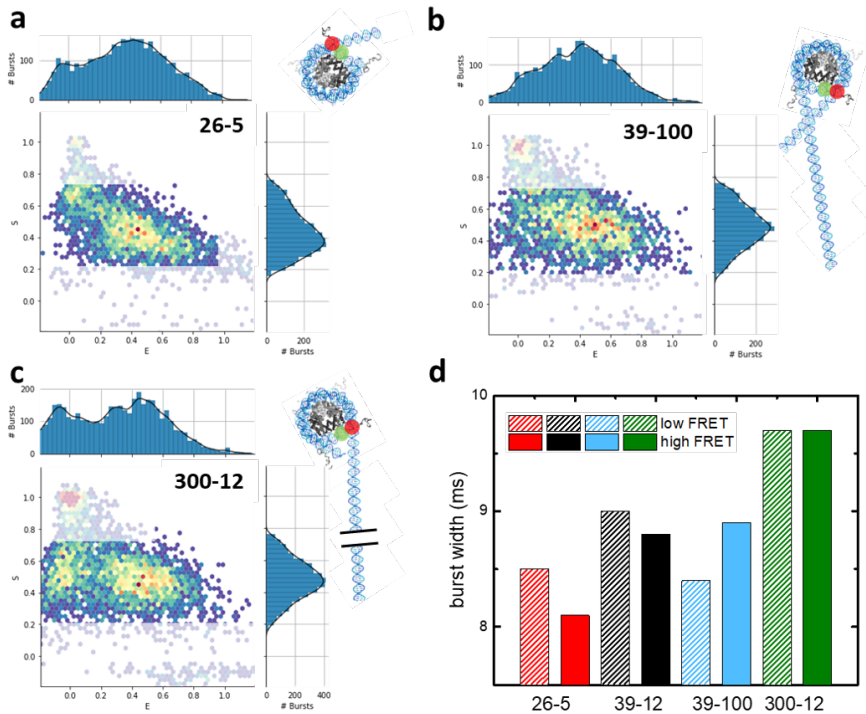


FIGURE 4.4: Long linker DNA shifts the nucleosome equilibrium to the closed conformation at low NaCl concentration. a) Nucleosome 26-5 has a larger closed population than nucleosome 39-12; K_{eq} was close to 0.5. **b)** Nucleosome 39-100 featured a small low FRET population and a wider high FRET population, with K_{eq} close to 0.5. **c)** Nucleosome 300-12 yielded $K_{eq} = 0.9$. **d)** The low FRET fractions of 26-5 and 39-12 had a longer burst width caused by a slower diffusion when the nucleosomes are in an open conformation. The burst width of the low FRET population of nucleosome 39-100 was smaller compared to the burst width of the high FRET population. The low and high FRET burst widths for 300-12 are both 9.7 ms.

It can be argued that when histone-linker DNA interactions are disrupted by cations at one position of the linker DNA, the chance for the histone tails to bind to another part of the linker DNA increases. More linker DNA in the nucleosome will then increase the overall chance of histone-DNA interactions taking place at any time, thereby increasing the total energy needed to disrupt these interactions.

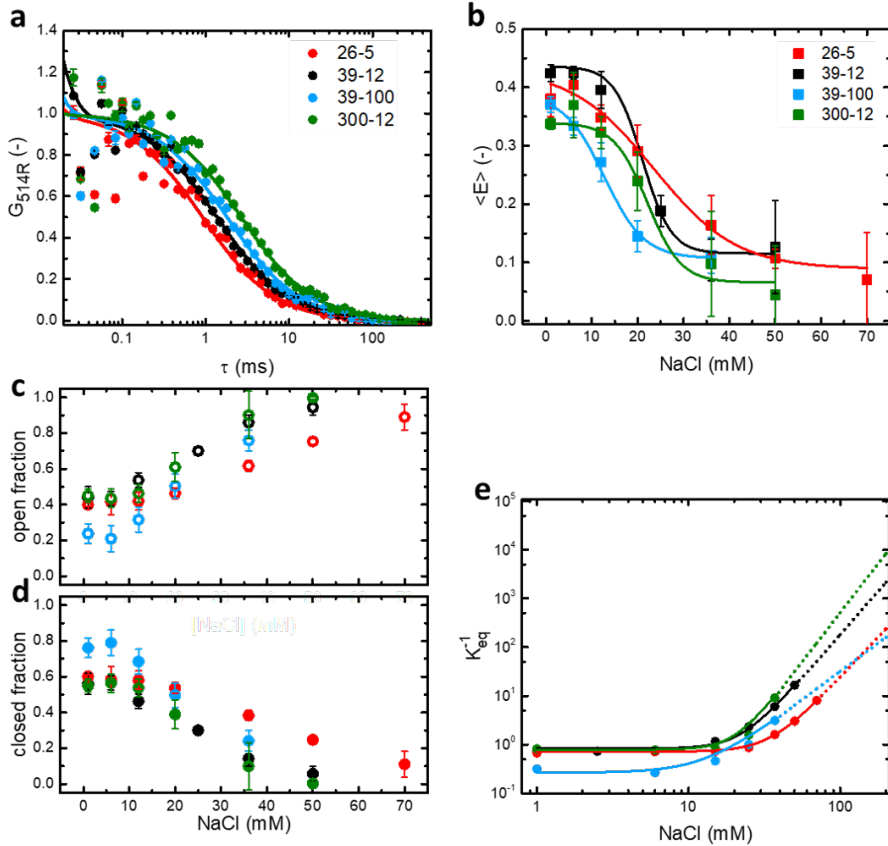


FIGURE 4.5: Crossing linker DNA increases nucleosome compaction at low NaCl concentration. At increasing NaCl concentration the nucleosome with shorter linker DNA remains compacted longer. **a)** The increasing diffusion times of the nucleosomes depend on the length of their linker DNA. **b)** The average FRET shows that at increasing NaCl concentration, nucleosome 26-5 takes the highest NaCl concentration to unwrap, 39-100 the lowest. **c)** and **d)** show for all nucleosomes an approximately linear decrease of the closed and open fractions. **e)** Fitting K_{eq} shows that all nucleosomes except 39-100 had a similar K_0 ; the slopes yielded $m = 2.3$ for 39-100, 3.3 for 26-5, 3.6 for 39-12 and 4 for 300-12 (see also Table 1).

When 514R autocorrelation curves were divided by 632R autocorrelation curves the results exhibited large standard deviations for values of τ smaller than 0.1 ms and larger than 50 ms (Figure 4.6a-d). These large standard deviations should be attributed to spectral characteristics of the fluorophores and the small number of molecules that remain in focus for long times, and were not caused by nucleosome dynamics. Nevertheless, the equilibrium constants calculated from these curves (Figure 4.6e) showed a trend similar to the decrease of the closed nucleosome fractions (Figure 4.5d).

At low salt concentration, nucleosome 39-100 had the highest, and nucleosome 300-12 had the lowest value of K_{eq} ; increasing NaCl decreased all equilibrium constants, with the K_{eq} of nucleosome 26-5 decreasing slowest. The opening rates of nucleosomes 26-5, 39-12 and 39-100 increased from less than 50 s^{-1} at NaCl concentrations lower than 20 mM to rates of several hundreds per second above this concentration. For nucleosome 300-12 $k_{opening}$ remained stable around $13 \pm 7 \text{ s}^{-1}$. The closing rates did not seem to increase with NaCl concentration within the error margins. For NaCl concentrations below 20 mM both nucleosome 26-5 and nucleosome 39-100 had a twice as high $k_{closing}$ compared to nucleosome 39-12 and nucleosome 300-12 (more than 100 s^{-1} versus less than 50 s^{-1}). Higher closing rates (nucleosomes 26-5 and 39-100) were associated with a smaller number of bound ions ($m = 3.3$ for 26-5 and $m = 2.3$ for 39-100). The opposite also held; nucleosome 300-12 had the slowest closing and opening rates and a larger number of associated ions ($m = 4$).

nucleosome	K_X (-)	m (-)	K_0 (-)	c_0 (mM)
26 – 5	$5.4 \pm 1.8 \cdot 10^{-6}$	3.3 ± 0.1	0.71 ± 0.03	34.6 ± 0.02
39 – 12	$1.3 \pm 4.6 \cdot 10^{-6}$	3.6 ± 0.1	0.83 ± 0.07	22.1 ± 0.04
39 – 100	$6.6 \pm 3.3 \cdot 10^{-4}$	2.3 ± 0.1	0.26 ± 0.04	12.8 ± 0.02
300 – 12	$4.3 \pm 1.6 \cdot 10^{-6}$	4.0 ± 0.1	0.77 ± 0.02	20.1 ± 0.01

TABLE 4.1: Crossed linker DNA decreases ionic dependence of nucleosome stability (decrease in m , number of broken ion pairs) short linker DNA shifts equilibrium transition (c_0) to higher NaCl concentration.

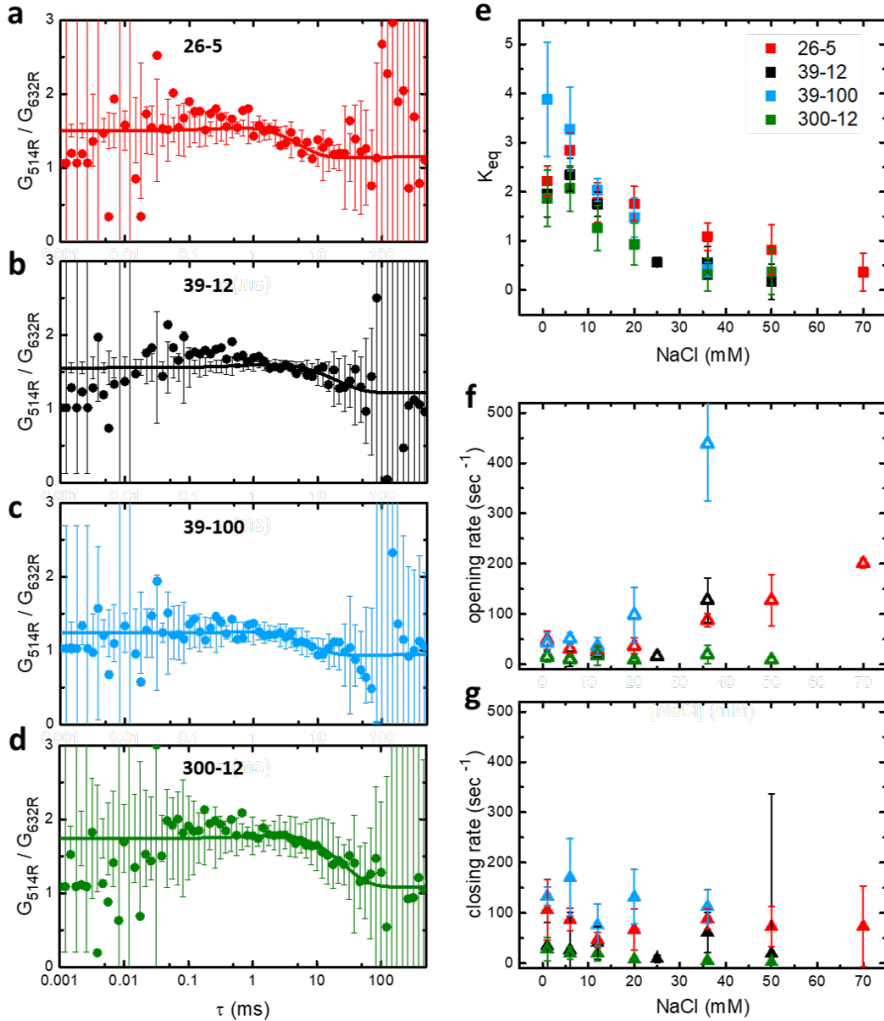


FIGURE 4.6: Crossed or short linker DNA increased the closing rate at low NaCl concentration, one very long DNA linker decreased both closing and opening rates. a), b), c) and d) are characteristic plots of the dynamics correlation curve for all nucleosomes. e) K_{eq} increased for NaCl > 6 mM for all nucleosomes. f) Opening rates of nucleosomes 26-5, 39-12 and 39-100 increased at increasing NaCl; $k_{opening}$ of nucleosome 300-12 remained stable. g) The closing rates of all nucleosomes did not change significantly upon increasing NaCl concentration.

4.4.4 Effects of nucleosomal DNA sequence

Specific protein recognition sites tend to be enriched at locations in or near DNA exiting from nucleosomes[191][193][194][195]. To resolve the effect of the positioning of such recognition sites relative to the nucleosome, we altered the Widom 601 sequence of nucleosome 39-12 by incorporating a Glucocorticoid Response Element at 3 different positions (GRE1, GRE2 and GRE3).

Figure 4.7a shows the locations of these sites in the nucleosome. GRE1 was located in two major grooves around SHL -5.5; GRE2 was shifted 5 base pairs into the nucleosome, at two minor grooves (SHLs -5.5 and -4.5); GRE3 was shifted another 5 base pairs, ending up predominantly at two major grooves (SHL -4.5). GRE1 differed 7 base pairs from the 601 template, GRE2 and GRE3 both differed 11 base pairs. We expected GRE2 to show the largest difference with 601 in terms of nucleosome stability and accessibility, since the GRE positioning in the minor grooves is associated with a longer binding time of the GR protein[95]. We anticipated a smaller effect of GRE1. GRE3 was positioned further into the nucleosome which may reduce the effect on nucleosomal breathing dynamics.

However, the only apparent difference in the average FRET efficiency was at high NaCl concentrations (figure 4.7b) At high salt, GRE1 and GRE2 had lower FRET efficiencies compared to 601 and GRE3. Fitting the Hill function gave similar values for $c_{1/2}$ for all nucleosomes: 21 ± 1.1 mM (601), 19 ± 2 mM (GRE1), 21 ± 0.6 mM (GRE2) and 19 ± 0.2 mM (GRE3).

The Hill coefficients were also very similar: 0.14 ± 0.03 (601), 0.1 ± 0.13 (GRE1), 0.1 ± 0.01 (GRE2) and 0.15 ± 0.006 (GRE3), and showed negative cooperativity. All nucleosomes showed a similar decrease in their fractions of closed nucleosomes. Fitting K_{eq} revealed that nucleosomes 601 and GRE1 had the highest number of bound ions with $m = 3.6 \pm 0.1$ (601) and $m = 3.7 \pm 0.1$ (GRE1). GRE2 bound ions less strongly ($m = 2.7 \pm 0.04$) and GRE3 featured the smallest m : 2.0 ± 0.2 . The trend appeared to be that the closer a mutation was located towards the dyad of the nucleosome, the larger its effect on nucleosomal stability.

The transition concentrations showed that nucleosomes 601 and GRE1 were the most stable (c_0 at 22 ± 0.04 mM and 23 ± 0.06 mM) GRE3 less (18 ± 0.12 mM), and GRE2 the least stable (14 ± 0.03 mM). This implied that nucleosome GRE2 should have higher opening and/or smaller closing rates, compared to nucleosome 601. Because nucleosome GRE1 had similar values

of c_0 and m , and we expected it would have similar dynamics as 601. The ratio of the autocorrelation curves 514R and 632R at 1 mM NaCl, shown in Figures 4.8a-d, did not reveal large differences between the nucleosomes. Figure 4.8e shows that at NaCl concentrations smaller than 20 mM, nucleosomes 601 and GRE1 had slightly higher equilibrium constants than nucleosomes GRE2 and GRE3, implying the first to be closed more often or for a longer period of time.

The transition rates confirmed this: Figure 4.8f showed that the opening rates of nucleosomes 601, GRE1 and GRE3 increased with increasing NaCl concentration. Like nucleosome 601, GRE3 had an opening rate of around 30 s^{-1} below 25 mM NaCl, but increased less steep as salt increased compared to nucleosome 601. The opening rates of nucleosome GRE1 seemed to increase linearly from $\sim 25\text{ s}^{-1}$ (1 mM NaCl) to $\sim 120\text{ s}^{-1}$ above 20 mM NaCl. The opening rates of nucleosome GRE2 were larger and decreased only marginally from $79 \pm 9\text{ s}^{-1}$. The steep decrease of the closing rate of nucleosome GRE2 was most obvious from Figure 4.8g; from faster than 150 s^{-1} at 1 mM NaCl to slower than 50 s^{-1} above 20 mM NaCl. Nucleosome GRE3 appeared to have similar closing rates as nucleosome 601 of $\sim 40\text{ s}^{-1}$, nucleosome GRE1 was closing more frequently at 60 s^{-1} . The higher opening and closing rates of nucleosome GRE1 could be related to the slightly lower average FRET efficiency shown in Figure 4.7b; when a nucleosome opened and closed more often, it may not wrap back completely to the histone core, leaving a larger distance between the FRET pair. The number of altered base pairs did not seem to have an effect on nucleosome breathing; the location of the mutation caused the largest differences in nucleosomal stability.

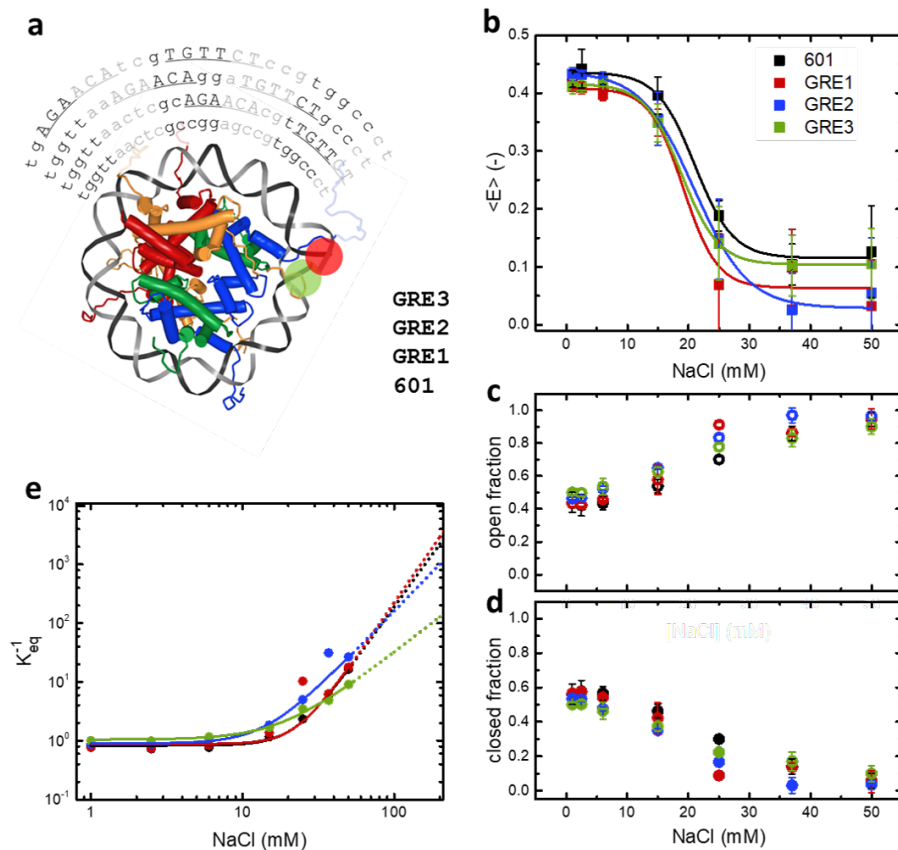


FIGURE 4.7: DNA sequence has a small effect on nucleosome breathing. **a)** Glucocorticoid Response Elements GRE1 and GRE3 were located in major grooves (colored dark grey), GRE2 was introduced in two minor grooves (colored light grey). **b)** The FRET efficiency as a function of salt concentration did not reveal significant differences between all constructs. **c)** and **d)** All nucleosomes had a similar salt dependence for closed and open fractions. **e)** Fitting K_{eq} did reveal small effects of the GRE mutations: m decreased from 601 to GRE3. Concentration c_0 showed that nucleosomes 601 and GRE1 were most stable.

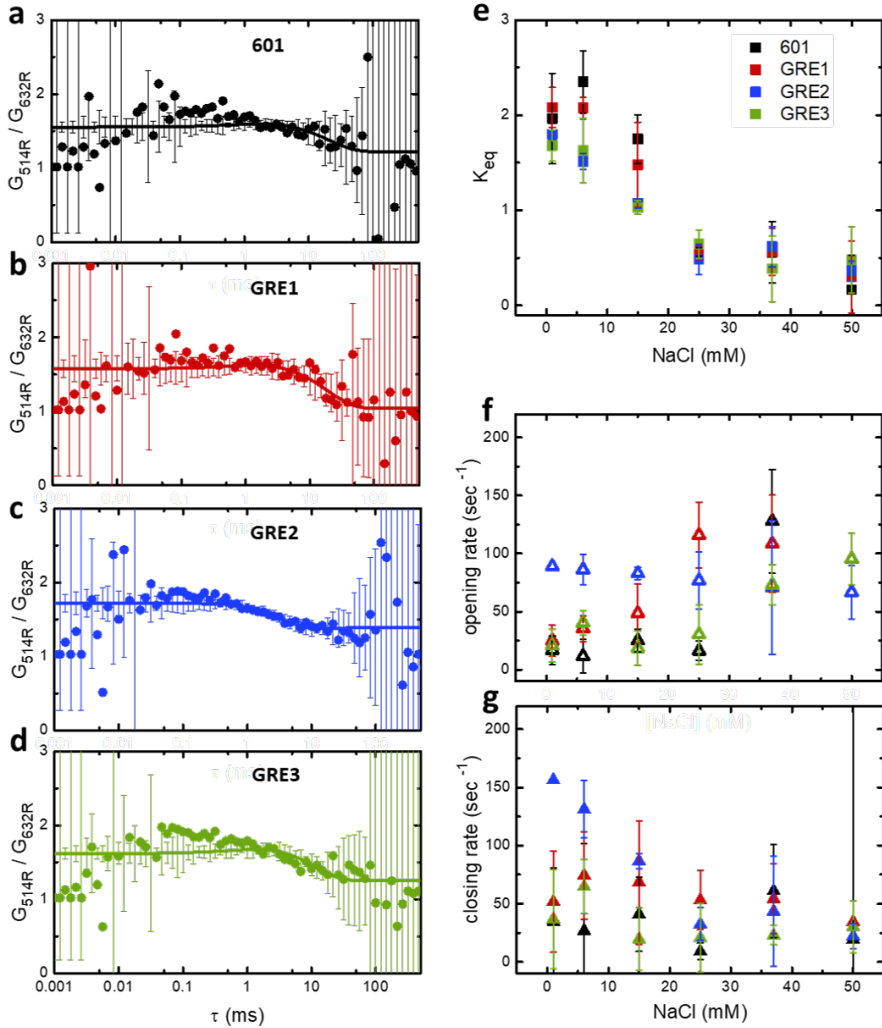


FIGURE 4.8: Mutation in the minor grooves and close to the exit changed nucleosome dynamics most. a), b), c) and d) show the ratio of 514R and 632R autocorrelation curves for different nucleosomes. e) K_{eq} from fitting the relative correlation curves decreased for increasing [NaCl]. f) and g) Nucleosome GRE2 showed significantly different salt-dependent dynamics.

nucleosome	$K_X(-)$	$m(-)$	$K_0(-)$	$c_0(\text{mM})$
601	$1.3 \pm 4.6 \cdot 10^{-6}$	3.6 ± 0.1	0.83 ± 0.07	22.1 ± 0.04
GRE1	$6.9 \pm 3.7 \cdot 10^{-6}$	3.7 ± 0.1	0.87 ± 0.11	22.8 ± 0.06
GRE2	$7.6 \pm 1.1 \cdot 10^{-4}$	2.7 ± 0.04	0.89 ± 0.05	14.2 ± 0.03
GRE3	$3 \pm 7 \cdot 10^{-3}$	2.0 ± 0.2	1.04 ± 0.21	18.2 ± 0.12

TABLE 4.2: The most inward mutation (GRE3) has the biggest effect on the nucleosomes' stability, a mutation in the minor grooves (GRE2) affects the equilibrium transition most.

4.4.5 Effects of buffer composition

When studying nucleosomes, other factors that stabilize the nucleosome are often added to the buffer to increase stability[176] or decrease surface interactions[53]. The effect of the additive itself on stability and dynamics is however rarely mentioned. There is no consensus on a standard buffer composition for nucleosome dynamics studies, which makes comparing experiments non-trivial. Here we have studied the effect of tris(hydroxymethyl)aminomethane (Tris) and nonionic detergent octylphenoxypolyethoxyethanol (known as Igepal-CA 630) which are added to increase nucleosome stability. We also tested the effect of Vitamin C, which enhances photostability through reduction of blinking of the fluorophores. However, we did not find a significant difference in photon signals when Vitamin C was added. Figure 4.9a shows the addition of 0.02% NP40 (and 1mM Vitamin C) reduced the diffusion time of a 39-12 nucleosome almost twofold; it decreased opening and closing rates 3-4 times, and increased the equilibrium constant from 0.47 to 0.29 (see also Table 3). Increasing the Tris concentration showed a slower decrease of the FRET efficiency than increasing [NaCl] (Figure 4.9d). FRET remained stable for Tris concentrations below 20 mM and decreased in a linear fashion for higher concentrations. Fitting the observed equilibrium constant yielded an equilibrium K_0 similar to the one found in NaCl titration: 0.9 ± 0.15 (Tris) and 0.83 ± 0.07 (NaCl). For Tris the value of m was 7.55 ± 0.55 , suggesting the effective charge of Tris to be half that of monovalent Na. The transition concentration c_0 was also higher at 29 ± 0.1 mM Tris (22 ± 0.04 mM for NaCl), implying less effective interactions with the nucleosome.

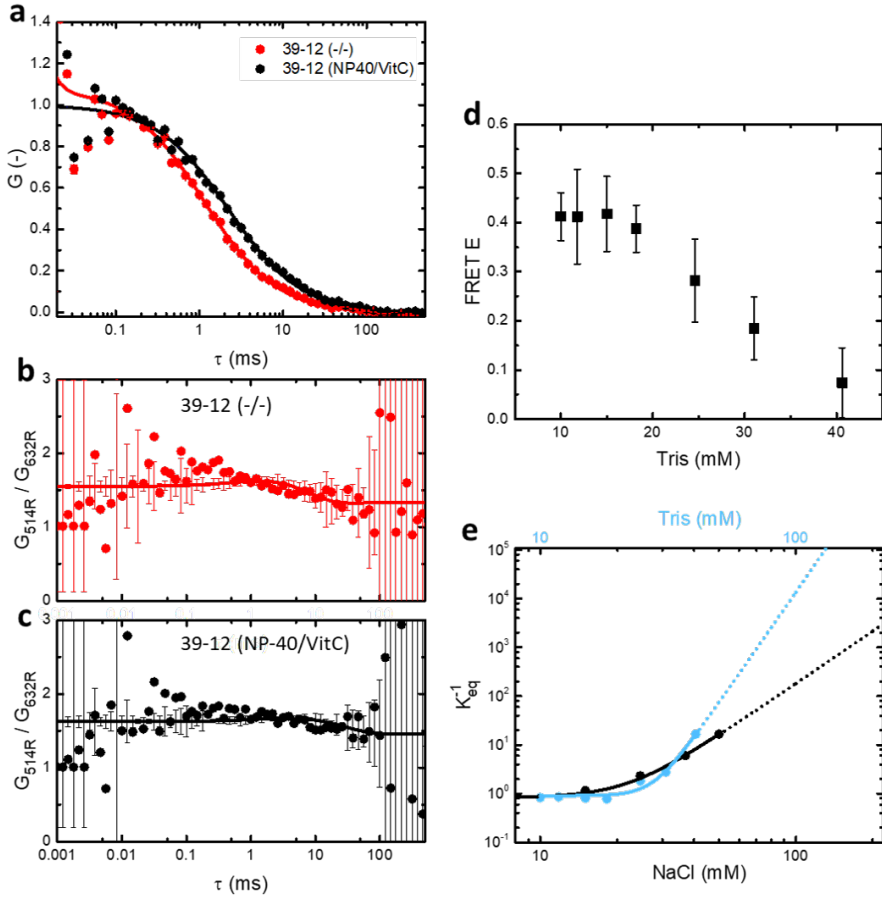


FIGURE 4.9: Buffer additives have a substantial impact on both stability and dynamics of the nucleosome. **a)** Addition of 0.02% NP40 and 1mM Vitamin C slowed the average diffusion time of a nucleosome almost twofold. **b)** and **c)** Characteristic plots of the ratio of the 514R and 632R autocorrelation curves of 39-12 without (b) and with (c) NP40 and Vitamin C. **d)** Adding Tris decreased the FRET efficiency in a similar fashion as seen before with NaCl. **e)** Fitting K of the Tris titration showed an independent equilibrium K_X at a higher transition concentration x_0 .

buffer	τ_D (ms)	t_{open} (ms)	t_{close} (ms)	K_{eq}
(-/-) (ms)	1.32 ± 0.25	10 ± 12.5	21 ± 46	2.15 ± 0.47
(NP40/VitC)	2.31 ± 0.35	35 ± 19	121 ± 11	3.46 ± 0.8

TABLE 4.3: Addition of NP40 and Vitamin C decreases diffusion time as well as dynamics of the nucleosome, thereby increasing stability (K_{eq}).

4.5 Discussion and conclusions

In this chapter we quantified the dependence of nucleosomal dynamics and stability on small differences in linker DNA length or DNA sequence by combining PIE-FCS with FRET. In salt concentrations lower than physiological conditions nucleosomes preferred to be in a closed conformation. Upon increasing NaCl concentration the opening rate increased while the closing rate remained the same. DNA-histone interactions strengthened with the length of linker DNA. Surprisingly, the extension of linker DNA lowered the NaCl concentration at which the opening rates of the nucleosome started to increase.

The insertion of the Glucocorticoid Response Element (GRE) in the Widom 601 DNA sequence decreased the stability of the nucleosome when the GRE was inserted deeper into the nucleosome (i.e. towards the dyad). Except for the nucleosome with the GRE in the minor grooves, all GRE nucleosomes increased their opening rates upon increasing NaCl concentration. Positioning the GRE in the minor grooves, where it approached the histone core closer than in the major grooves, did not increase the opening rate but rather decreased the closing rates. The GRE in the minor grooves might increase the rigidity of the DNA strand, making it energetically less favourable to bend towards the histone core. Overall, positioning the GRE towards the dyad decreased the critical NaCl concentration at which equilibrium changed.

The combination of PIE-FCS with FRET allowed to differentiate between open and closed nucleosomes, yielding the equilibrium constant as well as the dynamic rates without extensive corrections. To extract the opening and closing rates from autocorrelation curves, the correlation curve generated from the FRET signal was divided with the curve from the directly excited acceptor, thereby cancelling contributions from diffusion. This method seems to be more robust than dividing correlation curves obtained from

different measurements as reported by Torres et al[198]. Though the error margins were very large at short and long lag times, the equilibrium constant that was derived from fitting the ratios of the correlation curves agreed well with the equilibrium constant derived from the ratio of the fractions of open and closed nucleosomes, validating this method.

Comparing PIE-FCS results with findings from burst analysis for nucleosomes with variable linker DNA lengths in low NaCl concentration added more insight in the effect of linker DNA on compaction. For the nucleosome with crossed linkers, burst analysis did not show a low-FRET population. PIE-FCS data confirmed that this nucleosome was almost completely closed at low ionic conditions. For constructs with crossing linker DNA burst analysis revealed a small low-FRET population, accounting for a higher fraction of open nucleosomes, again consistent with the PIE-FCS data. Quantifying the low- and high-FRET populations did not completely reflect these observations. The nucleosome with the shortest linkers had a high-FRET population comparable to the nucleosome with the crossing linkers in burst analysis, while PIE-FCS showed a closed fraction comparable to nucleosomes without crossing DNA. We argue that this discrepancy originates from the thresholds chosen in burst analysis. Setting parameters such as number of photons and intermittent photon times too narrow results in missing bursts, while setting them too wide results in overestimating the number of bursts. Also, burst analysis can only be properly performed at concentrations < 200 pM to prevent bursts overlapping. When the concentration is too low (< 10 pM) however, it becomes difficult to acquire enough statistics. Moreover, at such low concentrations one has to take into account the reduced nucleosome stability. FCS generates reliable results over several orders of magnitude of concentration (1 pM to 50 nM). Measuring at nanomolar rather than pM concentrations increases the signal to noise ratio, making it less likely to misinterpret FRET signals.

Stabilizer compounds and oxygen scavengers are common ingredients in buffers used for single-molecule experiments on nucleosomes[178][97][176]. These additives reduce the deteriorating effects of low nucleosome concentrations by stabilizing nucleosomes or enhancing emission from fluorophores. We showed however, that nucleosomal dynamics is slowed down significantly and nucleosomes are more in a closed conformation when adding NP-40 and Vitamin C. Indeed, the nucleosome breathing studied here may be the first step in dissociation

of the nucleosome. Even though we did not measure nucleosome stability as a function of increasing salt concentration in the presence of these additives, we expect that the decrease in dynamics and the shift to the closed conformation would still occur at higher salt conditions. One could argue that adding stabilizing agents better resembles the *in vivo* situation, but we want to stress that the effect of additives on dynamics and stability should be taken into consideration when comparing experiments.

In this chapter we report a relatively small range of salt concentrations, up to 70 mM, compared to work previously done by e.g. Gansen[178] and Bohm[173]. There are several reasons for our concentration cap. To quantify the changes in nucleosomal dynamics induced by small sequence and linker length changes at the nucleosomes' exit, the FRET pair was positioned at the dyad and one of the last base pairs in the nucleosome. In concurrence with previous observations, nucleosomes unwrap progressively from the exits towards the dyad[177][99]. When measuring in higher salt conditions (> 100 mM NaCl) we observed that the FRET signal was lost progressively and irreversibly and we could not follow dynamics anymore. A loss of FRET signal was also observed to a lesser degree for salt concentrations lower than 100 mM. We observed that a small fraction of the nucleosomes irreversibly unwrapped over 10-30 minutes, until an equilibrium was reached. Similar progressive unwrapping of nucleosomes has been observed by others[53][201][202] and it was suggested this form of unwrapping resulted in sub-nucleosomal particles such as hexasomes and tetrasomes, which is enhanced by diluting the nucleosomes to low (< 1 nM) concentrations. Because the positions of our FRET pair can not discriminate between open nucleosomes and partially dissociated nucleosomes, we cannot confirm this interpretation. In our measurements however, long-term progressive unwrapping did not depend on nucleosome concentration (measurements were repeated at different nucleosomes concentrations (1 - 20 nM) and same NaCl concentration). Bohm et al.[173] reported before that nucleosomes need to equilibrate for several minutes after changing salt concentration. Taking into consideration that histone-DNA binding energies cannot be determined when dissociation is irreversible[36], we did not include measurements taken immediately after adding salt. Overall, we obtained very similar results from FRET burst analysis and FCS-PIE. The latter allows for a more detailed spectral and temporal analysis though. We used this method to distinguish structurally highly similar nucleosomes.

We have shown that nucleosomes wrap their DNA more stably when more linker DNA is available, suggesting that the histone tails span out further over the linker DNA. Small changes in nucleosomal DNA sequence affect both nucleosome dynamics and stability. By combining PIE-FCS with FRET we increased robustness and accuracy of measured dynamics and conformation. Hence we are confident that our technique is also applicable on nucleosomes containing natural DNA sequences, which exhibit an even richer variety than the nucleosomes containing the Widom601 sequence used in our experiments. This finding should be taken into account when comparing the binding of transcription factors to their target sites[174][100].



H3K36ME3 DECREASES NUCLEOSOME STABILITY AND INCREASES LEDGF AFFINITY IN CHROMATIN

Posttranslational modifications (PTMs) of the histone tails are widely associated with modulation of gene expression. By altering the local charge and structure of the amino acids in histone tails through acetylation, methylation or phosphorylation, these modifications change binding affinity of proteins for nucleosomal DNA or the histone tails themselves. The trimethylation of lysine 36 in the H3 tail, H3K36me3, is associated with DNA repair and transcription as well as HIV viral DNA integration. In the latter case protein LEDGF/p75 is hijacked by a pre-integration complex (PIC) containing the viral DNA and used as a bridge to the host DNA. The interaction mechanism between LEDGF/p75, PIC and DNA is not yet completely elucidated, as is the effect of H3K36me3 on nucleosomal dynamics and stability.

We combined the results of PIE-FCCS and PIE-FCS-FRET measurements to quantify the effect of H3K36me3 on nucleosome dynamics, stability, and the affinity of LEDGF/p75 to bare and nucleosomal DNA. We used wild-type and an AT-hook deficient variant of the protein to show that the dominant factor in affinity is the H3K36me3 modification. We also quantified the decrease in nucleosomal stability caused by H3K36me3. Lastly, we propose a possible interaction mechanism based on the decrease in FRET efficiency and binding affinity measurements.

This chapter is a collaboration with:

T. Brouns, W. Frederickx, S. De Feyter, W. Vanderlinden, KU Leuven.

5.1 Introduction

The nucleosome is the first level of DNA compaction in eukaryotic cells. Compacted DNA is sterically occluded from DNA-binding proteins involved in processes like transcription and repair[203][174]. DNA accessibility is modulated by spontaneous reversible unwrapping (nucleosome breathing) and DNA remodelers[39][50], the latter being proteins and enzymes attracted to specific DNA sequences or chemical modifications of histone tails. The posttranslational modifications (PTMs) of the amino acids comprising histone tails act as markers for a myriad of DNA processes[204][205][206][207][208]. Through covalent binding a chemical functional group is added or modified, thereby changing the local charge density or conformation of the amino acid, or both. The modifications alter the affinity for proteins to the histone tail and consequently to the nearby compacted DNA[209][210].

Although the role of PTMs in cellular processes is understood on a causal level, the underlying mechanisms are less clear[211][212][213][214]. This hiatus in mechanical insight is largely due to experimental limitations. However, in recent years experiments focusing on the role of PTMs in DNA accessibility have provided some insight. Cross-linking experiments by Mutskov et al. have shown the nucleosome stability is decreased by hyperacetylation of the H4 tails, while binding of protein GAL4 to its binding site in the wrapped DNA remained unaffected[215]. Work from the Widom group has demonstrated that completely removing all histone tails increased accessibility of nucleosomal DNA for restriction enzymes and in a lesser degree for protein GAL4[216]. More recent sm-FRET experiments have shown that acetylating H3K56 (H3K56Ac) increased nucleosome breathing 7-fold but did not decrease nucleosomal stability[217].

Here we aim to combine several single-molecule methods to answer (1) how does a PTM affect nucleosomal stability and dynamics, (2) how does a PTM affect the binding affinity of a protein, and (3) can we quantify from FRET experiments if and how nucleosomal dynamics is affected by this binding. Because we want as little disruption of the nucleosome structure as possible, we have chosen the trimethylation of lysine 36 in histone 3 (H3K36me3) as modification. Like acetylation, methylation of histones occurs on NH⁺ groups of lysine residues and is mediated by histone methyltransferases. Unlike acetylation, lysines can bind up to three methyl groups, and methylation preserves the positive amine charge of the lysine,

creating only a sterical bulk. Hence methylation of lysine residues should not interfere with the electrostatic histone–DNA interactions[218].

Next to having an active role in DNA repair and transcription events, H3K36me3 has also been found in pericentromeric (constitutive) heterochromatin, which are areas not associated with activity. This hints at H3K36me3 being involved in the structure of heterochromatin[74]. For DNA repair and transcriptional processes H3K36me3 recruits proteins such as p75, better known as LEDGF (Lens Epithelial-Derived Growth Factor)[203][219]. LEDGF/p75 is a chromatin-binding protein that has been tied to integration of HIV-1 cDNA into human chromosomes and reduction of cellular stress-induced apoptosis[220]. The structural basis for LEDGF binding to chromatin through the proteins' PWWP domain has been elucidated and the domain seems to be essential for binding[221]. However, the AT-hook domains of LEDGF have been shown to interact specifically as well as non-specifically with DNA[222]; deletion of the domains resulted in contradicting observations regarding affinity for compacted DNA[223][224]. Despite these observations, a lot is still not known about the exact binding mechanism and effects of LEDGF interactions with chromatin.

In this chapter we detail the effects of LEDGF binding to nucleosomes by combining single-molecule spectroscopy methods with FRET. We observe that LEDGF affinity for chromatin depends mostly on the presence of H3K36me3.

5.2 Materials and methods

5.2.1 Sample preparation and nucleosome reconstitution

A 197 bp long DNA construct containing one Widom 601 sequence and a Cy3B-ATTO647N fluorophore pair was produced with PCR. The fluorophores were positioned 80 base pairs apart, making FRET possible only when the DNA was reconstituted into a nucleosome. DNA containing one Widom 601 sequence and only the Atto647N fluorophore was also produced with PCR. All nucleosomes were reconstituted by salt gradient dialysis from 2 M to 0 mM NaCl overnight. DNA was mixed with human recombinant histones in a titration of molar ratios ranging from 1:1 to 1:3. Only titrations where no unreconstituted DNA substrates were detected through gel electrophoresis were used for FCS experiments. Nucleosomes

containing H3 trimethylated K36 were reconstituted following the same salt gradient dialysis protocol. Measurement buffers contained 10 mM Tris and 15 mM NaCl, unless stated otherwise. Nucleosome concentrations in FCS measurements were between 3 and 7 nM. Samples of 20 to 40 μ l were placed in a closed flowcell to minimize evaporation.

5.2.2 LEDGF purification and labeling

LEDGF/p75 wild-type and Δ AThook were purified as described by Bartholomeeusen [225]. Expression of LEDGF/p75 forms was induced in E.Coli cells (grown in LB medium) by 0.5% IPTG (Isopropyl β -D-1-thiogalactopyranoside) followed by incubation at 30C for 4 hours. Cells were collected and lysed in 20 mL lysis buffer (50 mM Tris, 100 mM NaCl, 1 mM DTT, 10 μ g/ml proteinase K and 1 U/10 ml DNase, pH 7.4). After lysis cells were centrifuged and the supernatant was purified over a Heparin column and eluted with a 50 mM Tris 2M NaCl, 1 mM DTT buffer (pH 7.4). Flag-tagged LEDGF/p75(C373A) was labeled by incubating 50 μ M of the protein with a 10-fold excess of ATTO532-maleimide for 3 hours at room temperature. Unbound dye was removed using Amicon ultra-0.5 centrifugal filters (10 kDa MWCO). The degree of labeling was calculated as

$$dol = \frac{A_{532} \cdot \epsilon_{LEDGF}}{(A_{280} - CF_{280} \cdot A_{532}) \cdot \epsilon_{Atto532}}$$

with $\epsilon_{LEDGF} = 16960M^{-1}cm^{-1}$, $\epsilon_{ATTO532} = 11500M^{-1}cm^{-1}$ and $CF_{280} = 0.11$ which corrects for absorbance of ATTO532 at 280nm. Labelling efficiencies were 84% for LEDGF_{WT} and 89% for LEDGF Δ ATh.

5.2.3 Single-molecule fluorescence microscopy

PIE-F(C)CS measurements were done for a least 60 minutes, in recordings of 10 minutes. Measurements were performed on a home-built confocal microscope with a water-immersion objective (60x, NA 1.2, Olympus), using an ICHROME MLE-SFG laser module as excitation source. The excitation beam was directed via fiber coupler and a dichroic mirror (z514/640rpc, Chroma) through the objective and focused 50 μ m above the glass-sample interface. FCS experiments were performed in pulsed interleaved excitation (PIE) mode by alternating 514 (30 μ W) and 632 nm (20 μ W) excitation

pulses of 100 ns long with 300 ns intermittent dark periods. Collected fluorescence was spatially filtered with a 50 μm pinhole in the image plane and split by a second dichroic mirror (640dcsr, Chroma). The fluorescent signals were further filtered (hq570/100nm and hq700/75nm, resp.) and focused on the active area of single photon avalanche photodiodes (SPADs, SPCM AQR-14, Perkin Elmer). The photodiodes were read out with a TimeHarp 200 photon counting board (Picoquant), and the arrival times of the collected photons were stored in t3r (time-tagged to time-resolved) files. These files were further processed with home-built Python analysis programs.

5.2.4 Fluorescence Correlation Spectroscopy

Fluorescently labeled molecules diffusing through the confocal focus cause the intensity of the fluorescent signal to fluctuate in time. In Fluorescence Correlation Spectroscopy (FCS) these fluctuations are used to determine the concentration, diffusion constant and when possible dynamical properties of molecules. The fluctuations in intensity are analyzed by correlating photon arrival times over increasing time-lag τ :

$$G(\tau) = \frac{\langle \delta I_1(t) \cdot \delta I_2(t + \tau) \rangle}{\langle I_1(t) \rangle \cdot \langle I_2(t) \rangle} \quad (5.1)$$

To assess the diffusion of a molecule, photon arrival times of one channel are correlated to generate an autocorrelation curve ($I_1 = I_2$). To quantify the fraction of two differently labeled molecules diffusing through the focus at the same time (i.e. as a complex) the signal of one molecule (I_1) is correlated with the signal of another molecule (I_2) to generate a crosscorrelation curve. The correlation function that fits the diffusional part of a autocorrelation curve is formulated in terms of the concentration and diffusion time of the population of molecules labeled with the same fluorophore, taking into account the confocal volume which they diffuse through:

$$G_{diff}(\tau) = N^{-1} \cdot (1 + \tau/\tau_D)^{-1} \cdot (1 + a^{-2} \cdot \tau/\tau_D)^{-1/2} \quad (5.2)$$

where τ_D is the diffusion time and N the average number of molecules in the confocal volume. Parameter a is the ratio between the axial and radial size of the confocal volume. The value of a for the setup used for the measurements presented here was determined through calibration experiments to be 8.

Physical interpretation of the crosscorrelation functions requires additional calculations and will be discussed further on. The Python `pycorrelate` module developed by Ingargiola et al.[133] was used to calculate all correlation curves. The correlation algorithm used in this module was developed by Laurence et al.[134]. The algorithm is based on rewriting the correlation as a counting operation on photon pairs and can be used with arbitrary bin widths and spacing.

The diffusion time τ_D of a molecule is determined by its size and the viscosity of the solvent η . The hydrodynamic radius of a molecule r_H can be obtained using the Stokes-Einstein equation:

$$r_H = \frac{k_B T}{6\pi\eta D} \quad (5.3)$$

where diffusion constant $D = \frac{w^2}{4\tau_D}$ with k_B the Boltzmann constant, T temperature and w the radius of the confocal spot in the radial (x,y) direction. Equation 5.3 shows the hydrodynamic radius scales proportional with diffusion time, implying that larger molecules move slower through the focus. This property was used to analyze correlation curves constructed from signals of molecules of different sizes. If we assume the molecule to have a spherical shape, the radius scales with the molecular mass as $r_H \propto M^{\frac{1}{3}}$. In practice this means for the diffusion time to increase two-fold, the mass of a molecule needs to increase a factor of 8.

Photophysics of the fluorophore, i.e. transiting to a triplet or dark state, as well as afterpulsing effects of the APD's need to be included in the fit of a correlation curve

$$G_{total}(\tau) = G_{diff}(\tau) \cdot G_{tr}(\tau) \cdot G_{ap}(\tau) \quad (5.4)$$

where the latter two terms are defined as

$$G_{tr}(\tau) = 1 + \left(\frac{F_{tr}}{1 - F_{tr}} \cdot e^{\frac{-\tau}{\tau_{tr}}} \right)$$

and

$$G_{ap}(\tau) = 1 + \left(\frac{F_{ap}}{1 - F_{ap}} \cdot e^{\frac{-\tau}{\tau_{ap}}} \right)$$

with F_{tr} , F_{ap} the fractions of molecules associated with either triplet state (**tr**) or afterpulsing (**ap**), and τ_{tr} , τ_{ap} their characteristic timescales. As

fluorophore photophysics and afterpulsing take place on different timescales sensible boundaries were set for fitting these parameters.

5.2.5 Fluorescence Cross-Correlation Spectroscopy and binding affinity

Contrary to the value of $G(0)$ of an autocorrelation curve, the plateau of a crosscorrelation curve at small τ does not directly correspond to the concentration of molecules in complex. Rather, $G(0)_{cc}$ represents the complex molecules as a percentage of the population of molecules present at a higher percentage[139]. To calculate the real number of complexed molecules from the crosscorrelation curve, N_{CC} is first corrected for background photons from both channels involved in the cross-correlation:

$$N_{CC,corr} = \frac{N_{CC} \cdot (I_{514G} - bg_{514G}) \cdot (I_{632R} - bg_{632R})}{I_{514G} \cdot I_{632R}} \quad (5.5)$$

Here channel I_{514G} corresponds to the signal of ATTO532-labeled proteins and I_{632R} with ATTO647N-labeled DNA or nucleosomes. We need to take into account that confocal spots from different excitation wavelengths do not completely overlap. Not compensating for this incomplete overlap would mean underestimating the number of molecules in complex. The actual number of molecules in a complex is then calculated as

$$N_{514G \times 632R} = c_{over}^{-1} \cdot \frac{N_{514G} \cdot N_{632R}}{N_{CC,corr}} \quad (5.6)$$

where c_{over} is used to correct for the incomplete overlap. Calibration experiments after each alignment of the setup showed $c_{over} = 0.9 \pm 0.03$, implying without correction $\sim 10\%$ of the number of molecules in complex would be missed. With the actual number of molecules in complex determined, the dissociation constant K_d is calculated as

$$K_d = \frac{[molecule1] \cdot [molecule2]}{[complex1 + 2]} \quad (5.7)$$

The dissociation constant is a measure of the binding affinity and is equal to the concentration of molecule 1 at which half of its available binding sites are occupied by molecule 2.

5.2.6 Multi-component fit and nucleosome dynamics

To determine stoichiometry of populations of two interacting molecules, the number of molecules N in equation 5.2 is split in fractions (for instance closed and open, or bound and free) as represented in the diffusional part of $G(\tau)$:

$$G(\tau)_{diff} = N_{total}^{-1} \cdot (F_1 \cdot (1 + \tau/\tau_{D1}) \cdot (1 + a^{-2} \cdot \tau/\tau_{D1}))^{-1/2} \cdot (F_2 \cdot (1 + \tau/\tau_{D2}) \cdot (1 + a^{-2} \cdot \tau/\tau_{D2}))^{-1/2} \quad (5.8)$$

with fractions $F_1 + F_2 = 1$.

For nucleosomes the closed and open fractions are known by previously fitting the autocorrelation curve from the FRET channel ($F_{closed} = \frac{N_{closed}}{N_{total}}$). From this initial fit the characteristic diffusion time ($\tau_{D,closed}$) is also known, leaving only the diffusion time of open nucleosomes $\tau_{D,open}$ to be fitted by the multi-population fit algorithm.

To quantify the effect of protein binding to nucleosomal dynamics, equation 5.8 is extended to include a third population following the same fractioning principle. This means two new variables, F_3 and τ_3 , need to be fitted. PIE-FCS experiments on double-labeled nucleosomes with unlabeled protein however only result in two usable (auto)correlation curves: 514R514R and 632R632R. The first curve represents closed nucleosomes, the second all nucleosomes, open and closed, as well as free and bound to protein. To fit the 632R autocorrelation curve we assumed that (1) only open nucleosomes bind to proteins, (2) the dissociation constant (K_d) between open and closed nucleosomes was not altered, and (3) the diffusion times τ_D of unbound (free) open and closed nucleosomes remained the same. Also, if FRET efficiency per closed nucleosome was the same as in a measurement on nucleosomes only, it is not necessary to include a fourth population in the fitting algorithm (closed nucleosomes bound to protein). If the FRET efficiency is however lower, then the 514R autocorrelation curve needs to be fitted with two populations, with $\tau_{D-closednucl-free}$ as a fixed parameter. We can also set the lower bound of $\tau_{D-closednucl-bound}$ to $\tau_{D-closednucl-free}$ as we assume a closed nucleosome bound to a protein is at least diffusing as fast as an unbound one, if not slower due to increased size. The 632R curve is then fitted including this additional population.

5.3 Results

5.3.1 Effect of H3K36me3 on the stability of nucleosomes

To measure the effect of the H3K36me3 modification on a mononucleosomes' intrinsic and salt-dependent equilibria, nucleosomes 39-12-H3(K36me3) and 39-12-WT were diluted to nanomolar concentration in 10 mM Tris and NaCl titrated up to 50 mM. The fluorescent signals of the labels were acquired in PIE-FCS measurements to quantify the concentration and diffusion of the nucleosome and the rates of nucleosome opening and closing.

The average FRET value $\langle E \rangle$ derived from the total fluorescent signals (corrected for background photons) showed for nucleosome 39-12-H3 a significantly lower value compared to 39-12-WT for all salt concentrations. At 1 mM NaCl the difference was almost 50%; 0.25 ± 0.005 compared to 0.42 ± 0.01 for 39-12-WT. Fitting with the Hill function resulted in transition concentration $c_{1/2}$ of 15.83 ± 0.51 mM NaCl and Hill coefficient $H = 0.08 \pm 0.006$. For 39-12-WT $c_{1/2} = 21 \pm 1$ mM and $H = 0.14 \pm 0.03$, indicating stronger interactions between the nucleosomal DNA exit and the histone core. At low salt concentrations 39-12-H3 was found more often in an open state; 52% at 1 mM NaCl (39-12-WT: 44%).

Fitting the inverted equilibrium constant from population fractions resulted in a salt-independent equilibrium K_{eq} of 1.16 ± 0.393 , a transition concentration x_0 of 12.97 ± 0.2 mM and salt stoichiometry m of 2.04 ± 0.23 ion pairs. Compared to 39-12-WT ($K_{eq} = 0.83 \pm 0.07$, $c_0 = 22.1 \pm 0.04$ and $m = 3.6 \pm 0.1$) nucleosomes containing H3K36me3 have a 25% lower intrinsic equilibrium constant, an almost 50% lower transition concentration and about 1.5 less electrostatic interactions between DNA and histone core. Evaluating nucleosomal dynamics over the salt titration range revealed below the transition concentration c_0 39-12-H3 opened on average at a rate of 24 ± 15 s^{-1} and closed 23 ± 15 times per second, translating to an equilibrium constant of appr. 1. Above c_0 the opening rate rapidly increased to 3000 s^{-1} with the closed rate decreasing to 10 times per second, on average. For comparison, below their c_0 39-12-WT nucleosomes on average opened 15 and closed 32 times per second, and above c_0 still closed 40 s^{-1} while opening 1200 times per second at 50 mM NaCl.

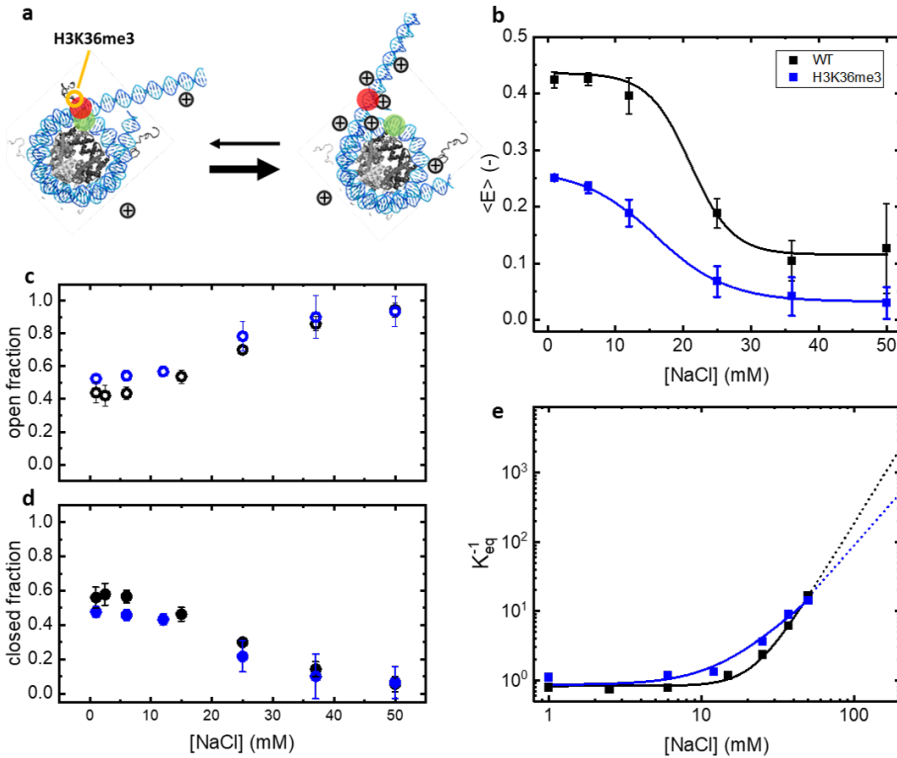


FIGURE 5.1: Post-translational modification H3K36me3 drives nucleosomes to open conformation. **a)** Salt ions interact with the nucleosome, cancelling electrostatic interactions between DNA and histone core, thereby driving the nucleosome to the open conformation. **b)** Comparing average FRET $\langle E \rangle$ from 39-12-H3 with an unmodified nucleosome shows lower $\langle E \rangle$ at both low and high salt concentrations. **c) and d)** Open and closed fractions showed nucleosomes containing H3K36me3 are also at low salt concentrations more in the open conformation. **e)** Fitting the inverse of the equilibrium constant from conformational states resulted in a K_X of 0.004 ± 0.004 , a K_0 of 0.9 ± 0.4 , c_0 of 13.0 ± 0.2 mM and $m = 2.0 \pm 0.2$. All these values are significantly lower compared to those found for 39-12 nucleosomes containing WT histones.

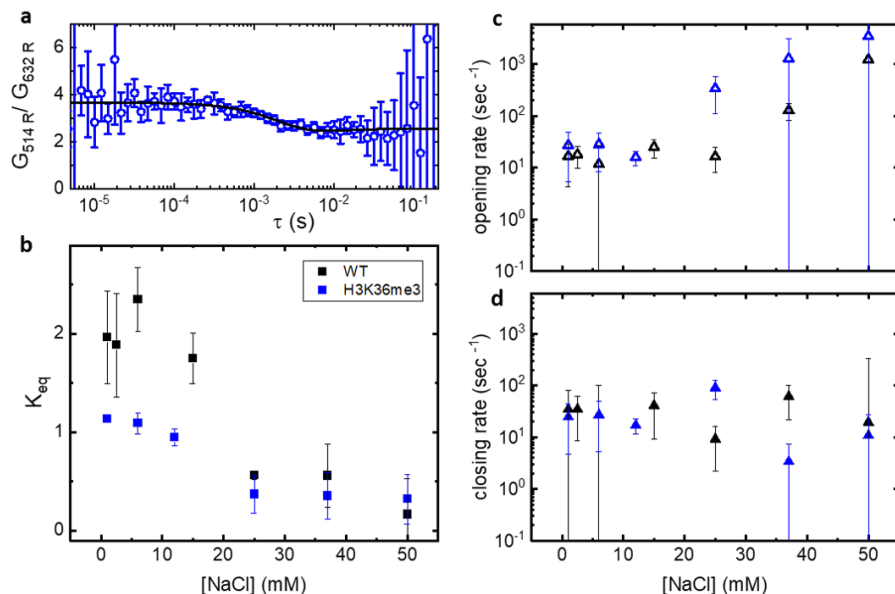


FIGURE 5.2: **Post-translational modification H3K36me3 increases opening rate, but not closing rate of nucleosome.** **a)** Characteristic plot of dynamics correlation curve of 39-12-H3K36me3. **b)** The equilibrium constant derived from opening **(c)** and closing rates **(d)** confirmed result from open and closed fractions that nucleosome 39-12-H3 is more often in an open conformation for all salt concentrations. Under c_0 the average opening rate of 39-12-H3 is 24 s^{-1} (15 s^{-1} for 39-12-WT) and average closing rate is 23 s^{-1} (32 s^{-1} for 39-12-WT).

5.3.2 LEDGF binding to DNA and nucleosomes, and resulting ATTO532 quenching

PIE-FCCS measurements were performed on single-labeled LEDGF with ATTO532 and nucleosomes reconstituted from 601 DNA sequence labeled with ATTO647N on one nucleosomal exit (**figure 5.4a**). FRET between ATTO532 and ATTO647N is possible when the labels get close enough ($r_F = 5.1\text{nm}$), which was in principle possible in our construct. However, we did not observe any evidence of this. Nevertheless, a decrease of the fluorescent signal of LEDGF-ATTO532 was clearly visible over time. Depending on concentration the signal stabilized after around 20 minutes. This phenomenon did not seem to be caused by bleaching, as ATTO532

dye was measured at same intensities and showed no decrease. Also non-specific sticking to surface was ruled out as the decrease also occurred for LEDGF-ATTO532 on glasses coated with either PLL-PEG or BSA (shown in **fig. 5.3a**). Fitting showed that both concentration and diffusion time seemed unaffected, meaning protein concentration was not decreasing, but the ATTO532 molecules were being quenched. This process is described in literature as well[226][227][228]. Hence we concluded concentrations and diffusion times derived from ATTO532 signal were reliable to use for affinity calculations.

The loss of fluorescent signal from LEDGF-ATTO532 needed to be taken into consideration when examining the crosscorrelation curve to detect complex formation between protein and nucleosome. As this correlation curve was constructed from correlating photons from their respective fluorescent channels, the complex concentration, as well as its diffusion time, might be underestimated due to signal decrease over longer timescales from the green channel. We observed a small decline of complex concentration in interaction experiments (**fig. 5.2e**). In the case shown however, this is most likely due to decline in red signal /molecules, most likely caused by sample holder drift, a microscope artefact. Since both nucleosome and complex concentrations decrease at similar rates this however did not influence the dissociation constant K_D . Omitting the first 5 minutes, we observed that diffusion times during the next 25 minutes of the measurement were also stable, at 2.2 ms for nucleosomes (39-12-WT), 1.8 ms for LEDGF-WT and 3 ms for the complex. The significantly slower diffusion time of LEDGF in complex in this measurement compared to that of free LEDGF at 1 ms (**fig. 5.2c**) could be used as a separate method to calculate complex formation by fitting the autocorrelation curve from LEDGF with 2 populations. However, 30 minutes into the measurement the diffusion time of LEDGF appeared to decrease to an average of 1.64 ms, and the diffusion time of the complex decreased to a similar time as that of nucleosomes. Similar observations were made during measurements of the other combinations of nucleosomes and LEDGF variants. While diffusion times of nucleosomes and proteins were comparable to those of 39-12-WT and LEDGF-WT as in **fig. 5.3f**, the diffusion times of the complexes were shorter: 1.8 ± 0.7 ms for 39-12-WT with LEDGF- Δ Ath, and 2.0 ± 0.5 ms for LEDGF-WT and 1.8 ± 0.4 ms for LEDGF- Δ Ath with nucleosomes containing H3K36me3. The errors increased not only from the decreased diffusion time but also because of

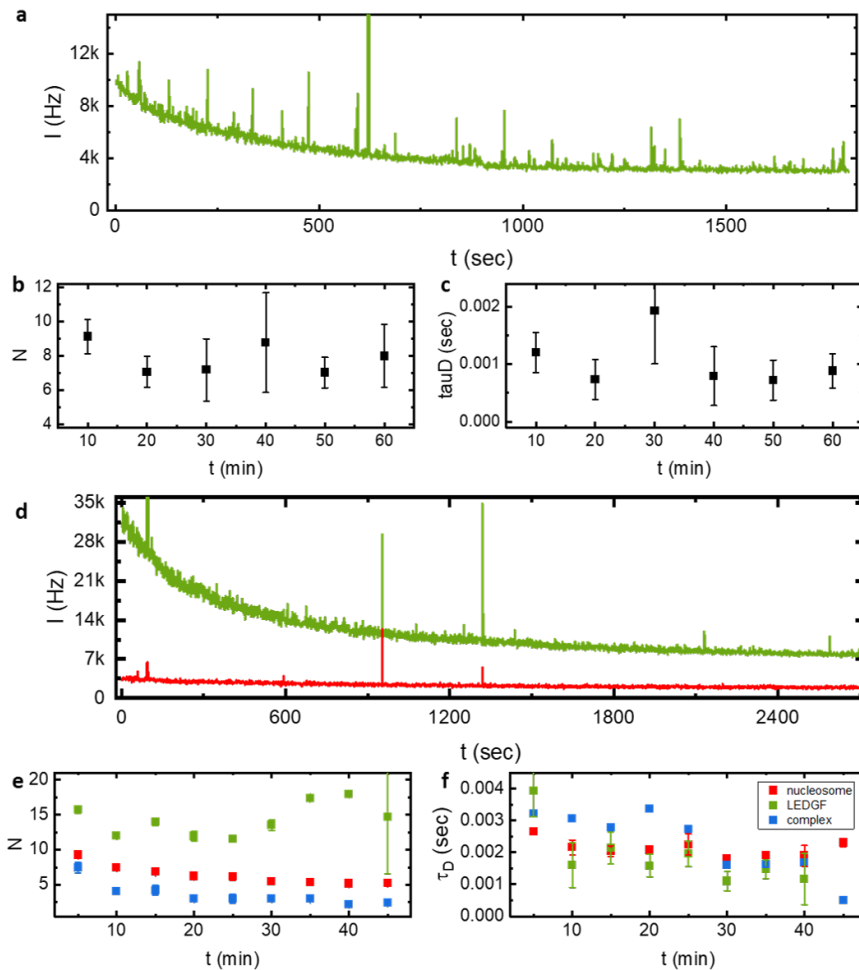


FIGURE 5.3: **ATTO532 is prone to quenching when LEDGF is over-saturated with labelling dye.** **a)** Decrease of the fluorescent signal from ATTO532 labelled LEDGF shows an irreversible loss of fluorescence on glasses coated with PLL-PEG or BSA. **b)** However, bleaching and sticking can be ruled out, because the concentration of protein remained stable over time, as did the diffusion time (**c**). **d)** Fluorescent signal of an interaction experiment of single-labeled nucleosomes (red) with LEDGF (green) decreased somewhat in signal from the nucleosome, likely due to sample holder drift. **e)** The number of nucleosomes decreased according to the decrease in fluorescence signal although the LEDGF concentration was remained constant. **f)** The diffusion times of both nucleosomes and LEDGF remained stable over time, the diffusion of the complex however seemed to decrease. (Measurement shown in **d-e-f** is on nucleosome 39-12-WT with LEDGF-WT)

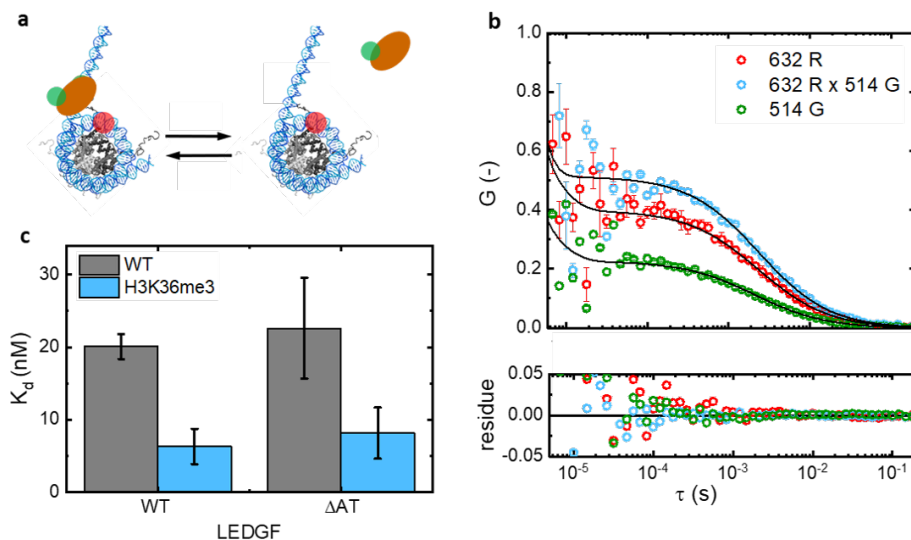


FIGURE 5.4: H3K36me3 tripled LEDGF affinity for nucleosomes, deletion of Athook domain does not decrease affinity. **a)** Representation of LEDGF labeled with ATTO532 binding to nucleosome labeled with ATTO647N. This method cannot distinguish if LEDGF binds to closed or open nucleosomes, or to both conformations. **b)** Representative auto- and cross-correlation curves from measurements, corrected for concentrations of molecules associated with each curves (red: nucleosomes, green: LEDGF, blue: complex) **c)** Dissociation constants derived from concentrations showed both WT-LEDGF and Δ AThook LEDGF had a significantly higher affinity for nucleosomes containing H3K36me3.

protein aggregates. Dissociation constants (**fig. 5.4c**) were calculated from averaging affinity at the start and at the end of the measurement. Note though that at the end fluorescent signals were stable, but complex concentration might be underestimated due to quenching. At the start however, complex concentration might be overestimated due to the rapid decrease of the fluorescent signal. Averaging these two instances may cancel out these uncertainties. The results showed both LEDGF-WT and LEDGF- Δ AThook had a higher affinity for nucleosomes containing H3K36me3 (6 ± 2 nM and 8 ± 4 nM, resp.) than for nucleosomes containing recombinant/WT histones (LEDGF-WT: 20 ± 2 nM, LEDGF- Δ AThook: 23 ± 7 nM). The error bars in **fig. 5.4c** are the propagated standard deviations after averaging. The size of the errors result from larger differences between affinities calculated at the

start and at the end of the experiments for LEDGF- Δ ATh than for LEDGF-WT.

5.3.3 Effect of LEDGF binding on nucleosome dynamics

PIE-FCS was used to measure the changes in nucleosome conformation stoichiometry, FRET efficiency and diffusion time upon adding WT or Δ ATh LEDGF to nucleosomes containing or lacking H3K36me3 (39-12-H3 and 39-12-WT). Proteins were added to nucleosomes in a 4 to 1 ratio.

A decrease in FRET signal was immediately noticeable in the first 5-10 minutes (fast binding), then slowed down (**fig. 5.5a**). The rapid decrease at the start of the measurement was however only visible for nucleosome 39-12-H3 with LEDGF- Δ ATh and to a lesser degree for nucleosome 39-12-WT with LEDGF-WT. In other measurements it was probably missed because a larger time was used for transferring sample to microscope and starting the measurements, in which time nucleosomes may have been depleted by sticking to the surface of the flowcell. We therefore corrected the FRET intensity by dividing it by the number of closed nucleosomes, determined from fitting the correlation curves. When adding LEDGF, FRET per nucleosome decreased, but only significantly for LEDGF- Δ ATh binding to 39-12-WT and 39-12-H3 (**fig. 5.5b**). The fraction of closed nucleosomes decreased over time as well (**fig. 5.5c**), so loss of FRET signal was mostly from losing closed nucleosomes, and only marginally from nucleosomes becoming more open through binding of LEDGF. The equilibrium constants decreased accordingly (**fig. 5.5d**). Interesting to note is that LEDGF binding lowers the equilibrium constant K_{eq} between open and closed nucleosomes faster and more for 39-12-WT nucleosomes than for 39-12-H3 nucleosomes. This could however be caused by differences in protein concentration, since it was not possible to verify directly from measurements.

Fig. 5.6a shows the reaction scheme for combined nucleosome breathing and LEDGF binding. The loss of overall FRET, but minimal loss of FRET per nucleosome implied route k_{14} , i.e. from free closed nucleosome to bound open nucleosome via bound closed nucleosome, was not the preferred pathway. Also, in all measurements the diffusion times of closed nucleosomes (with LEDGF and complexes present) were not significantly slower than those found for free closed nucleosomes, indicating no detectable binding of proteins to closed nucleosomes. Lastly, the decrease in FRET signal as well as the decrease in closed nucleosomes did not seem to reverse, implying pathway k_{32} is likely never taken. Fitting in a complex fraction in addition

to an open and a closed fraction on autocorrelation curve 632R (fig. 5.6b) resulted in diffusion times of the complex similar to the times found in single-labeled experiments for binding to 39-12-WT nucleosomes (fig. 5.6c); 3.6 ± 0.3 ms (LEDGF-WT) and 2.2 ± 0.4 ms (LEDGF- Δ ATh). For nucleosomes containing H3K36me3 the diffusion times of complexes appeared to be faster (1.1 ± 0.8 ms (LEDGF-WT) and 1.7 ± 1.8 ms (LEDGF- Δ ATh)), comparable to the times of closed nucleosomes. Faster diffusion times might indicate bound 39-12-H3 nucleosomes were more wrapped through LEDGF binding, but the nucleosomal exit was not close enough for FRET to occur.

Combining the found diffusion times for the complex fractions with the decrease in I_{514R} per nucleosome showed an interesting connection; the decrease in FRET was almost proportional with the decrease in diffusion time. The complex with the slowest diffusion time, 39-12-WT with LEDGF-WT, had the smallest decrease of $8\pm 2\%$. Complex 39-12-WT with LEDGF- Δ ATh decreased $22\pm 9\%$. Complexes with 39-12-H3 showed FRET decreasing with $14\pm 2\%$ (LEDGF-WT) and $26\pm 7\%$ (LEDGF- Δ ATh). This might mean that, depending on the LEDGF variant and the presence of H3K36me3, a small subset of proteins were able to bind to closed nucleosomes (taking pathway k_{14}). The 3-component fit resulted in similar complex fractions for nucleosome 39-12-WT with both LEDGF variants; 0.33 ± 0.02 with open: 0.38 ± 0.02 and closed: 0.29 ± 0.02 (LEDGF-WT) and 0.26 ± 0.02 with open: 0.42 ± 0.02 and closed: 0.32 ± 0.02 (LEDGF- Δ ATh). For nucleosome 39-12-H3 the fit resulted in a larger complex fraction of 0.48 ± 0.04 (with open: 0.11 ± 0.04 and closed: 0.41 ± 0.04) for binding with LEDGF-WT and a small fraction of non-bound nucleosomes 0.14 ± 0.05 (with open: 0.46 ± 0.05 and closed: 0.40 ± 0.05) for LEDGF- Δ ATh.

Considering that diffusion times yielded large errors and resembled the times of closed nucleosomes, the fitting algorithm may not have been able to distinguish between the contributions of the complex fraction to the autocorrelation curve from those of closed unbound nucleosomes. An obvious solution would have been to fit the 632R autocorrelation curve with 4 populations. This would have resulted in a objectively better fit of the curve, but would unlikely had given better results for the stoichiometry of the population.

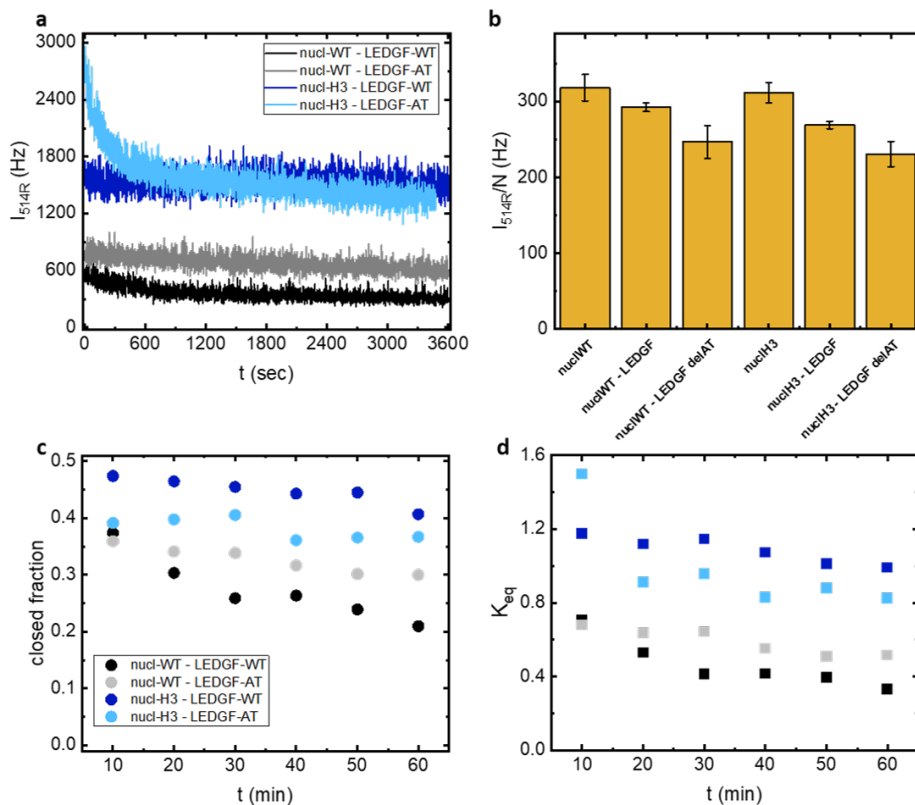


FIGURE 5.5: Unlabeled LEDGF variants binding to double-labeled nucleosomes became visible from loss of FRET signal. a) Upon adding unlabeled LEDGF, for all combinations of proteins and nucleosomes a decrease in total FRET signal was visible **b)** Also FRET per nucleosome decreased for each combination between nucleosomes and proteins, however the loss was less since also the numbers of closed nucleosome **(c)** and consequently the equilibrium constants **(d)** decreased. Error bars were omitted from figures **(c)** and **(d)** for clarity. For nucleosome 39-12-WT (318 ± 17 ph/s), the loss of FRET was $8 \pm 2\%$ with LEDGF-WT and $22 \pm 9\%$ with LEDGF- Δ ATh. For nucleosome 39-12-H3 (312 ± 14 ph/s) the loss was $14 \pm 2\%$ with LEDGF-WT and $26 \pm 7\%$ with LEDGF- Δ ATh.

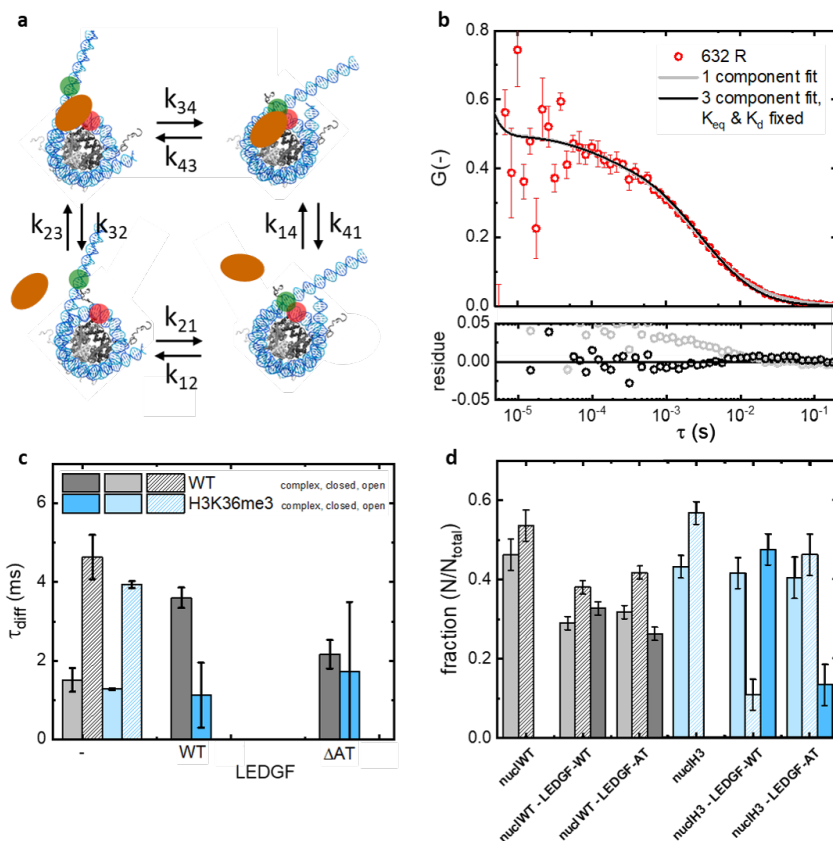


FIGURE 5.6: Binding of LEDGF variants to nucleosomes containing H3K36me3 decreased diffusion times of the formed complex. **a)** 4-state reaction scheme of protein binding to open and closed nucleosomes. **b)** Fitting the autocorrelation with 3 components (open, closed and nucleosomes in complex) improved the fits, especially around the millisecond timescale, characteristic for nucleosome and LEDGF (and their complex) diffusion times. **c)** Complex diffusion times from 3-component fit resulted in times for nucleosome 39-12-WT with either LEDGF variant resembling times found in measurements on single-labeled nucleosomes and proteins (**fig. 5.3f**). **d)** Fractions from fit resulted in significant complex fractions for 39-12-WT with LEDGF-WT (0.33 ± 0.02) and LEDGF- Δ ATh (0.26 ± 0.02), and 39-12-H3 with LEDGF-WT (0.48 ± 0.04). For 39-12-H3 with LEDGF- Δ ATh only a small fraction of complex was observed (0.14 ± 0.05).

5.4 Discussion and conclusions

Here we studied the effect of H3K36me3 on nucleosomal dynamics and stability, and how it increased affinity of the protein LEDGF to nucleosomes. Nucleosomes containing H3K36 trimethylation seemed more open from average FRET and equilibrium constants. But the FRET signal shows that the trimethylation does not inhibit bending of the nucleosomal exit towards the histone core. It does however lower the number of electrostatic interactions m from 3.6 to 2. This decrease in DNA-histone interactions is supported by the observation of faster dynamics of H3K36me3 nucleosomes in both low and high salt conditions. Increased kinetics through less (strong) interactions between DNA arms and histone core may be how the trimethylation facilitates binding to nucleosomal DNA in processes such as transcription and DNA repair. Morrison et al.[229] have recently suggested that the H3 histone tails interact with compacted DNA as a ‘fuzzy’ complex, interacting robustly but adopting a dynamic ensemble of DNA-bound states[230]. It is possible that trimethylation of lysine 36, although not altering the local charge of the histone tail, does change the range of binding states with the condensed DNA.

We have also presented evidence that H3K36me3 increases LEDGF affinity to nucleosomes by using PIE-FCCS on single-labeled nucleosomes and single-labeled variants of the LEDGF protein (wild type, WT and AT-hook deficient, Δ ATh). PIE-FCCS and our data analysis algorithm could circumvent the effects of ATTO532 quenching and generate reliable results for concentrations and diffusion times of nucleosomes, proteins as well as the complex formed between them. The diffusion times we found for the four different complexes differed between one another with more than one millisecond, indicating different modes of interaction, depending on the LEDGF variant and if H3K36me3 was present or not in the nucleosome. Complexes of AT-hook deficient LEDGF with nucleosomes diffused fastest at around 1.8 ms, almost as fast as closed nucleosomes (1.2-1.5 ms). It might be through interaction of the PWWP domain, and the lack of the 20+ amino acids of the AT-hooks domain, that the LEDGF variant brings the DNA exit closer to the nucleosome core. The slowest complex, composed of LEDGF-WT and nucleosomes lacking H3K36me3, still diffused faster than open nucleosomes (3 ms vs. 4 ms). The complex of LEDGF-WT with H3K36me3 nucleosomes is somewhat faster, around 2 ms.

We found similar diffusion times when investigating the effect of LEDGF

variants on nucleosome dynamics in PIE-FCS measurements on double-labeled nucleosomes and unlabeled proteins. As the LEDGF variants were unlabeled we had to determine the bound fractions by fitting the autocorrelation curve from the signal of all states of nucleosomes. The results for fractions and diffusion times for experiments on WT nucleosomes seemed to be more accurate than those of experiments on H3K36me3 nucleosomes; both fraction sizes and diffusion times had large errors. Since these values are based on the correlation curve, representing the nucleosome in certain conformational states, these large errors might be caused by 'fuzzy' states due to the altered interactions of the H3 tail with nucleosomal DNA. We also observed that despite losing closed nucleosomes at the start of an experiment, loss of FRET per nucleosome is minimal, about 10-25% depending on the protein and nucleosome variants, implying the pathway from free nucleosome to bound nucleosome is predominantly via free open nucleosomes. The steady decrease in FRET signal in measurements of 60 minutes pointed to the depletion being irreversible. This observation, combined with the diffusion times of the complex that were faster than those of open nucleosomes, suggests that LEDGF binding stabilizes open nucleosomes by remodelling rather than unwrapping them. It would be an interesting follow-up experiment to titrate salt to determine if the electrostatic interactions in LEDGF-bound nucleosomes, and thus nucleosomal stability, have increased through binding.

QUANTIFYING TRANSCRIPTION FACTOR AFFINITY IN CHROMATIN

Transcription factors (TFs) are proteins that bind to specific binding sites or recognition sequences in the promotor region of genes and are essential in the transcription regulation. Binding sites are often located at the DNA exits of the nucleosome; unwrapping nucleosomes from their ends, facilitates access of transcription factors to the nucleosomal DNA. To gain a mechanistic insight into the function of TFs and its interaction with chromatin, it is relevant to study its interactions with techniques capable of resolving the appropriate time scales under physiologically relevant conditions.

We combined Fluorescence Cross-Correlation Spectroscopy (FCCS) with Pulsed Interleaved Excitation (PIE) to quantify the binding affinity of the Glucocorticoid Receptor (GR) in the ex vivo environment of a nuclear extract to mimic in vivo molecular crowding as well as competition and cooperativity from other proteins and pioneering factors. We have shown previously that a Glucocorticoid Response Element (GRE) embedded in the Widom 601 nucleosome increased the opening and closing rates. We performed our measurements in nuclear extract to relate breathing dynamics to binding affinity in a single experiment; we observed that in the nuclear extract environment, the affinity of GR was most affected by DNA compaction, concurring with previous research in vitro, and less by the position of the GRE in the nucleosomes. In addition, we used FCS to quantify the specificity of the c-Jun protein, another transcription factor, for DNA containing or lacking its recognition sequence and found that the protein is capable of condensing both DNA constructs regardless of a recognition site present. The ex vivo experiments on GR bridge the observations made in vivo and in vitro by showing how a proteins' binding affinity and specificity are related to binding sites in compacted DNA in the presence of an abundance of unknown proteins, while keeping track of the relevant constituents in the environment.

This chapter is in collaboration with:

M. van Eikenhorst, S. Grevink, D. Zandstra, M. Schaaf, Leiden University.

6.1 Introduction

Transcription factors (TFs) are proteins that bind to specific binding sites or recognition sequences in the promotor region of genes[231]. These proteins play a pivotal role in the transcription regulation. *In vivo*, transcription factors interact with not only with DNA but also with a host of other proteins that organize DNA[232][233]. Protein interactions with DNA condensed into chromatin have been shown to occur with association and dissociation times on a wide timescale (microseconds to minutes)[234][95][50] and with an affinity that is influenced by DNA sequence[233].

Transcription factor binding to DNA is expressed in affinity as well as specificity (or the inverse: promiscuity)[235][236]. Binding (or absolute) affinity is the ratio between the concentrations of free protein, DNA containing binding site, and their complex in molar dimensions (K_d [M]) whereas specificity involves both binding to a specific partner and not binding to other proteins or binding sites ($K_d^{absolute}/K_d^{general}$), and is often used to qualitatively describe protein interactions [237][236]. Specificity has also been described as local affinity, depending on possible interactions between a protein and binding site in close proximity of the target site, i.e. on the concentrations of all proteins and binding sites present locally[238]. Local differences in concentrations occur *in vivo* through several mechanisms (compartmentalization, phase separation), as opposed to *in vitro*, where concentrations of the constituents are expected to be homogeneous. Also, *in vitro* all constituents (proteins, binding sites, buffer composition) are known, making it in principle possible to calculate the affinities of all interactions. Because of these different environments, different measuring techniques and environments are often used, making an absolute parameter such as affinity, difficult to compare[239].

A transcription factor for which a wide range of affinities was found is c-Jun[240]. As either a homodimer, or a heterodimer with a closely related protein[241], it forms AP-1 (activation factor 1) [242], which is involved in transcription initiation [243][244]. Depending on being a monomer or a dimer, reported affinities of c-Jun for its specific DNA binding sequence (TRE: TPA responsive element) ranged from 10-12 nM (c-Jun/c-Fos, methylated and unmethylated DNA) [245] [246] to between 30 nM and 100 nM (c-Jun dimer, recombinant) [247][248][249] *in vitro*. Binding to non-specific sequences resulted in affinities as low as 2147 nM [246]. It was also observed that without the presence of closely related protein c-Fos, affinity

for DNA decreased [250][251] and c-Jun dissociated within seconds from DNA[252]. *In vivo*, similar trends were observed in ChIP-Seq experiments; however, as c-Jun associates with a multitude of proteins[253][254][255], these results are often difficult to interpret[256][257].

The Glucocorticoid Receptor (GR) is in many ways similar to c-Jun; after activation by a steroid hormone[258], it too can form homo- as well as heterodimers [259][260], which interact either directly with DNA or through tethering with a multitude of other proteins[261][262] and has been ascribed a pioneering role in transcription[263][264]. The binding affinity of GR for DNA depends on the conservation of, as well as the position of the recognition sequence (GRE)[94][95]. Affinity also increased when DNA was compacted in nucleosomes[91][92].

Another thing c-Jun and GR (and many other proteins) unfortunately have in common is the difficulty to relate their behavior *in vitro* to *in vivo*. A variation of dissociation constants of GR for nucleosomal DNA with GRE at different locations in the nucleosome were reported from *in vitro* and *ex vivo* measurements [91][93][95]; however, the experimental methods were based on fixed complexes (ELISA, gel-shift assays, single-color TIRFM) or lacked the complex environment that is found *in vivo* by using recombinant or purified proteins. On the other hand, *in vivo* measurements have characterized interactions ranging from milliseconds up to minutes[85][234][265], but lack the positional accuracy[50][266].

In order to bridge the gap between well-controlled *in vitro* experiments and *in vivo* measurements in bulk, here we combine pulsed interleaved interaction (PIE) with fluorescence cross-correlation spectroscopy (FCCS) for *ex vivo* to characterize the interaction of c-Jun with DNA containing and lacking the TRE sequence, and to quantify the affinity of GR in nuclear extract to the Widom 601 sequence. In this DNA sequence, the GRE was embedded at different positions so that, when the DNA constructs were condensed into nucleosomes, the GREs were positioned in one of the nucleosomal exits.

6.2 Materials and methods

6.2.1 DNA containing c-Jun and GR response elements

The response element for c-Jun, 5'-TGA^{CT}CAG-3', was inserted into a DNA construct with an ATTO647N modified primer via PCR. The size of the DNA construct was 198 base pairs and contained the Widom 601 sequence between base pairs 40 and 191. The c-Jun part of the GJE sequence was positioned at base pairs 53 to 60. The Widom 601 sequence itself included several partial c-Jun response elements, most notably 5'-TCAG-3', at different locations. DNA-GJE also contained a GR response element.

Several DNA constructs were made containing the complete Glucocorticoid Response Element (GRE) 5'-TCTTGTtgcACAAGA-3' or half the element: 5'-TCTTGTtgcctcaggc-3' (hGRE). The GRE was inserted through a modified primer at the PCR step (see Supplement for primers, protocols, DNA sequences and label positions). The DNA constructs were labeled with ATTO647N at base pair 41. DNA was mixed with human recombinant histones in a titration of molar ratios ranging from 1:1 to 1:3. Nucleosomes were reconstituted by salt gradient dialysis from 2 M to 0 mM NaCl overnight. Only titrations where no unreconstituted DNA was detected in gel after electrophoresis were used for F(C)CS experiments. Measurement buffers contained 10 mM Tris and 1 mM NaCl, unless stated otherwise. Nucleosome concentrations in FCS measurements were between 3 and 7 nM. Samples of 20 to 40 μ l were placed in a closed flowcell to minimize evaporation.

6.2.2 Recombinant c-Jun

Recombinant c-Jun was acquired from Active Motif (5 μ g, catalog no. 31116) diluted in buffer of 20 mM Tris-Cl (pH 8), 20% glycerol, 100 mM KCl, 1 mM DTT and 0.2 mM EDTA. The buffer used to perform FCS measurements consisted of 10 mM Tris-HCl (pH 8). The concentration of DNA was 2 nM in all measurements, c-Jun was added to obtain molar ratios 1:0.1, 1:0.3, 1:0.7 and 1:1 (DNA:protein).

6.2.3 GR transfection and activation

Human GR α N-terminally tagged with EYFP was obtained from transgenic COS-1 cells. As these cells are known to not express GR, complete labelling

of the GR population could be ensured.

COS-1 cells were grown in Dulbecco's Modified Eagle Medium (DMEM, Sigma D1145) containing 4500 mg/L glucose before transfection. DMEM lacked L-glutamine, sodium pyruvate and phenol red; therefore glutaMAX-1 (2 mM) and sodium pyruvate (1 mM) were added to the DMEM stock. Phenol red was omitted to minimize background of red fluorescence during FCS measurements. Fetal calf serum (fcs) was 10x diluted in the incubation buffer. Cells were grown at 37°C and 5% CO₂. Cell transfer was performed after 3-4 days with trypsin added as a mixture of 45 ml/L PBS/EDTA plus 5 mL 10x trypsin 25%. Cells were transferred into T25 vials at 1 to 10 ratio. COS-1 cells were transfected with a GR-EYFP DNA vector provided by dr. Schaaf[267]. Our transfection protocol was based on a protocol from Fugene HD transfection reagent (Promega). At 80% confluency cells were detached from the T25 vial into 2 mL DMEM Δ fcs. Cells were plated on p-100 plates at a density of $7.5 \cdot 10^5$ cells per plate. DMEM Δ fcs was added to an end volume of 4 mL per plate and incubated at 37°C for 24 hours. 10 μ g of the plasmid containing EYFP-hGR was dissolved in 1 mL DMEM Δ fcs plus 30 μ L Fugene HD (left for 2 hours at room temperature prior to incubation). The cells were incubated at 37°C for 24 hours after which the medium was refreshed with DMEM Δ fcs and incubated for another 24 hours. After this, the percentage of transfected cells was determined using a confocal microscope (EVOS FLAuto2, Thermofisher). This percentage was between 70% and 85% (N = 4).

hGR-EYFP was activated with corticosterone or dexamethasone in EtOH. 30 μ L of 1 mM of the hormone was added to the total volume of 30 mL and the cells were incubated for 50 minutes at 37°C.

Cytoplasmic and nuclear extracts were acquired following the protocol of the Nuclear Extract Kit (Active Motif, 40010/40410, protocol version D3). The cells were collected on ice in a PBS/Phosphatase Inhibitor buffer from the kit to minimize protein activity. The cells were then resuspended in Hypotonic Buffer from the kit to swell them and weaken their membranes. Detergent buffer was added to induce leakage of the cytoplasmic proteins into the supernatant. The samples were centrifuged for 30 seconds at 14000 x g in a micro-centrifuge cooled to 4°C. After collection of the supernatant containing the cytoplasmic fraction, the nuclei in the pellet were lysated and solubilized in Lysis buffer from the kit.

The extracts contained a plethora of other unlabeled proteins and the

overall protein concentration needed to be determined first. This was done by Bradford method (Coomassie Protein Assay Kit 23200, Thermoscientific). The total protein concentration in the nuclear extract containing GR activated with dexamethasone was 726 $\mu\text{g}/\text{mL}$. A TransAM GR kit based on the ELISA method (Active Motif, 45496, protocol version A1) was used to determine GR activity in the cytoplasmic and nuclear extracts. The extracts were each loaded into a well of a 96-well plate coated with DNA oligomers containing the GRE consensus sequence (5'-GGTACAnnnTGTCT-3'). The TransAM protocol allows for 2-20 μg of protein per well, so 5 μL (= 3.6 μg) of the nuclear extract used in the Bradford was used for TransAM. The GR concentrations of all extracts were determined from FCS experiments, by assessing the number of proteins from the amplitude of the correlation curve and the average intensity (photons/sec). Extracts were diluted to match the EYFP-GR concentration of the dexamethasone-activated nuclear extract. By doing so, the relative difference in activity between extracts was measured.

After incubation of the GR in the extracts in the TransAM plate and washing, primary GR antibodies were added to the wells. After incubation and washing, secondary antibodies (anti-IgG HRP-conjugated) were added which were activated with a developing solution from the kit and stopped after 20 minutes. Directly after stop solution from the kit was added, absorbance was measured on a spectrophotometer at 514 nm using a reference absorbance at 655 nm.

6.2.4 Single-molecule fluorescence correlation spectroscopy

Measurements were performed on a home-built confocal microscope with a water-immersion objective (60x, NA 1.2, Olympus), using an ICHROME MLE-SFG laser. The excitation beam was directed via fiber coupler and a dichroic mirror (z514/640rpc, Chroma) into the objective and focused 50 μm above the glass-sample interface. cJun-DNA measurements were done by continuous excitation at 632 nm. F(C)CS was performed on GR-DNA and GR-nucleosome in experiments using pulsed interleaved excitation (PIE) mode by alternating 514 nm (30 μW) and 632 nm (20 μW) 100 ns excitation pulses with 300 ns intermittent dark periods. Fluorescence was spatially filtered with a 50 μm pinhole in the image plane and split by a second dichroic mirror (640dcxr, Chroma). The fluorescent signals were further filtered (hq570/100nm and hq700/75nm, resp.) and focused on the

active area of single photon avalanche photodiodes (SPADs, SPCM AQR-14, Perkin Elmer). The photodiodes were read out with a TimeHarp 200 photon counting board (Picoquant), and the arrival times of the collected photons were stored in t3r (time-tagged to time-resolved) files. PIE-F(C)CS measurements were done for a least 30 minutes, in recordings of at least 2 minutes. These recordings were further processed by home-built Python analysis programs.

6.2.5 FCCS analysis and binding affinity

Due to Brownian motion, fluorescently labeled molecules diffuse in and out of the confocal volume, causing the fluorescence intensity to fluctuate in time. The fluctuations of the intensity were analyzed by correlating the photon arrival times over increasing time-lag τ :

$$G(\tau)_{diff} = \frac{\langle \delta I_1(t) \cdot \delta I_2(t + \tau) \rangle}{\langle I_1(t) \rangle \langle I_2(t) \rangle} \quad (6.1)$$

To assess the diffusion of a molecule photon streams I_1 and I_2 were correlated to generate an autocorrelation curve ($I_1 = I_2$). To quantify the fraction of two differently labeled molecules diffusing through the focus at the same time (i.e. as a complex) the signal of one molecule (I_1) was correlated with the signal of another molecule (I_2) to generate a crosscorrelation curve. The correlation curve $G(\tau)$ depends on the concentration and diffusion time of the labeled molecules, as well as the confocal volume which they diffuse through:

$$G(\tau) = N^{-1} \cdot (1 + \tau/\tau_D)^{-1} \cdot (1 + a^{-2} \cdot \tau/\tau_D)^{-1/2} \quad (6.2)$$

with diffusion time τ_D and average number of molecules N in the focal volume. Parameter a is the ratio between the axial and radial size of the confocal volume and was determined through calibration experiments to be 8. Background signal, photophysics of the fluorophore (transiting to the triplet state / dark state) and afterpulsing effects were included in the fit of the correlation curve, see chapter 2 of this thesis. Binding affinity of proteins to DNA or nucleosomes was defined as the dissociation constant derived from the concentrations of proteins and DNA (or nucleosomes), and complex:

$$K_d = \frac{[DNA] \cdot [protein]}{[complex]} \quad (6.3)$$

The dissociation constant equals the concentration of DNA or nucleosome at which half of the available binding sites are occupied by protein. A lower value of K_d therefore corresponds to a higher affinity of the protein to the ligand.

6.3 Results

6.3.1 c-Jun interactions with DNA

Transcription factor c-Jun was added to DNA containing or lacking the response element GJE. Figures 5.1 a-d show representative time traces of different molecular ratios of c-Jun to DNA (all containing the GJE except fig. 6.1c). By qualitative observation it was obvious that increasing the c-Jun concentration introduced large DNA condensates. In order to quantify this, the mean and standard deviation (sd) of the intensity of fluorophore ATTO647N were calculated. In the absence of c-Jun, the photon signal of labeled DNA stayed almost completely within 2 sd of the average signal (figure 6.1a, $I = 2.48 \pm 0.12$ kHz (mean \pm sd)). Upon introducing a 1:0.1 DNA to c-Jun ratio, the photon signal became more erratic and the standard deviation increased (figure 6.1b). Nevertheless, the photon signal was mostly within 2x sd (17% of the mean). At a DNA:c-Jun ratio of 1:0.3 (figure 6.1c) the effect of condensation was clearly visible. When measured for a longer time, parts of the time trace containing condensates could be discarded before for correlation analysis. However, measuring for 200 seconds did not yield enough data without condensates for the experiment 1:0.3 DNA(-):c-Jun to be used for correlation analysis.

At a 1:0.7 ratio of DNA:c-Jun time traces of both DNA(-) and DNA(GJE) contained very large condensates. As a result, the mean and sd were larger than we anticipated for the concentration of DNA. Next to very large aggregates, we also observed smaller condensates that could not fully be excluded from time traces, as shown in the inset of figure 6.1d.

Figure 6.1e shows the effectiveness of aggregate exclusion by selection. for DNA only, 1:0.1 and 1:0.3 DNA:c-Jun measurements the normalized curves overlapped. Correlation curves from 1:0.7 experiments resulted in a slightly worse fit (figure 6.1f).

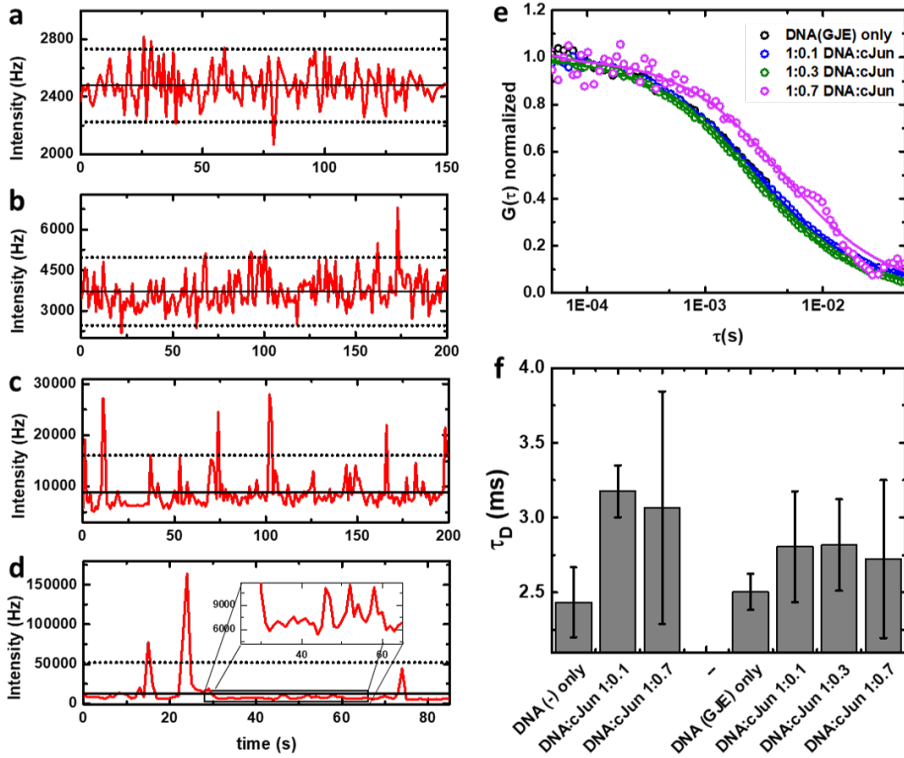


FIGURE 6.1: **Nonspecific aggregation of c-Jun on DNA.** **a) - d)** Time traces (red) of DNA(GJE)-ATTO647N from continuous 632 nm excitation, with no **(a)**, 1:0.1 **(b)**, 1:0.3 **(c)** and 1:0.7 **(d)** ratio of DNA to c-Jun. Increasing c-Jun concentration introduced more and large condensates, thereby increasing the variance (dots, 2x variance) from the intensity (mean = black line). **e)** Addition of unlabeled c-Jun to DNA resulted in correlation curves more difficult to fit with one population (purple curve). **f)** Averaging over several experiments and excluding aggregates yielded uncompromised correlation curves, with small deviations of the diffusion times, when bursts from condensates were discarded.

6.3.2 GR activity

In order to have a completely labeled population of a transcription factor, a DNA vector translating to GR fused to EYFP was used to transfect COS1 cells as described in the Methods section. After sufficient expression, GR was activated with dexamethasone or corticosterone. Figures 6.2a-f show

the localization of GR in the nucleus upon activation with dexamethasone. Directly after adding hormone, GR was predominantly localized in the cytoplasm; the nuclei are less fluorescent than the cytoplasm in figure 6.2a. After 24 minutes the cells' nuclei started to become brighter (figure 6.2c), and after 44 minutes GR appeared to be mostly localized in the nuclei. From previous activation experiments we learned to allow for 5 to 10 more minutes for residual GR to go into the nucleus (figure 6.1f).

After activation, cells were collected and lysated to obtain cytoplasmic and nuclear extract (described in Methods). GR concentration was determined through FCS measurements and average fluorescent intensities. Different extracts were diluted to similar concentrations to determine GR activity. The ELISA based TransAM kit was used as described. Figure 6.2g shows the optical density (OD, or extinction coefficient) at 514 nm excitation. The OD values of different samples revealed the relative GR activity. We observed that at similar concentrations, GR in nuclear extract activated with dexamethasone contained twice more functional GR compared to its cytoplasmic counterpart. This implies that half of the GR in the cytoplasmic extract could not bind to DNA and was therefore inactive. Cytoplasmic and nuclear extracts after corticosterone activation showed equal levels of GR activity, implying that the cytoplasm still contained a substantial population of activated GR. Subsequent experiments were performed with nuclear extracts after dexamethasone activation.

GR affinity for one of the DNA-GRE constructs (GRE3) was tested by EMSA. Figure 6.3a shows that GR in nuclear extract did not appear to have a defined band in the gel; the fluorescent signal in lane 1 showed a wide dispersion. Without nuclear extract the DNA appeared as a clear band (lane 2), when GR was added at a 1:1 ratio the signal of DNA was completely dispersed in the gel (lane #4). For higher concentrations of DNA the DNA signal became visible again, although not in a defined band (lanes 5-8 show ratios 1:2, 1:4, 1:8, 1:16 respectively); the signal of GR was still very dispersed in the lanes. We argue that unlabeled components (proteins, RNA) from the nuclear extract may interact nonspecifically with the GR and DNA, thereby preventing the formation or detection of clearly defined GR · DNA complexes.

Measuring GR in FCS was done in two modes of excitation: pulsed (PIE) and continuous (figure 6.3b). PIE reduced the photophysical effect known as flickering (blinking of fluorophore EYFP in the range of micro- to

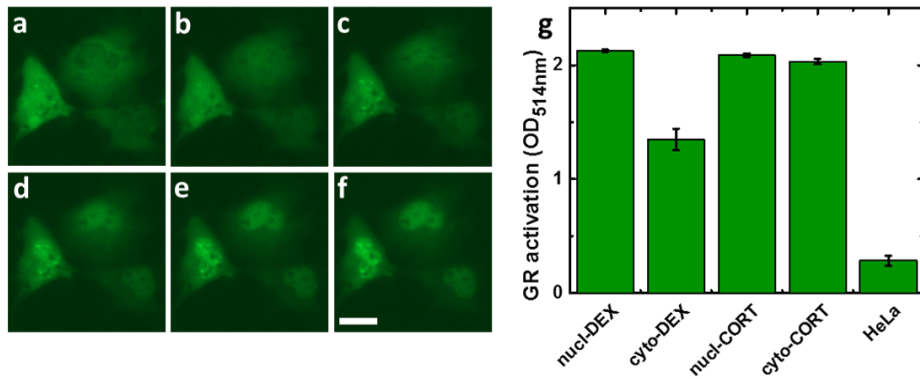


FIGURE 6.2: **Activated GR in nuclear extract binds to DNA containing a GRE.** a) - f) GR-EYFP in COS-1 cells was localized predominantly in the cytoplasm before activation. After activation with dexamethasone images were taken at 4 (a), 13 (b), 24 (c), 35 (d), 44 (e) and 50 minutes (f). Scale bar: 10 μ m. g) GR activity was measured with ELISA based method TransAM. GR activated with corticosterone mainly localized to the nucleus (nucl-CORT), but part of the active GR was still present in the cytoplasm (cyto-CORT). To estimate background, samples containing GR were compared to samples from HeLa cells (containing no EYFP labeled GR). Error bars represent standard deviations of 2 or more samples.

milliseconds) making the diffusion part of the autocorrelation curve more prominent. The resulting diffusion time of GR was 3.6 ± 0.7 ms, which corresponds to a hydrodynamic radius of 25 ± 5 nm. Considering the size of a GR dimer from electron microscopy studies to be in the order of 8 nm [268][187], the results from gel and PIE-FCS suggest that activated GR exists in a larger complex in the nuclear extract, even when taking into account the added size of the EYFP.

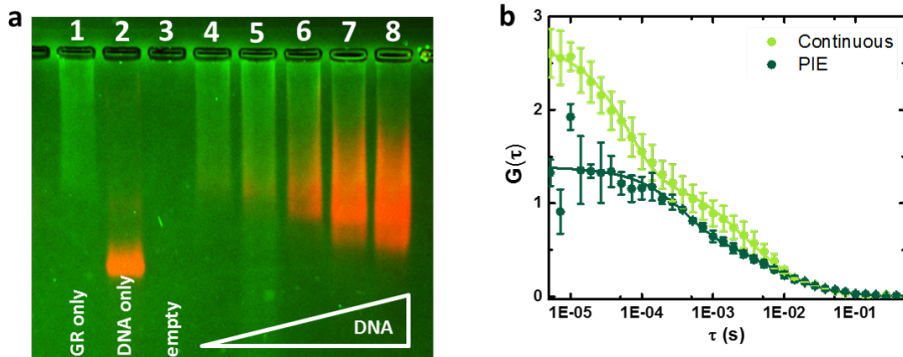


FIGURE 6.3: **Nuclear extract containing activated GR interacts nonspecifically with DNA.** **a)** Nuclear extract containing activated GR (EYFP labeled, green, lane 1) interacted with DNA construct GRE3 (Atto647N labeled, red, lane 2) in a 1% agarose gel. Molecular ratios of GR to DNA in lanes 4-8 were 1:1, 1:2, 1:4, 1:8 and 1:16. Unlabeled components of the nuclear extract seemed to nonspecifically interact with GR, as in lanes 1 and 4-8 its signal was dispersed as well. **b)** FCS with sub-microsecond PIE modulation reduced flickering of EYFP compared to continuous excitation with 514 nm. Fitting the autocorrelation curve from PIE-FCS measurements resulted in a diffusion time of 3.6 ± 0.7 ms for GR.

6.3.3 GR affinity for DNA and nucleosomes

PIE-FCCS measurements were performed on DNA constructs GREh, GRE2 and GRE3 and the nucleosomes reconstituted using these DNA substrates (see supplement for full sequences). Nuclear extract containing GR activated with dexamethasone was added to a molecular ratio between DNA or nucleosomes with GR of approximately 1:1. Auto- and crosscorrelation curves were computed to quantify protein affinity. Figure 6.4a shows representative plots of these curves. The curves were fitted to eq. 5.2 to obtain the number of molecules for each species. In figure 6.4b the number GR proteins, nucleosomes and complexes fitted from FCS experiments on three reconstituted nucleosomes are shown. We obtained similar results for all sequences. We did the same measurements on bare DNA substrates and obtained very similar concentrations (data not shown).

From the obtained concentrations we calculated the binding affinities; all affinities were larger than 15 nM. The dissociation constants of the DNA constructs in figure 6.4c were similar for all substrates (hGRE: 25 ± 8 nM,

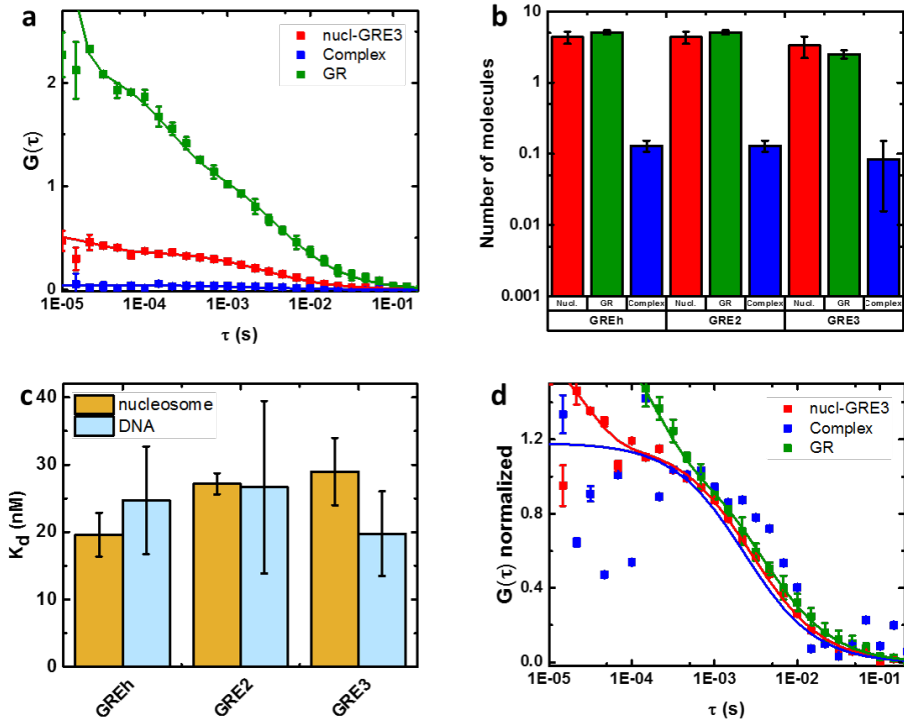


FIGURE 6.4: **GR-nucleosome binding depends on GRE position.** **a)** Representative auto- and crosscorrelation curves from photon signals corresponding to nucleosome (red), GR (green) and the complex nucleosome-GR (blue). **b)** The concentrations from fitting the correlation curves were used to calculate the dissociation constant K_d for three DNA constructs incorporating the GRE. **c)** Dissociation constant for nucleosome-GR interaction shows a trend of decreasing affinity when the GRE is positioned more towards the nucleosome dyad. Between DNA constructs where the position of the GRE differed no difference in affinity was observed. **d)** Normalization of the correlation curves in 5.4a shows that the complex is not diffusing significantly slower compared to either GR or nucleosome.

GRE2: 27 ± 13 nM, GRE3: 20 ± 6 nM). Nucleosome hGRE (K_d : 20 ± 3 nM) appeared to have a slightly higher affinity than GRE2 (K_d : 27 ± 2 nM) and as GRE3 (K_d : 29 ± 5 nM). This result cannot confirm the GRE was less accessible to GR when placed further inside the nucleosome.

As the DNA-GR complex made up a very small part of the mix, the resulting crosscorrelation curves had a small amplitude. For better visualization the curves were normalized (figure 6.4d). Unexpectedly, the fit to the curve corresponding to the complex had a similar diffusion time as the free nucleosome, suggesting a more complex binding pattern. The diffusion times of the DNA/nucleosomes and GR in interaction experiments did not differ significantly compared to their diffusion times without the other component. However, because of increased noise, the crosscorrelation curve could not be fitted as accurately as one species of molecules.

6.3.4 Increasing nucleosome concentration increases complex concentration

Because the concentration of bound GR was close to the detection limit, we repeated the experiment at higher nucleosome concentrations. Indeed, the number of nucleosome-GR complexes increased and fits of both experiments resulted in similar dissociation constants: 34 ± 4 nM (1:1) and 25 ± 4 nM (1:10). Because the number of molecules were more difficult to fit for the complex (figure 6.4d), we decided to also investigate the changes in diffusion time of the nucleosome and GR in interaction experiments.

Upon increasing the concentration of nucleosomes, the correlation curves shifted to slightly larger correlation times (orange and red curve in figure 6.5b). However, fitting the correlation curves did not result in significantly different diffusion times (figure 6.5c, red bars). The same was found for the diffusion times of GR (figure 6.5c, green bars).

Summation of simulated correlation curves of nucleosomes consisting of free nucleosomes and nucleosomes bound to an increasing fraction of GR protein offered an explanation for the absence of differences seen in our experiments: the inset in figure 6.5d shows that the curves for 0% and 25% bound cannot be distinguished from one another, assuming a standard deviation of 5%. This implied a higher affinity (resulting in a higher percentage of bound protein) is needed in order to confirm binding through difference in diffusion times. Simulated data were computed by composing a τ_D of different fractions of the diffusion times of free nu-

cleosomes and nucleosomes bound to GR; for the latter we assumed the diffusion times of nucleosome and GR as found in measurements, and in a 1:1 binding ratio. For example, for 25% binding, the diffusion time was calculated as $\tau_{D,comp} = 0.75 \cdot \tau_{D,freeNucl} + 0.25 \cdot \tau_{D,boundNucl}$, with $\tau_{D,boundNucl} = \tau_{D,freeNucl} + \tau_{D,freeGR}$.

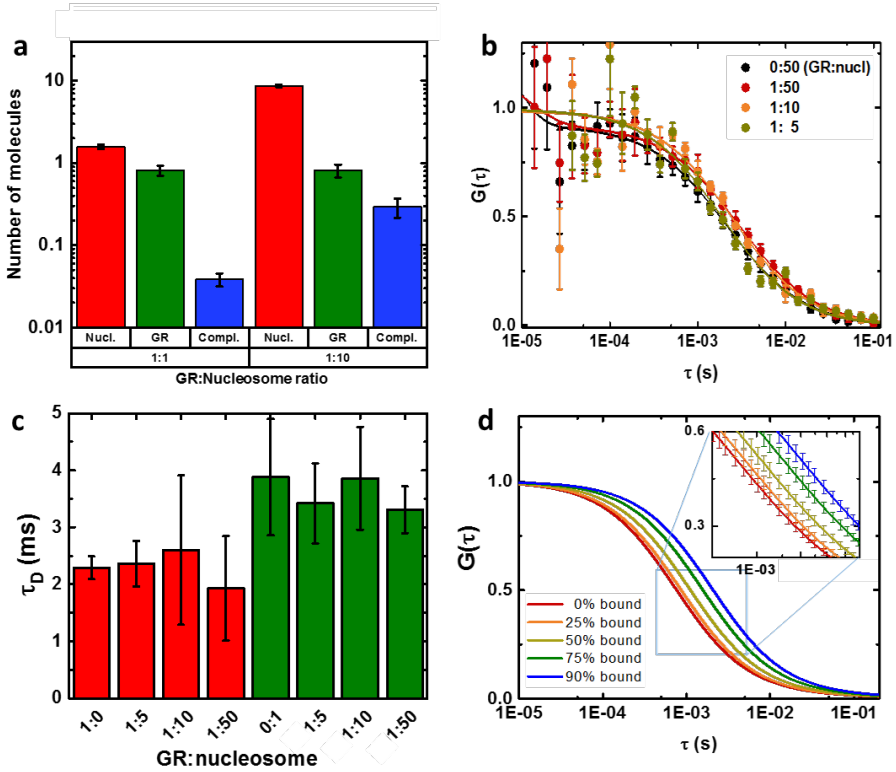


FIGURE 6.5: Increasing concentrations of GR or nucleosome increased concentration of the GR-nucleosome complex. **a**) Increasing nucleosome concentration tenfold increased the complex concentration. **b**) Increasing nucleosome GRE3 concentration showed a small shift for higher concentrations of nucleosome. **c**) However, diffusion times of nucleosome GRE3 or GR did not increase significantly upon increasing the concentration of nucleosome. **d**) Simulating nucleosome diffusion with increasing GR binding revealed a significant difference in correlation curve could only be observed when more than 25% bound protein.

6.4 Discussion and conclusions

Using FCS we demonstrated that mixing recombinant c-Jun with DNA constructs both lacking and containing a c-Jun binding element induces DNA aggregation. For both DNA constructs the size of the condensates increased with the concentration of c-Jun, while their frequency seemed to decrease. We did not quantify the frequency and intensity of the condensates, but FCS does offer the possibility to do so, since we were able to identify and exclude (most of) them from further analysis. We have shown that after exclusion of condensates, addition of c-Jun slightly increased the diffusion time of DNA. Increasing the concentration of c-Jun did not further increase the diffusion time of DNA when the signal was filtered from condensate contributions. These observations point to nonspecific interactions of c-Jun with DNA and might imply a DNA-condensing role for c-Jun during transcription. It is possible to increase specificity of c-Jun through methylation of the DNA binding site [245] [246] or addition of the protein c-Fos[250][251]; however, as we were not able to tag c-Jun with a fluorescent label, further experiments to see if c-Jun has a higher affinity for methylated DNA constructs containing the GJE binding element were not pursued.

For GR to exhibit any binding to DNA, the protein needs to be activated to detach from the heat shock proteins complex it resides in when in the cytoplasm[269]. We used dexamethasone as well as cortisol to activate GR. Translocation to the nucleus occurred for both hormones. As described, COS-1 cells containing activated GR were processed in both nuclear extracts and cytoplasmic extracts. All extracts were tested with an ELISA kit; the cytoplasmic extract from dexamethasone activation exhibited a lower affinity than the associated nuclear extract, implying a difference in activity. A difference in binding affinity depending on the hormone used for activation has been observed before by Schaaf et al.[258][234][265]

In agarose gel, GR-EYFP(dex) in the nuclear extract was visible as a smeared band in the high molecular weight region around 1000-1200 bp. The smearing might stem from nonspecific, short-lived interactions with other proteins in the extract[270][271][261] as has been observed before in gel for nucleosomes and purified GR by Perlmann et al. [91][93][92], and nucleosomes and LexA by Li and Widom[50]; it could also be an intrinsic property of the GR existing in a disordered state, which is often related to a protein's level of activity [272][273]. Adding a 200bp DNA construct labeled with Atto647N resulted in the DNA construct smearing in the lane centered around size 500

bp. Increasing the ratio of DNA to nuclear extract widened the DNA smear but shifted its center to smaller sizes. A possible explanation for this is that more DNA may distribute proteins in the extract over more DNA fragments, yielding less complexes carrying multiple DNA binding proteins, thus allowing DNA to move further down through the gel. The smearing appeared to be independent of a GRE present in the DNA construct, fortifying the idea that not only the GR, but also other proteins in the extract interacted with the DNA [264][263][262].

Consistent with this, in FCCS the cross-correlation curve, complexes of GR with either DNA or nucleosome, were barely visible, implying a low concentration of a complex. For all DNA and nucleosome constructs the binding affinities were 20 nM and larger. Statistically there was no significant difference in K_d for DNA constructs GREh, GRE2 and GRE3, which was different than previous results from Jin[95] and Wrangle[94][181], who have shown that the compaction of DNA into nucleosomes, as well as embedding the GRE position in nucleosomes increases the affinity of GR. Here, GR had the highest affinity for nucleosomes reconstituted from GREh DNA. Although differences in affinity were small, it appeared that K_d depends on accessibility of the GRE in nucleosome, i.e. having a GRE positioned closer to the nucleosomal exit increases access for GR. The difference in affinity of GR for GRE-nucleosomes might become more apparent though at higher salt concentrations, as we have shown in this thesis that differences in nucleosomal dynamics and stability appeared mostly at salt concentrations higher than 15 mM.

As mentioned, the signal in the cross-correlation channel was very low (10-100 photons/sec), requiring long data acquisition times. In addition, we observed anti-correlation at microsecond timescales, likely from EYFP photophysics[127]. Despite these technical difficulties, the small amplitude cross-correlation curve does show a plateau at larger tau (implying slower diffusion, i.e. larger molecule) compared to the autocorrelation curves from GR and DNA. The incline of the slope however, is steeper and uncharacteristic of normal 3D diffusion, implying more convoluted dynamics than only diffusion. The timescale of the steeper incline (milliseconds) does not coincide with that of EYFP-flickering, which happens at shorter times (nano to microseconds). Our curve-fitting algorithm converged most of the times to a plateau of the curve (fits were visually inspected after automated fitting), allowing for estimation of the complex concentration.

The binding affinities found via PIE-FCCS resembled those reported *in vitro* [92][181]. Observations in FCS and in gel matched nonspecific binding observed *in vivo* [234][233][274], where binding times of milliseconds are the predominant mode of interaction[265].

In vivo, specific binding events of seconds to minutes have been reported, which may be enhanced through crowding [275][276][277][278][279]. Physiological crowding conditions can be mimicked through adding PEG to DNA-GR mixtures; however, addition of PEG to nucleosomes causes the nucleosomes to aggregate, and slows the diffusion of all constituents in the sample, which would then needed to be characterized through separate measurements.

A small shift in the correlation curve of nucleosome GRE3 towards larger τ was observed when increasing the ratio of nucleosome to GR, but the difference was so minute it did not lead to significantly larger diffusion times when fitted. This observation points again toward an abundance of nonspecific interactions of the constituents in the extract with DNA or nucleosomes.

During measurements, large condensates of both DNA/nucleosomes and GR were observed, but the frequency and intensity differed between extracts and were therefore initially discarded. It might be that these condensates are the *ansatz* of pre-complex bubbles, increasing local protein concentrations by macromolecular crowding / volume exclusion [280][281][282][283].

Bibliography

- [1] Kay, L. E. A book of life?: How the genome became an information system and DNA a language. *Perspectives in biology and medicine* **1998**, 41 (4), 504–528.
- [2] Edenberg, E.; Downey, M.; Toczyski, D. Polymerase stalling during replication, transcription and translation. *Current Biology* **2014**, 24 (10), R445–R452.
- [3] Annunziato, A. DNA packaging: nucleosomes and chromatin. *Nature Education* **2008**, 1 (1), 26.
- [4] Kornberg, R. D. Chromatin Structure: A Repeating Unit of Histones and DNA: Chromatin structure is based on a repeating unit of eight histone molecules and about 200 DNA base pairs. *Science* **1974**, 184 (4139), 868–871.
- [5] Woodcock, C.; Safer, J.; Stanchfield, J. Structural repeating units in chromatin: I. Evidence for their general occurrence. *Experimental cell research* **1976**, 97 (1), 101–110.
- [6] Owen-Hughes, T.; Workman, J. L. Experimental analysis of chromatin function in transcription control. *Critical reviews in eukaryotic gene expression* **1994**, 4 (4), 403–441.
- [7] Van Holde, K. E. Chromatin. Springer Science & Business Media, **2012**.
- [8] Olins, D. E.; Olins, A. L. Chromatin history: our view from the bridge. *Nature reviews Molecular cell biology* **2003**, 4 (10), 809–814.
- [9] Maeshima, K.; Ide, S.; Hibino, K.; Sasai, M. Liquid-like behavior of chromatin. *Current opinion in genetics & development* **2016**, 37, 36–45.
- [10] Everid, A.; Small, J.; Davies, H. Electron-microscope observations on the structure of condensed chromatin: evidence for orderly arrays of

-
- unit threads on the surface of chicken erythrocyte nuclei. *Journal of cell science* **1970**, 7 (1), 35–48.
- [11] Oudet, P.; Gross-Bellard, M.; Chambon, P. Electron microscopic and biochemical evidence that chromatin structure is a repeating unit. *Cell* **1975**, 4 (4), 281–300.
- [12] Dorigo, B.; Schalch, T.; Kulangara, A.; Duda, S.; Schroeder, R. R.; Richmond, T. J. Nucleosome arrays reveal the two-start organization of the chromatin fiber. *Science* **2004**, 306 (5701), 1571–1573.
- [13] Song, F.; Chen, P.; Sun, D.; Wang, M.; Dong, L.; Liang, D.; Xu, R.-M.; Zhu, P.; Li, G. Cryo-EM study of the chromatin fiber reveals a double helix twisted by tetranucleosomal units. *Science* **2014**, 344 (6182), 376–380.
- [14] Fazary, A. E.; Ju, Y.-H.; Abd-Rabboh, H. S. How does chromatin package DNA within nucleus and regulate gene expression? *International journal of biological macromolecules* **2017**, 101, 862–881.
- [15] Nora, E. P.; Lajoie, B. R.; Schulz, E. G.; Giorgetti, L.; Okamoto, I.; Servant, N.; Piolot, T.; Van Berkum, N. L.; Meisig, J.; Sedat, J.; et al. Spatial partitioning of the regulatory landscape of the X-inactivation centre. *Nature* **2012**, 485 (7398), 381–385.
- [16] Babu, A.; Verma, R. S. Chromosome structure: euchromatin and heterochromatin. *International review of cytology* **1987**, 108, 1–60.
- [17] Schwartz, U.; Németh, A.; Diermeier, S.; Exler, J. H.; Hansch, S.; Maldonado, R.; Heizinger, L.; Merkl, R.; Längst, G. Characterizing the nuclease accessibility of DNA in human cells to map higher order structures of chromatin. *Nucleic acids research* **2019**, 47 (3), 1239–1254.
- [18] Shashikant, T.; Khor, J. M.; Ettensohn, C. A. Global analysis of primary mesenchyme cell cis-regulatory modules by chromatin accessibility profiling. *BMC genomics* **2018**, 19 (1), 1–18.
- [19] Mueller, B.; Mieczkowski, J.; Kundu, S.; Wang, P.; Sadreyev, R.; Tolstorukov, M. Y.; Kingston, R. E. Widespread changes in nucleosome accessibility without changes in nucleosome occupancy during a

- rapid transcriptional induction. *Genes & development* **2017**, 31 (5), 451–462.
- [20] Dixon, J. R.; Selvaraj, S.; Yue, F.; Kim, A.; Li, Y.; Shen, Y.; Hu, M.; Liu, J. S.; Ren, B. Topological domains in mammalian genomes identified by analysis of chromatin interactions. *Nature* **2012**, 485 (7398), 376–380.
- [21] Erdel, F.; Rippe, K. Formation of chromatin subcompartments by phase separation. *Biophysical journal* **2018**, 114 (10), 2262–2270.
- [22] Strom, A. R.; Emelyanov, A. V.; Mir, M.; Fyodorov, D. V.; Darzacq, X.; Karpen, G. H. Phase separation drives heterochromatin domain formation. *Nature* **2017**, 547 (7662), 241–245.
- [23] Wang, N.; Liu, C. Implications of liquid–liquid phase separation in plant chromatin organization and transcriptional control. *Current Opinion in Genetics & Development* **2019**, 55, 59–65.
- [24] Peng, L.; Li, E.-M.; Xu, L.-Y. From start to end: Phase separation and transcriptional regulation. *Biochimica et Biophysica Acta (BBA)-Gene Regulatory Mechanisms* **2020**, 1863 (12), 194641.
- [25] Feric, M.; Misteli, T. Phase separation in genome organization across evolution. *Trends in cell biology* **2021**, 31 (8), 671–685.
- [26] Guo, Q.; Shi, X.; Wang, X. RNA and liquid-liquid phase separation. *Non-coding RNA Research* **2021**, 6 (2), 92–99.
- [27] Bonner, J.; Ru-chih, C. H. Properties of chromosomal nucleohistone. *Journal of Molecular Biology* **1963**, 6 (3), 169–174.
- [28] Beam, S.; Ris, H. On the structure of nucleohistone. *Journal of molecular biology* **1971**, 55 (3), 325–IN2.
- [29] Olins, A. L.; Olins, D. E. Spheroid chromatin units (ν bodies). *Science* **1974**, 183 (4122), 330–332.
- [30] Lieb, J. D.; Clarke, N. D. Control of transcription through intragenic patterns of nucleosome composition. *Cell* **2005**, 123 (7), 1187–1190.

-
- [31] Huang, R.-c. C.; Bonner, J. Histone, a suppressor of chromosomal RNA synthesis. *Proceedings of the National Academy of Sciences* **1962**, 48 (7), 1216–1222.
- [32] Thomas Jr, G.; Prescott, B.; Olins, D. Secondary structure of histones and DNA in chromatin. *Science* **1977**, 197 (4301), 385–388.
- [33] Olins, D. E.; Olins, A. L. Nucleosomes: The Structural Quantum in Chromosomes. *American Scientist* **1978**, 66 (6), 704–711.
- [34] Luger, K.; Mäder, A. W.; Richmond, R. K.; Sargent, D. F.; Richmond, T. J. Crystal structure of the nucleosome core particle at 2.8 Å resolution. *Nature* **1997**, 389 (6648), 251–260.
- [35] Luger, K.; Richmond, T. J. DNA binding within the nucleosome core. *Current Opinion in Structural Biology* **1998**, 8 (1), 33 – 40.
- [36] Thåström, A.; Gottesfeld, J.; Luger, K.; Widom, J. Histone- DNA binding free energy cannot be measured in dilution-driven dissociation experiments. *Biochemistry* **2004**, 43 (3), 736–741.
- [37] Luger, K. Dynamic nucleosomes. *Chromosome Research* **2006**, 14 (1), 5–16.
- [38] Bondarenko, V. A.; Steele, L. M.; Újvári, A.; Gaykalova, D. A.; Kulaeva, O. I.; Polikanov, Y. S.; Luse, D. S.; Studitsky, V. M. Nucleosomes can form a polar barrier to transcript elongation by RNA polymerase II. *Molecular cell* **2006**, 24 (3), 469–479.
- [39] Polach, K.; Widom, J. Mechanism of protein access to specific DNA sequences in chromatin: a dynamic equilibrium model for gene regulation. *Journal of molecular biology* **1995**, 254 (2), 130–149.
- [40] Lowary, P.; Widom, J. New DNA sequence rules for high affinity binding to histone octamer and sequence-directed nucleosome positioning. *Journal of molecular biology* **1998**, 276 (1), 19–42.
- [41] Thåström, A.; Lowary, P.; Widlund, H.; Cao, H.; Kubista, M.; Widom, J. Sequence motifs and free energies of selected natural and non-natural nucleosome positioning DNA sequences. *Journal of molecular biology* **1999**, 288 (2), 213–229.

- [42] McGinty, R. K.; Tan, S. Nucleosome structure and function. *Chemical reviews* **2015**, 115 (6), 2255–2273.
- [43] Drew, H. R.; Travers, A. A. DNA bending and its relation to nucleosome positioning. *Journal of molecular biology* **1985**, 186 (4), 773–790.
- [44] Bolshoy, A.; McNamara, P.; Harrington, R.; Trifonov, E. Curved DNA without AA: experimental estimation of all 16 DNA wedge angles. *Proceedings of the National Academy of Sciences* **1991**, 88 (6), 2312–2316.
- [45] Ioshikhes, I.; Bolshoy, A.; Trifonov, E. Preferred positions of AA and TT dinucleotides in aligned nucleosomal DNA sequences. *Journal of Biomolecular Structure and Dynamics* **1992**, 9 (6), 1111–1117.
- [46] Morozov, A. V.; Fortney, K.; Gaykalova, D. A.; Studitsky, V. M.; Widom, J.; Siggia, E. D. Using DNA mechanics to predict in vitro nucleosome positions and formation energies. *Nucleic acids research* **2009**, 37 (14), 4707–4722.
- [47] Ngo, T. T.; Zhang, Q.; Zhou, R.; Yodh, J. G.; Ha, T. Asymmetric unwrapping of nucleosomes under tension directed by DNA local flexibility. *Cell* **2015**, 160 (6), 1135–1144.
- [48] De Bruin, L.; Tompitak, M.; Eslami-Mossallam, B.; Schiessel, H. Why do nucleosomes unwrap asymmetrically? *The Journal of Physical Chemistry B* **2016**, 120 (26), 5855–5863.
- [49] Wondergem, J.; Schiessel, H.; Tompitak, M. Performing SELEX experiments in silico. *The Journal of chemical physics* **2017**, 147 (17), 174101.
- [50] Li, G.; Widom, J. Nucleosomes facilitate their own invasion. *Nature Structural and Molecular Biology* **2004**, 11 (8), 763–769.
- [51] Li, G.; Levitus, M.; Bustamante, C.; Widom, J. Rapid spontaneous accessibility of nucleosomal DNA. *Nature Structural and Molecular Biology* **2005**, 12 (1), 46–53.

-
- [52] Hodges, C.; Bintu, L.; Lubkowska, L.; Kashlev, M.; Bustamante, C. Nucleosomal fluctuations govern the transcription dynamics of RNA polymerase II. *Science* **2009**, 325 (5940), 626–628.
- [53] Koopmans, W. J.; Buning, R.; Schmidt, T.; Van Noort, J. spFRET using alternating excitation and FCS reveals progressive DNA unwrapping in nucleosomes. *Biophysical Journal* **2009**, 97 (1), 195–204.
- [54] Pennings, S.; Muyldermans, S.; Meersseman, G.; Wyns, L. Formation, stability and core histone positioning of nucleosomes reassembled on bent and other nucleosome-derived DNA. *Journal of molecular biology* **1989**, 207 (1), 183–192.
- [55] Teif, V. B.; Rippe, K. Predicting nucleosome positions on the DNA: combining intrinsic sequence preferences and remodeler activities. *Nucleic acids research* **2009**, 37 (17), 5641–5655.
- [56] Shogren-Knaak, M.; Ishii, H.; Sun, J.-M.; Pazin, M. J.; Davie, J. R.; Peterson, C. L. Histone H4-K16 acetylation controls chromatin structure and protein interactions. *Science* **2006**, 311 (5762), 844–847.
- [57] Erler, J.; Zhang, R.; Petridis, L.; Cheng, X.; Smith, J. C.; Langowski, J. The role of histone tails in the nucleosome: a computational study. *Biophysical journal* **2014**, 107 (12), 2911–2922.
- [58] Dorigo, B.; Schalch, T.; Bystricky, K.; Richmond, T. J. Chromatin fiber folding: requirement for the histone H4 N-terminal tail. *Journal of molecular biology* **2003**, 327 (1), 85–96.
- [59] Lu, X.; Simon, M. D.; Chodaparambil, J. V.; Hansen, J. C.; Shokat, K. M.; Luger, K. The effect of H3K79 dimethylation and H4K20 trimethylation on nucleosome and chromatin structure. *Nature structural & molecular biology* **2008**, 15 (10), 1122–1124.
- [60] Creyghton, M. P.; Cheng, A. W.; Welstead, G. G.; Kooistra, T.; Carey, B. W.; Steine, E. J.; Hanna, J.; Lodato, M. A.; Frampton, G. M.; Sharp, P. A.; et al. Histone H3K27ac separates active from poised enhancers and predicts developmental state. *Proceedings of the National Academy of Sciences* **2010**, 107 (50), 21931–21936.

- [61] Koch, C. M.; Andrews, R. M.; Flicek, P.; Dillon, S. C.; Karaöz, U.; Clelland, G. K.; Wilcox, S.; Beare, D. M.; Fowler, J. C.; Couttet, P.; et al. The landscape of histone modifications across 1% of the human genome in five human cell lines. *Genome research* **2007**, 17 (6), 691–707.
- [62] Guillemette, B.; Drogaris, P.; Lin, H.-H. S.; Armstrong, H.; Hiragami-Hamada, K.; Imhof, A.; Bonneil, E.; Thibault, P.; Verreault, A.; Festenstein, R. J. H3 lysine 4 is acetylated at active gene promoters and is regulated by H3 lysine 4 methylation. *PLoS genetics* **2011**, 7 (3), e1001354.
- [63] Zhiteneva, A.; Bonfiglio, J. J.; Makarov, A.; Colby, T.; Vagnarelli, P.; Schirmer, E. C.; Matic, I.; Earnshaw, W. C. Mitotic post-translational modifications of histones promote chromatin compaction in vitro. *Open biology* **2017**, 7 (9), 170076.
- [64] Wang, Q.; Zhang, Y.; Yang, C.; Xiong, H.; Lin, Y.; Yao, J.; Li, H.; Xie, L.; Zhao, W.; Yao, Y.; et al. Acetylation of metabolic enzymes coordinates carbon source utilization and metabolic flux. *Science* **2010**, 327 (5968), 1004–1007.
- [65] Zhao, S.; Xu, W.; Jiang, W.; Yu, W.; Lin, Y.; Zhang, T.; Yao, J.; Zhou, L.; Zeng, Y.; Li, H.; et al. Regulation of cellular metabolism by protein lysine acetylation. *Science* **2010**, 327 (5968), 1000–1004.
- [66] Barski, A.; Cuddapah, S.; Cui, K.; Roh, T.-Y.; Schones, D. E.; Wang, Z.; Wei, G.; Chepelev, I.; Zhao, K. High-resolution profiling of histone methylations in the human genome. *Cell* **2007**, 129 (4), 823–837.
- [67] Yang, K.; Greenberg, M. M. Histone tail sequences balance their role in genetic regulation and the need to protect DNA against destruction in nucleosome core particles containing abasic sites. *ChemBioChem* **2019**, 20 (1), 78–82.
- [68] Tsuchiya, M.; Dang, N.; Kerr, E. O.; Hu, D.; Steffen, K. K.; Oakes, J. A.; Kennedy, B. K.; Kaerberlein, M. Sirtuin-independent effects of nicotinamide on lifespan extension from calorie restriction in yeast. *Aging cell* **2006**, 5 (6), 505–514.

-
- [69] Greer, E. L.; Maures, T. J.; Hauswirth, A. G.; Green, E. M.; Leeman, D. S.; Maro, G. S.; Han, S.; Banko, M. R.; Gozani, O.; Brunet, A. Members of the H3K4 trimethylation complex regulate lifespan in a germline-dependent manner in *C. elegans*. *Nature* **2010**, 466 (7304), 383–387.
- [70] Li, F.; Mao, G.; Tong, D.; Huang, J.; Gu, L.; Yang, W.; Li, G.-M. The histone mark H3K36me3 regulates human DNA mismatch repair through its interaction with MutS α . *Cell* **2013**, 153 (3), 590–600.
- [71] Pai, C.-C.; Deegan, R. S.; Subramanian, L.; Gal, C.; Sarkar, S.; Blaikley, E. J.; Walker, C.; Hulme, L.; Bernhard, E.; Codlin, S.; et al. A histone H3K36 chromatin switch coordinates DNA double-strand break repair pathway choice. *Nature communications* **2014**, 5 (1), 1–11.
- [72] Huang, Y.; Gu, L.; Li, G.-M. H3K36me3-mediated mismatch repair preferentially protects actively transcribed genes from mutation. *Journal of Biological Chemistry* **2018**, 293 (20), 7811–7823.
- [73] Supek, F.; Lehner, B. Clustered mutation signatures reveal that error-prone DNA repair targets mutations to active genes. *Cell* **2017**, 170 (3), 534–547.
- [74] Chantalat, S.; Depaux, A.; Héry, P.; Barral, S.; Thuret, J.-Y.; Dimitrov, S.; Gérard, M. Histone H3 trimethylation at lysine 36 is associated with constitutive and facultative heterochromatin. *Genome research* **2011**, 21 (9), 1426–1437.
- [75] Cherepanov, P.; Sun, Z.-Y. J.; Rahman, S.; Maertens, G.; Wagner, G.; Engelman, A. Solution structure of the HIV-1 integrase-binding domain in LEDGF/p75. *Nature structural & molecular biology* **2005**, 12 (6), 526–532.
- [76] Ciuffi, A.; Llano, M.; Poeschla, E.; Hoffmann, C.; Leipzig, J.; Shinn, P.; Ecker, J. R.; Bushman, F. A role for LEDGF/p75 in targeting HIV DNA integration. *Nature medicine* **2005**, 11 (12), 1287–1289.
- [77] Shun, M.-C.; Raghavendra, N. K.; Vandegraaff, N.; Daigle, J. E.; Hughes, S.; Kellam, P.; Cherepanov, P.; Engelman, A. LEDGF/p75 functions downstream from preintegration complex formation to

- effect gene-specific HIV-1 integration. *Genes & development* **2007**, 21 (14), 1767–1778.
- [78] Keys, D. A.; Lee, B.-S.; Dodd, J. A.; Nguyen, T. T.; Vu, L.; Fantino, E.; Burson, L. M.; Nogi, Y.; Nomura, M. Multiprotein transcription factor UAF interacts with the upstream element of the yeast RNA polymerase I promoter and forms a stable preinitiation complex. *Genes & development* **1996**, 10 (7), 887–903.
- [79] Kim, H.; Tang, G.-Q.; Patel, S. S.; Ha, T. Opening–closing dynamics of the mitochondrial transcription pre-initiation complex. *Nucleic acids research* **2012**, 40 (1), 371–380.
- [80] Robertson, S.; Hapgood, J. P.; Louw, A. Glucocorticoid receptor concentration and the ability to dimerize influence nuclear translocation and distribution. *Steroids* **2013**, 78 (2), 182–194.
- [81] Pratt, W. B.; Toft, D. O. Steroid Receptor Interactions with Heat Shock Protein and Immunophilin Chaperones. *Endocrine reviews* **1997**, 18 (3), 306–361.
- [82] Pratt, W. B.; Silverstein, A. M.; Galigniana, M. D. A model for the cytoplasmic trafficking of signalling proteins involving the hsp90-binding immunophilins and p50cdc37. *Cellular signalling* **1999**, 11 (12), 839–851.
- [83] Petta, I.; Dejager, L.; Ballegeer, M.; Lievens, S.; Tavernier, J.; De Bosscher, K.; Libert, C. The interactome of the glucocorticoid receptor and its influence on the actions of glucocorticoids in combatting inflammatory and infectious diseases. *Microbiology and Molecular Biology Reviews* **2016**, 80 (2), 495–522.
- [84] Scheinman, R. I.; Gualberto, A.; Jewell, C. M.; Cidlowski, J. A.; Baldwin Jr, A. S. Characterization of mechanisms involved in transrepression of NF-kappa B by activated glucocorticoid receptors. *Molecular and cellular biology* **1995**, 15 (2), 943–953.
- [85] McNally, J. G.; Müller, W. G.; Walker, D.; Wolford, R.; Hager, G. L. The glucocorticoid receptor: rapid exchange with regulatory sites in living cells. *Science* **2000**, 287 (5456), 1262–1265.

-
- [86] Dostert, A.; Heinzl, T. Negative glucocorticoid receptor response elements and their role in glucocorticoid action. *Current pharmaceutical design* **2004**, 10 (23), 2807.
- [87] Chen, S.-y.; Wang, J.; Yu, G.-q.; Liu, W.; Pearce, D. Androgen and glucocorticoid receptor heterodimer formation: a possible mechanism for mutual inhibition of transcriptional activity. *Journal of Biological Chemistry* **1997**, 272 (22), 14087–14092.
- [88] Savory, J. G.; Préfontaine, G. G.; Lamprecht, C.; Liao, M.; Walther, R. F.; Lefebvre, Y. A.; Haché, R. J. Glucocorticoid receptor homodimers and glucocorticoid-mineralocorticoid receptor heterodimers form in the cytoplasm through alternative dimerization interfaces. *Molecular and cellular biology* **2001**, 21 (3), 781–793.
- [89] Garlatti, M.; Daheshia, M.; Slater, E.; Bouguet, J.; Hanoune, J.; Beato, M.; Barouki, R. A functional glucocorticoid-responsive unit composed of two overlapping inactive receptor-binding sites: evidence for formation of a receptor tetramer. *Molecular and cellular biology* **1994**, 14 (12), 8007–8017.
- [90] Tsukamoto, T.; Demura, M.; Sudo, Y. Irreversible trimer to monomer transition of thermophilic rhodopsin upon thermal stimulation. *The Journal of Physical Chemistry B* **2014**, 118 (43), 12383–12394.
- [91] Perlmann, T.; Wrangé, O. Specific glucocorticoid receptor binding to DNA reconstituted in a nucleosome. *The EMBO Journal* **1988**, 7 (10), 3073–3079.
- [92] Perlmann, T. Glucocorticoid receptor DNA-binding specificity is increased by the organization of DNA in nucleosomes. *Proceedings of the National Academy of Sciences* **1992**, 89 (9), 3884–3888.
- [93] Perlmann, T.; Eriksson, P.; Wrangé, O. Quantitative analysis of the glucocorticoid receptor-DNA interaction at the mouse mammary tumor virus glucocorticoid response element. *Journal of Biological Chemistry* **1990**, 265 (28), 17222–17229.
- [94] Li, Q.; Wrangé, O. Translational positioning of a nucleosomal glucocorticoid response element modulates glucocorticoid receptor affinity. *Genes & development* **1993**, 7 (12a), 2471–2482.

- [95] Jin, J.; Lian, T.; Sunney Xie, X.; Su, X.-D. High-accuracy mapping of protein binding stability on nucleosomal DNA using a single-molecule method. *Journal of molecular cell biology* **2014**, 6 (5), 438–440.
- [96] Cosgrove, M. S. Histone proteomics and the epigenetic regulation of nucleosome mobility. *Expert review of proteomics* **2007**, 4 (4), 465–478.
- [97] Gansen, A.; Valeri, A.; Hauger, F.; Felekyan, S.; Kalinin, S.; Tóth, K.; Langowski, J.; Seidel, C. A. Nucleosome disassembly intermediates characterized by single-molecule FRET. *Proceedings of the National Academy of Sciences of the United States of America* **2009**, 106 (36), 15308–15313.
- [98] Poirier, M. G.; Oh, E.; Tims, H. S.; Widom, J. Dynamics and function of compact nucleosome arrays. *Nature Structural and Molecular Biology* **2009**, 16 (9), 938–944.
- [99] Grigoryev, S. A. Nucleosome spacing and chromatin higher-order folding. *Nucleus* **2012**, 3 (6), 493–499.
- [100] Luo, Y.; North, J. A.; Rose, S. D.; Poirier, M. G. Nucleosomes accelerate transcription factor dissociation. *Nucleic Acids Research* **2014**, 42 (5), 3017–3027.
- [101] Paul, M.; Murray, V. Use of an automated capillary DNA sequencer to investigate the interaction of cisplatin with telomeric DNA sequences. *Biomedical Chromatography* **2012**, 26 (3), 350–354.
- [102] Abe, K.; Zhao, L.; Periasamy, A.; Intes, X.; Barroso, M. Non-invasive in vivo imaging of near infrared-labeled transferrin in breast cancer cells and tumors using fluorescence lifetime FRET. *PloS one* **2013**, 8 (11), e80269.
- [103] Buning, R.; Van Noort, J. Single-pair FRET experiments on nucleosome conformational dynamics. *Enfermedades Infecciosas y Microbiologia Clinica* **2010**, 28 (SUPPL. 3), 1729–1740.
- [104] Buning, R.; Kropff, W.; Martens, K.; Van Noort, J. SpFRET reveals changes in nucleosome breathing by neighboring nucleosomes. *Journal of Physics Condensed Matter* **2015**, 27 (6), 64103.

-
- [105] Harriman, O.; Leake, M. Single molecule experimentation in biological physics: exploring the living component of soft condensed matter one molecule at a time. *Journal of Physics: Condensed Matter* **2011**, 23 (50), 503101.
- [106] Lenn, T.; Leake, M. C. Experimental approaches for addressing fundamental biological questions in living, functioning cells with single molecule precision. *Open biology* **2012**, 2 (6), 120090.
- [107] Leake, M. C. The physics of life: one molecule at a time, **2013**.
- [108] Miller, H.; Zhou, Z.; Shepherd, J.; Wollman, A. J.; Leake, M. C. Single-molecule techniques in biophysics: a review of the progress in methods and applications. *Reports on Progress in Physics* **2017**, 81 (2), 024601.
- [109] Sheppard, C. J.; Gu, M.; Roy, M. Signal-to-noise ratio in confocal microscope systems. *Journal of Microscopy* **1992**, 168 (3), 209–218.
- [110] Oldenbourg, R.; Terada, H.; Tiberio, R.; Inoue, S. Image sharpness and contrast transfer in coherent confocal microscopy. *Journal of microscopy* **1993**, 172 (1), 31–39.
- [111] Pawley, J. B. Limitations on optical sectioning in live-cell confocal microscopy. *Scanning: The Journal of Scanning Microscopies* **2002**, 24 (5), 241–246.
- [112] Schermelleh, L.; Heintzmann, R.; Leonhardt, H. A guide to super-resolution fluorescence microscopy. *Journal of Cell Biology* **2010**, 190 (2), 165–175.
- [113] Leung, B. O.; Chou, K. C. Review of super-resolution fluorescence microscopy for biology. *Applied spectroscopy* **2011**, 65 (9), 967–980.
- [114] Beljonne, D.; Curutchet, C.; Scholes, G. D.; Silbey, R. J. Beyond Förster resonance energy transfer in biological and nanoscale systems. *The journal of physical chemistry B* **2009**, 113 (19), 6583–6599.
- [115] Clegg, R. M. Förster resonance energy transfer—FRET what is it, why do it, and how it's done. *Laboratory techniques in biochemistry and molecular biology* **2009**, 33, 1–57.

- [116] Sahoo, H. Förster resonance energy transfer—A spectroscopic nanoruler: Principle and applications. *Journal of Photochemistry and Photobiology C: Photochemistry Reviews* **2011**, 12 (1), 20–30.
- [117] Zauner, T.; Berger-Hoffmann, R.; Müller, K.; Hoffmann, R.; Zuchner, T. Highly adaptable and sensitive protease assay based on fluorescence resonance energy transfer. *Analytical chemistry* **2011**, 83 (19), 7356–7363.
- [118] Thompson, N. L. Fluorescence correlation spectroscopy. In *Topics in fluorescence spectroscopy*, 337–378. Springer, **2002**.
- [119] Rigler, R.; Elson, E. S. Fluorescence correlation spectroscopy: theory and applications, volume 65. Springer Science & Business Media, **2012**.
- [120] Haustein, E.; Schwille, P. Fluorescence correlation spectroscopy: novel variations of an established technique. *Annu. Rev. Biophys. Biomol. Struct.* **2007**, 36, 151–169.
- [121] Hess, S. T.; Huang, S.; Heikal, A. A.; Webb, W. W. Biological and chemical applications of fluorescence correlation spectroscopy: a review. *Biochemistry* **2002**, 41 (3), 697–705.
- [122] Elson, E. L. Fluorescence correlation spectroscopy: past, present, future. *Biophysical journal* **2011**, 101 (12), 2855–2870.
- [123] Klehs, K.; Spahn, C.; Endesfelder, U.; Lee, S. F.; Fürstenberg, A.; Heilemann, M. Increasing the brightness of cyanine fluorophores for single-molecule and superresolution imaging. *ChemPhysChem* **2014**, 15 (4), 637–641.
- [124] Cooper, M.; Ebner, A.; Briggs, M.; Burrows, M.; Gardner, N.; Richardson, R.; West, R. Cy3B™: improving the performance of cyanine dyes. *Journal of fluorescence* **2004**, 14 (2), 145–150.
- [125] Ploetz, E.; Lerner, E.; Husada, F.; Roelfs, M.; Chung, S.; Hohlbein, J.; Weiss, S.; Cordes, T. Förster resonance energy transfer and protein-induced fluorescence enhancement as synergetic multi-scale molecular rulers. *Scientific reports* **2016**, 6 (1), 1–18.

-
- [126] Holden, S. J.; Uphoff, S.; Hohlbein, J.; Yadin, D.; Le Reste, L.; Britton, O. J.; Kapanidis, A. N. Defining the limits of single-molecule FRET resolution in TIRF microscopy. *Biophysical Journal* **2010**, 99 (9), 3102–3111.
- [127] Schwille, P.; Kummer, S.; Heikal, A. A.; Moerner, W.; Webb, W. W. Fluorescence correlation spectroscopy reveals fast optical excitation-driven intramolecular dynamics of yellow fluorescent proteins. *Proceedings of the National Academy of Sciences* **2000**, 97 (1), 151–156.
- [128] Kremers, G.-J.; Goedhart, J.; van Munster, E. B.; Gadella, T. W. Cyan and yellow super fluorescent proteins with improved brightness, protein folding, and FRET Förster radius. *Biochemistry* **2006**, 45 (21), 6570–6580.
- [129] Kubin, R. F.; Fletcher, A. N. Fluorescence quantum yields of some rhodamine dyes. *Journal of Luminescence* **1982**, 27 (4), 455–462.
- [130] Müller, B. K.; Reuter, A.; Simmel, F. C.; Lamb, D. C. Single-pair FRET characterization of DNA tweezers. *Nano letters* **2006**, 6 (12), 2814–2820.
- [131] Fields, A. P.; Cohen, A. E. Anti-Brownian traps for studies on single molecules. *Methods in enzymology* **2010**, 475, 149–174.
- [132] Prendergast, F. G.; Mann, K. G. Chemical and physical properties of aequorin and the green fluorescent protein isolated from *Aequorea forskalea*. *Biochemistry* **1978**, 17 (17), 3448–3453.
- [133] Ingargiola, A.; Lerner, E.; Chung, S. Y.; Weiss, S.; Michalet, X. FRET-Bursts: An open source toolkit for analysis of freely-diffusing Single-molecule FRET. *PLoS ONE* **2016**, 11 (8).
- [134] Laurence, T.; Fore, S.; Huser, T. A fast, flexible algorithm for calculating correlations in Fluorescence Correlation Spectroscopy. *Optics Letters* **2005**, 31 (6).
- [135] Chung, H. S.; Louis, J. M.; Eaton, W. A. Distinguishing between protein dynamics and dye photophysics in single-molecule FRET experiments. *Biophysical Journal* **2010**, 98 (4), 696–706.

- [136] Stennett, E. M.; Ciuba, M. A.; Levitus, M. Photophysical processes in single molecule organic fluorescent probes. *Chemical Society Reviews* **2014**, 43 (4), 1057–1075.
- [137] Müller, B. K.; Zaychikov, E.; Bräuchle, C.; Lamb, D. C. Pulsed interleaved excitation. *Biophysical journal* **2005**, 89 (5), 3508–3522.
- [138] Ries, J.; Petráek, Z.; García-Sáez, A. J.; Schwille, P. A comprehensive framework for fluorescence cross-correlation spectroscopy. *New Journal of Physics* **2010**, 12.
- [139] Bacia, K.; Petrášek, Z.; Schwille, P. Correcting for spectral cross-talk in dual-color fluorescence cross-correlation spectroscopy. *ChemPhysChem* **2012**, 13 (5), 1221–1231.
- [140] Foo, Y. H.; Naredi-Rainer, N.; Lamb, D. C.; Ahmed, S.; Wohland, T. Factors affecting the quantification of biomolecular interactions by fluorescence cross-correlation spectroscopy. *Biophysical journal* **2012**, 102 (5), 1174–1183.
- [141] Hendrix, J.; Lamb, D. C. Implementation and application of pulsed interleaved excitation for dual-color FCS and RICS. In *Fluorescence Spectroscopy and Microscopy*, 653–682. Springer, **2014**.
- [142] Schwille, P.; Meyer-Almes, F.-J.; Rigler, R. Dual-color fluorescence cross-correlation spectroscopy for multicomponent diffusional analysis in solution. *Biophysical journal* **1997**, 72 (4), 1878–1886.
- [143] Medina, M. A.; Schwille, P. Fluorescence correlation spectroscopy for the detection and study of single molecules in biology. *Bioessays* **2002**, 24 (8), 758–764.
- [144] Meseth, U.; Wohland, T.; Rigler, R.; Vogel, H. Resolution of fluorescence correlation measurements. *Biophysical journal* **1999**, 76 (3), 1619–1631.
- [145] Magde, D.; Elson, E.; Webb, W. W. Thermodynamic fluctuations in a reacting system—measurement by fluorescence correlation spectroscopy. *Physical review letters* **1972**, 29 (11), 705.

-
- [146] Poirier, M. G.; Bussiek, M.; Langowski, J.; Widom, J. Spontaneous access to DNA target sites in folded chromatin fibers. *Journal of molecular biology* **2008**, 379 (4), 772–786.
- [147] Culbertson, M. J.; Burden, D. L. A distributed algorithm for multi-tau autocorrelation. *Review of scientific instruments* **2007**, 78 (4), 044102.
- [148] Sint, D.; Raso, L.; Traugott, M. Advances in multiplex PCR: balancing primer efficiencies and improving detection success. *Methods in ecology and evolution* **2012**, 3 (5), 898–905.
- [149] Singh, C.; Roy-Chowdhuri, S. Quantitative real-time PCR: recent advances. *Clinical Applications of PCR* **2016**, 161–176.
- [150] Zahiri, J.; Hannon Bozorgmehr, J.; Masoudi-Nejad, A. Computational prediction of protein–protein interaction networks: algorithms and resources. *Current genomics* **2013**, 14 (6), 397–414.
- [151] Angermueller, C.; Pärnamaa, T.; Parts, L.; Stegle, O. Deep learning for computational biology. *Molecular systems biology* **2016**, 12 (7), 878.
- [152] Regmi, R.; Al Balushi, A. A.; Rigneault, H.; Gordon, R.; Wenger, J. Nanoscale volume confinement and fluorescence enhancement with double nanohole aperture. *Scientific reports* **2015**, 5 (1), 1–10.
- [153] Kuang, C.; Liu, Y.; Hao, X.; Luo, D.; Liu, X. Creating attoliter detection volume by microsphere photonic nanojet and fluorescence depletion. *Optics Communications* **2012**, 285 (4), 402–406.
- [154] Estrada, L. C.; Aramendía, P. F.; Martínez, O. E. 10000 times volume reduction for fluorescence correlation spectroscopy using nano-antennas. *Optics express* **2008**, 16 (25), 20597–20602.
- [155] Zheng, Y.; Nguyen, J.; Wei, Y.; Sun, Y. Recent advances in microfluidic techniques for single-cell biophysical characterization. *Lab on a Chip* **2013**, 13 (13), 2464–2483.
- [156] Larkin, J. E.; Frank, B. C.; Gavras, H.; Sultana, R.; Quackenbush, J. Independence and reproducibility across microarray platforms. *Nature methods* **2005**, 2 (5), 337–344.

- [157] Baker, M. Reproducibility crisis. *Nature* **2016**, 533 (26), 353–66.
- [158] Iqbal, S. A.; Wallach, J. D.; Khoury, M. J.; Schully, S. D.; Ioannidis, J. P. Reproducible research practices and transparency across the biomedical literature. *PLoS biology* **2016**, 14 (1), e1002333.
- [159] Petersen, E. J.; Hirsch, C.; Elliott, J. T.; Krug, H. F.; Aengenheister, L.; Arif, A. T.; Bogni, A.; Kinsner-Ovaskainen, A.; May, S.; Walser, T.; et al. Cause-and-effect analysis as a tool to improve the reproducibility of nanobioassays: four case studies. *Chemical research in toxicology* **2019**, 33 (5), 1039–1054.
- [160] Elofsson, A.; Hess, B.; Lindahl, E.; Onufriev, A.; Van der Spoel, D.; Wallqvist, A. Ten simple rules on how to create open access and reproducible molecular simulations of biological systems, **2019**.
- [161] Bustin, S. A.; Wittwer, C. T. MIQE: a step toward more robust and reproducible quantitative PCR. *Clinical chemistry* **2017**, 63 (9), 1537–1538.
- [162] De Marco, A. Nanomaterial bio-activation and macromolecules functionalization: the search for reliable protocols. *Protein expression and purification* **2018**, 147, 49–54.
- [163] Di Vito, A.; Reitano, E.; Poggi, L.; Iaboni, M. Biotin oligonucleotide labeling reactions: A method to assess their effectiveness and reproducibility. *Analytical biochemistry* **2020**, 593, 113590.
- [164] Teixeira da Silva, J. A. Room temperature in scientific protocols and experiments should be defined: a reproducibility issue, **2021**.
- [165] Rychlik, W.; Spencer, W.; Rhoads, R. Optimization of the annealing temperature for DNA amplification in vitro. *Nucleic acids research* **1990**, 18 (21), 6409–6412.
- [166] Stadhouders, R.; Pas, S. D.; Anber, J.; Voermans, J.; Mes, T. H.; Schutten, M. The effect of primer-template mismatches on the detection and quantification of nucleic acids using the 5′nuclease assay. *The Journal of Molecular Diagnostics* **2010**, 12 (1), 109–117.

-
- [167] Frey, U. H.; Bachmann, H. S.; Peters, J.; Siffert, W. PCR-amplification of GC-rich regions: 'slowdown PCR'. *Nature protocols* **2008**, 3 (8), 1312–1317.
- [168] Lis, J. T.; Schleif, R. Size fractionation of double-stranded DNA by precipitation with polyethylene glycol. *Nucleic acids research* **1975**, 2 (3), 383–390.
- [169] Cheng, C.; Jia, J.-L.; Ran, S.-Y. Polyethylene glycol and divalent salt-induced DNA re-entrant condensation revealed by single molecule measurements. *Soft Matter* **2015**, 11 (19), 3927–3935.
- [170] Borah, P. Primer designing for PCR. *Science Vision* **2011**, 11 (3), 134–136.
- [171] Kaczmarczyk, A.; Brouwer, T. B.; Pham, C.; Dekker, N. H.; Noort, J. v. Probing chromatin structure with magnetic tweezers. In *Nanoscale Imaging*, 297–323. Springer, **2018**.
- [172] Koopmans, W. J.; Brehm, A.; Logie, C.; Schmidt, T.; Van Noort, J. Single-pair FRET microscopy reveals mononucleosome dynamics. *Journal of Fluorescence* **2007**, 17 (6), 785–795.
- [173] Böhm, V.; Hieb, A. R.; Andrews, A. J.; Gansen, A.; Rocker, A.; Tóth, K.; Luger, K.; Langowski, J. Nucleosome accessibility governed by the dimer/tetramer interface. *Nucleic Acids Research* **2011**, 39 (8), 3093–3102.
- [174] North, J. A.; Shimko, J. C.; Javaid, S.; Mooney, A. M.; Shoffner, M. A.; Rose, S. D.; Bundschuh, R.; Fishel, R.; Ottesen, J. J.; Poirier, M. G. Regulation of the nucleosome unwrapping rate controls DNA accessibility. *Nucleic Acids Research* **2012**, 40 (20), 10215–10227.
- [175] Schiessel, H. The nucleosome: a transparent, slippery, sticky and yet stable DNA-protein complex. *The European Physical Journal E* **2006**, 19 (3), 251–262.
- [176] Koopmans, W. J.; Schmidt, T.; van Noort, J. Nucleosome Immobilization Strategies for Single-Pair FRET Microscopy. *ChemPhysChem* **2008**, 9 (14), 2002–2009.

- [177] Kelbauskas, L.; Sun, J.; Woodbury, N.; Lohr, D. Nucleosomal stability and dynamics vary significantly when viewed by internal versus terminal labels. *Biochemistry* **2008**, 47 (36), 9627–9635.
- [178] Gansen, A.; Tóth, K.; Schwarz, N.; Langowski, J. Structural variability of nucleosomes detected by single-pair Förster resonance energy transfer: Histone acetylation, sequence variation, and salt effects. *Journal of Physical Chemistry B* **2009**, 113 (9), 2604–2613.
- [179] Van Holde, K.; Zlatanova, A. G., J.; Moudrianakis, E. Elements of chromatin structure: histones, nucleosome, and fibres. *Chromatin Structure and Gene Expression* **1995**, 1–26.
- [180] Szerlong, H. J.; Hansen, J. C. Nucleosome distribution and linker DNA: Connecting nuclear function to dynamic chromatin structure, **2011**.
- [181] Li, Q.; Wrangé, O. Accessibility of a glucocorticoid response element in a nucleosome depends on its rotational positioning. *Molecular and Cellular Biology* **1995**, 15 (8), 4375–4384.
- [182] Lone, I. N.; Shukla, M. S.; Charles Richard, J. L.; Peshev, Z. Y.; Dimitrov, S.; Angelov, D. Binding of NF- κ B to Nucleosomes: Effect of Translational Positioning, Nucleosome Remodeling and Linker Histone H1. *PLoS Genetics* **2013**, 9 (9).
- [183] Reul, J.; Kloet, E. D. Two receptor systems for corticosterone in rat brain: microdistribution and differential occupation. *Endocrinology* **1985**, 117 (6), 2505–2511.
- [184] Htun, H.; Barsony, J.; Renyi, I.; Gould, D. L.; Hager, G. L. Visualization of glucocorticoid receptor translocation and intranuclear organization in living cells with a green fluorescent protein chimera. *Proceedings of the National Academy of Sciences of the United States of America* **1996**, 93 (10), 4845–4850.
- [185] Schiller, B. J.; Chodankar, R.; Watson, L. C.; Stallcup, M. R.; Yamamoto, K. R. Glucocorticoid receptor binds half sites as a monomer and regulates specific target genes. *Genome biology* **2014**, 15 (8), 418.

-
- [186] Schoneveld, O. J.; Gaemers, I. C.; Lamers, W. H. Mechanisms of glucocorticoid signalling. *Biochimica et Biophysica Acta (BBA)-Gene Structure and Expression* **2004**, 1680 (2), 114–128.
- [187] Dahlman-Wright, K.; Wright, A.; Gustafsson, J.-A.; Carlstedt-Duke, J. Interaction of the glucocorticoid receptor DNA-binding domain with DNA as a dimer is mediated by a short segment of five amino acids. *Journal of Biological Chemistry* **1991**, 266 (5), 3107–3112.
- [188] Datson, N.; Polman, J.; De Jonge, R.; Van Boheemen, P.; Van Maanen, E.; Welten, J.; McEwen, B.; Meiland, H.; Meijer, O. Specific regulatory motifs predict glucocorticoid responsiveness of hippocampal gene expression. *Endocrinology* **2011**, 152 (10), 3749–3757.
- [189] Kelbauskas, L.; Chan, N.; Bash, R.; Yodh, J.; Woodbury, N.; Lohr, D. Sequence-dependent nucleosome structure and stability variations detected by Förster resonance energy transfer. *Biochemistry* **2007**, 46 (8), 2239–2248.
- [190] Flaus, A.; Richmond, T. J. Positioning and stability of nucleosomes on MMTV 3'LTR sequences. *Journal of molecular biology* **1998**, 275 (3), 427–441.
- [191] Anderson, J.; Widom, J. Sequence and position-dependence of the equilibrium accessibility of nucleosomal DNA target sites. *Journal of molecular biology* **2000**, 296 (4), 979–987.
- [192] Sharma, S.; Dokholyan, N. V. DNA sequence mediates nucleosome structure and stability. *Biophysical Journal* **2008**, 94 (1), 1–3.
- [193] Jiang, C.; Pugh, B. F. A compiled and systematic reference map of nucleosome positions across the *Saccharomyces cerevisiae* genome. *Genome Biology* **2009**, 10 (10), 1–11.
- [194] MacIsaac, K. D.; Wang, T.; Gordon, D. B.; Gifford, D. K.; Stormo, G. D.; Fraenkel, E. An improved map of conserved regulatory sites for *Saccharomyces cerevisiae*. *BMC Bioinformatics* **2006**, 7, 1–14.
- [195] Lin, Y.-S.; Carey, M. F.; Ptashne, M.; Green, M. R. GAL4 derivatives function alone and synergistically with mammalian activators in vitro. *Cell* **1988**, 54 (5), 659–664.

- [196] Record Jr, M. T.; Lohman, T. M.; De Haseth, P. Ion effects on ligand-nucleic acid interactions. *Journal of molecular biology* **1976**, 107 (2), 145–158.
- [197] Krichevsky, O.; Bonnet, G. Fluorescence correlation spectroscopy: the technique and its applications. *Reports on Progress in Physics* **2002**, 65 (2), 251.
- [198] Torres, T.; Levitus, M. Measuring conformational dynamics: A new FCS-FRET approach. *Journal of Physical Chemistry B* **2007**, 111 (25), 7392–7400.
- [199] Tims, H. S.; Gurunathan, K.; Levitus, M.; Widom, J. Dynamics of nucleosome invasion by DNA binding proteins. *Journal of molecular biology* **2011**, 411 (2), 430–448.
- [200] Lee, N. K.; Kapanidis, A. N.; Wang, Y.; Michalet, X.; Mukhopadhyay, J.; Ebright, R. H.; Weiss, S. Accurate FRET measurements within single diffusing biomolecules using alternating-laser excitation. *Biophysical journal* **2005**, 88 (4), 2939–2953.
- [201] Hazan, N. P.; Tomov, T. E.; Tsukanov, R.; Liber, M.; Berger, Y.; Masoud, R.; Toth, K.; Langowski, J.; Nir, E. Nucleosome core particle disassembly and assembly kinetics studied using single-molecule fluorescence. *Biophysical journal* **2015**, 109 (8), 1676–1685.
- [202] Gansen, A.; Felekyan, S.; Kühnemuth, R.; Lehmann, K.; Tóth, K.; Seidel, C. A.; Langowski, J. High precision FRET studies reveal reversible transitions in nucleosomes between microseconds and minutes. *Nature Communications* **2018**, 9 (1), 1–13.
- [203] Gibson, M. D.; Gatchalian, J.; Slater, A.; Kutateladze, T. G.; Poirier, M. G. PHF1 Tudor and N-terminal domains synergistically target partially unwrapped nucleosomes to increase DNA accessibility. *Nucleic acids research* **2017**, 45 (7), 3767–3776.
- [204] Bowman, G. D.; Poirier, M. G. Post-translational modifications of histones that influence nucleosome dynamics. *Chemical reviews* **2014**, 115 (6), 2274–2295.

-
- [205] Rothbart, S. B.; Strahl, B. D. Interpreting the language of histone and DNA modifications. *Biochimica et Biophysica Acta (BBA)-Gene Regulatory Mechanisms* **2014**, 1839 (8), 627–643.
- [206] Bannister, A. J.; Kouzarides, T. Regulation of chromatin by histone modifications. *Cell research* **2011**, 21 (3), 381–395.
- [207] Cosgrove, M. S.; Boeke, J. D.; Wolberger, C. Regulated nucleosome mobility and the histone code. *Nature structural & molecular biology* **2004**, 11 (11), 1037–1043.
- [208] Mersfelder, E. L.; Parthun, M. R. The tale beyond the tail: histone core domain modifications and the regulation of chromatin structure. *Nucleic acids research* **2006**, 34 (9), 2653–2662.
- [209] Kingston, R. E.; Narlikar, G. J. ATP-dependent remodeling and acetylation as regulators of chromatin fluidity. *Genes & development* **1999**, 13 (18), 2339–2352.
- [210] Saha, A.; Wittmeyer, J.; Cairns, B. R. Chromatin remodelling: the industrial revolution of DNA around histones. *Nature reviews Molecular cell biology* **2006**, 7 (6), 437–447.
- [211] Bowerman, S.; Wereszczynski, J. Effects of macroH2A and H2A.Z on nucleosome dynamics as elucidated by molecular dynamics simulations. *Biophysical journal* **2016**, 110 (2), 327–337.
- [212] Xiao, X.; Liu, C.; Pei, Y.; Wang, Y.-Z.; Kong, J.; Lu, K.; Ma, L.; Dou, S.-X.; Wang, P.-Y.; Li, G.; et al. Histone H2A ubiquitination reinforces mechanical stability and asymmetry at the single-nucleosome level. *Journal of the American Chemical Society* **2020**, 142 (7), 3340–3345.
- [213] Zentner, G. E.; Henikoff, S. Regulation of nucleosome dynamics by histone modifications. *Nature structural & molecular biology* **2013**, 20 (3), 259–266.
- [214] Tessarz, P.; Kouzarides, T. Histone core modifications regulating nucleosome structure and dynamics. *Nature reviews Molecular cell biology* **2014**, 15 (11), 703–708.

- [215] Mutskov, V.; Gerber, D.; Angelov, D.; Ausio, J.; Workman, J.; Dimitrov, S. Persistent interactions of core histone tails with nucleosomal DNA following acetylation and transcription factor binding. *Molecular and cellular biology* **1998**, 18 (11), 6293–6304.
- [216] Polach, K.; Lowary, P.; Widom, J. Effects of core histone tail domains on the equilibrium constants for dynamic DNA site accessibility in nucleosomes. *Journal of molecular biology* **2000**, 298 (2), 211–223.
- [217] Neumann, H.; Hancock, S. M.; Buning, R.; Routh, A.; Chapman, L.; Somers, J.; Owen-Hughes, T.; van Noort, J.; Rhodes, D.; Chin, J. W. A method for genetically installing site-specific acetylation in recombinant histones defines the effects of H3 K56 acetylation. *Molecular cell* **2009**, 36 (1), 153–163.
- [218] Levenson, J.; Wood, M. 4.42 - Epigenetics – Chromatin Structure and Rett Syndrome. *Learning and Memory: A Comprehensive Reference* **2008**, 859–878.
- [219] Sun, Z.; Zhang, Y.; Jia, J.; Fang, Y.; Tang, Y.; Wu, H.; Fang, D. H3K36me3, message from chromatin to DNA damage repair. *Cell & bioscience* **2020**, 10 (1), 1–9.
- [220] Tesina, P.; Čermáková, K.; Hořejší, M.; Procházková, K.; Fábry, M.; Sharma, S.; Christ, F.; Demeulemeester, J.; Debyser, Z.; De Rijck, J.; et al. Multiple cellular proteins interact with LEDGF/p75 through a conserved unstructured consensus motif. *Nature communications* **2015**, 6 (1), 1–14.
- [221] Eidahl, J. O.; Crowe, B. L.; North, J. A.; McKee, C. J.; Shkriabai, N.; Feng, L.; Plumb, M.; Graham, R. L.; Gorelick, R. J.; Hess, S.; et al. Structural basis for high-affinity binding of LEDGF PWWP to mononucleosomes. *Nucleic acids research* **2013**, 41 (6), 3924–3936.
- [222] Turlure, F.; Maertens, G.; Rahman, S.; Cherepanov, P.; Engelman, A. A tripartite DNA-binding element, comprised of the nuclear localization signal and two AT-hook motifs, mediates the association of LEDGF/p75 with chromatin in vivo. *Nucleic acids research* **2006**, 34 (5), 1653–1665.

-
- [223] Llano, M.; Vanegas, M.; Hutchins, N.; Thompson, D.; Delgado, S.; Poeschla, E. M. Identification and characterization of the chromatin-binding domains of the HIV-1 integrase interactor LEDGF/p75. *Journal of molecular biology* **2006**, 360 (4), 760–773.
- [224] McNeely, M.; Hendrix, J.; Busschots, K.; Boons, E.; Deleersnijder, A.; Gerard, M.; Christ, F.; Debyser, Z. In vitro DNA tethering of HIV-1 integrase by the transcriptional coactivator LEDGF/p75. *Journal of molecular biology* **2011**, 410 (5), 811–830.
- [225] Bartholomeeusen, K.; De Rijck, J.; Busschots, K.; Desender, L.; Gijssbers, R.; Emiliani, S.; Benarous, R.; Debyser, Z.; Christ, F. Differential interaction of HIV-1 integrase and Jpo2 with the C terminus of LEDGF/p75. *Journal of molecular biology* **2007**, 372 (2), 407–421.
- [226] Caselli, M.; Latterini, L.; Ponterini, G. Consequences of H-dimerization on the photophysics and photochemistry of oxacarbocyanines. *Physical Chemistry Chemical Physics* **2004**, 6 (14), 3857–3863.
- [227] Liu, Y.; Feshitan, J. A.; Wei, M.-Y.; Borden, M. A.; Yuan, B. Ultrasound-modulated fluorescence based on donor-acceptor-labeled microbubbles. *Journal of biomedical optics* **2015**, 20 (3), 036012.
- [228] Holzmeister, P.; Wunsch, B.; Gietl, A.; Tinnefeld, P. Single-molecule photophysics of dark quenchers as non-fluorescent FRET acceptors. *Photochemical & Photobiological Sciences* **2014**, 13 (6), 853–858.
- [229] Morrison, E. A.; Baweja, L.; Poirier, M. G.; Wereszczynski, J.; Musselman, C. A. Nucleosome composition regulates the histone H3 tail conformational ensemble and accessibility. *Nucleic acids research* **2021**, 49 (8), 4750–4767.
- [230] Ghoneim, M.; Fuchs, H. A.; Musselman, C. A. Histone tail conformations: a fuzzy affair with DNA. *Trends in Biochemical Sciences* **2021**.
- [231] Pan, Y.; Tsai, C.-J.; Ma, B.; Nussinov, R. Mechanisms of transcription factor selectivity. *Trends in Genetics* **2010**, 26 (2), 75–83.
- [232] Zaret, K. S.; Lerner, J.; Iwafuchi-Doi, M. Chromatin scanning by dynamic binding of pioneer factors. *Molecular cell* **2016**, 62 (5), 665–667.

- [233] Sung, M.-H.; Guertin, M. J.; Baek, S.; Hager, G. L. DNase footprint signatures are dictated by factor dynamics and DNA sequence. *Molecular cell* **2014**, 56 (2), 275–285.
- [234] Groeneweg, F. L.; van Royen, M. E.; Fenz, S.; Keizer, V. I.; Geverts, B.; Prins, J.; de Kloet, E. R.; Houtsmuller, A. B.; Schmidt, T. S.; Schaaf, M. J. Quantitation of glucocorticoid receptor DNA-binding dynamics by single-molecule microscopy and FRAP. *PLoS one* **2014**, 9 (3), e90532.
- [235] Stormo, G. D.; Zhao, Y. Determining the specificity of protein–DNA interactions. *Nature Reviews Genetics* **2010**, 11 (11), 751–760.
- [236] Lin, M.; Guo, J.-t. New insights into protein–DNA binding specificity from hydrogen bond based comparative study. *Nucleic acids research* **2019**, 47 (21), 11103–11113.
- [237] Schreiber, G.; Keating, A. E. Protein binding specificity versus promiscuity. *Current opinion in structural biology* **2011**, 21 (1), 50–61.
- [238] Greenspan, N. S. Cohen’s Conjecture, Howard’s Hypothesis, and Ptashne’s Ptruth: an exploration of the relationship between affinity and specificity. *Trends in immunology* **2010**, 31 (4), 138–143.
- [239] Corona, R. I.; Guo, J.-t. Statistical analysis of structural determinants for protein–DNA-binding specificity. *Proteins: Structure, Function, and Bioinformatics* **2016**, 84 (8), 1147–1161.
- [240] Bakiri, L.; Matsuo, K.; Wisniewska, M.; Wagner, E. F.; Yaniv, M. Promoter specificity and biological activity of tethered AP-1 dimers. *Molecular and cellular biology* **2002**, 22 (13), 4952–4964.
- [241] Hess, J.; Angel, P.; Schorpp-Kistner, M. AP-1 subunits: quarrel and harmony among siblings. *Journal of cell science* **2004**, 117 (25), 5965–5973.
- [242] Bohmann, D.; Bos, T. J.; Admon, A.; Nishimura, T.; Vogt, P. K.; Tjian, R. Human proto-oncogene c-jun encodes a DNA binding protein with structural and functional properties of transcription factor AP-1. *Science* **1987**, 238 (4832), 1386–1392.

-
- [243] Karin, M.; Liu, Z.-g.; Zandi, E. AP-1 function and regulation. *Current opinion in cell biology* **1997**, 9 (2), 240–246.
- [244] Biddie, S. C.; John, S.; Sabo, P. J.; Thurman, R. E.; Johnson, T. A.; Schiltz, R. L.; Miranda, T. B.; Sung, M.-H.; Trump, S.; Lightman, S. L.; et al. Transcription factor AP1 potentiates chromatin accessibility and glucocorticoid receptor binding. *Molecular cell* **2011**, 43 (1), 145–155.
- [245] Rishi, V.; Bhattacharya, P.; Chatterjee, R.; Rozenberg, J.; Zhao, J.; Glass, K.; Fitzgerald, P.; Vinson, C. CpG methylation of half-CRE sequences creates C/EBP α binding sites that activate some tissue-specific genes. *Proceedings of the National Academy of Sciences* **2010**, 107 (47), 20311–20316.
- [246] Gustems, M.; Woellmer, A.; Rothbauer, U.; Eck, S. H.; Wieland, T.; Lutter, D.; Hammerschmidt, W. c-Jun/c-Fos heterodimers regulate cellular genes via a newly identified class of methylated DNA sequence motifs. *Nucleic acids research* **2014**, 42 (5), 3059–3072.
- [247] John, M.; Leppik, R.; Busch, S. J.; Granger-Schnarr, M.; Schnarr, M. DNA binding of Jun and Fos bZip domains: homodimers and heterodimers induce a DNA conformational change in solution. *Nucleic acids research* **1996**, 24 (22), 4487–4494.
- [248] Abate, C.; Luk, D.; Gentz, R.; Rauscher, F. J.; Curran, T. Expression and purification of the leucine zipper and DNA-binding domains of Fos and Jun: both Fos and Jun contact DNA directly. *Proceedings of the National Academy of Sciences* **1990**, 87 (3), 1032–1036.
- [249] Nakabeppu, Y.; Ryder, K.; Nathans, D. DNA binding activities of three murine Jun proteins: stimulation by Fos. *Cell* **1988**, 55 (5), 907–915.
- [250] Halazonetis, T. D.; Georgopoulos, K.; Greenberg, M. E.; Leder, P. c-Jun dimerizes with itself and with c-Fos, forming complexes of different DNA binding affinities. *Cell* **1988**, 55 (5), 917–924.
- [251] Ryseck, R.-P.; Bravo, R. c-JUN, JUN B, and JUN D differ in their binding affinities to AP-1 and CRE consensus sequences: effect of FOS proteins. *Oncogene* **1991**, 6 (4), 533–542.

- [252] Rauscher, F. d.; Voulalas, P. J.; Franza, B.; Curran, T. Fos and Jun bind cooperatively to the AP-1 site: reconstitution in vitro. *Genes & development* **1988**, 2 (12b), 1687–1699.
- [253] Eferl, R.; Wagner, E. F. AP-1: a double-edged sword in tumorigenesis. *Nature Reviews Cancer* **2003**, 3 (11), 859–868.
- [254] Yoon, H.; Kim, M.; Jang, K.; Shin, M.; Besser, A.; Xiao, X.; Zhao, D.; Wander, S. A.; Briegel, K.; Morey, L.; et al. p27 transcriptionally coregulates cJun to drive programs of tumor progression. *Proceedings of the National Academy of Sciences* **2019**, 116 (14), 7005–7014.
- [255] Brennan, A.; Leech, J. T.; Kad, N. M.; Mason, J. M. Selective antagonism of cJun for cancer therapy. *Journal of Experimental & Clinical Cancer Research* **2020**, 39 (1), 1–16.
- [256] Risse, G.; Jooss, K.; Neuberg, M.; Brüller, H.; Müller, R. Asymmetrical recognition of the palindromic AP1 binding site (TRE) by Fos protein complexes. *The EMBO journal* **1989**, 8 (12), 3825–3832.
- [257] Chinenov, Y.; Kerppola, T. K. Close encounters of many kinds: Fos-Jun interactions that mediate transcription regulatory specificity. *Oncogene* **2001**, 20 (19), 2438–2452.
- [258] Schaaf, M. J.; Lewis-Tuffin, L. J.; Cidlowski, J. A. Ligand-selective targeting of the glucocorticoid receptor to nuclear subdomains is associated with decreased receptor mobility. *Molecular Endocrinology* **2005**, 19 (6), 1501–1515.
- [259] Picard, D.; Yamamoto, K. R. Two signals mediate hormone-dependent nuclear localization of the glucocorticoid receptor. *The EMBO journal* **1987**, 6 (11), 3333–3340.
- [260] Schoenmakers, E.; ALEN, P.; Verrijdt, G.; PEETERS, B.; Verhoeven, G.; Rombauts, W.; Claessens, F. Differential DNA binding by the androgen and glucocorticoid receptors involves the second Zn-finger and a C-terminal extension of the DNA-binding domains. *Biochemical Journal* **1999**, 341 (3), 515–521.
- [261] Elbi, C.; Walker, D. A.; Romero, G.; Sullivan, W. P.; Toft, D. O.; Hager, G. L.; DeFranco, D. B. Molecular chaperones function as steroid

-
- receptor nuclear mobility factors. *Proceedings of the National Academy of Sciences* **2004**, 101 (9), 2876–2881.
- [262] Ratman, D.; Berghe, W. V.; Dejager, L.; Libert, C.; Tavernier, J.; Beck, I. M.; De Bosscher, K. How glucocorticoid receptors modulate the activity of other transcription factors: a scope beyond tethering. *Molecular and cellular endocrinology* **2013**, 380 (1-2), 41–54.
- [263] Voss, T. C.; Schiltz, R. L.; Sung, M.-H.; Yen, P. M.; Stamatoyannopoulos, J. A.; Biddie, S. C.; Johnson, T. A.; Miranda, T. B.; John, S.; Hager, G. L. Dynamic exchange at regulatory elements during chromatin remodeling underlies assisted loading mechanism. *Cell* **2011**, 146 (4), 544–554.
- [264] King, H. A.; Trotter, K. W.; Archer, T. K. Chromatin remodeling during glucocorticoid receptor regulated transactivation. *Biochimica et Biophysica Acta (BBA)-Gene Regulatory Mechanisms* **2012**, 1819 (7), 716–726.
- [265] Keizer, V. I.; Coppola, S.; Houtsmuller, A. B.; Geverts, B.; van Royen, M. E.; Schmidt, T.; Schaaf, M. J. Repetitive switching between DNA-binding modes enables target finding by the glucocorticoid receptor. *Journal of cell science* **2019**, 132 (5).
- [266] Chen, C.; Bundschuh, R. Quantitative models for accelerated protein dissociation from nucleosomal DNA. *Nucleic acids research* **2014**, 42 (15), 9753–9760.
- [267] Schaaf, M. J.; Cidlowski, J. A. Molecular determinants of glucocorticoid receptor mobility in living cells: the importance of ligand affinity. *Molecular and cellular biology* **2003**, 23 (6), 1922–1934.
- [268] Eriksson, P.; Daneholt, B.; Wrangé, Ö. The glucocorticoid receptor in homodimeric and monomeric form visualised by electron microscopy. *Journal of structural biology* **1991**, 107 (1), 48–55.
- [269] Cairns, W.; Cairns, C.; Pongratz, I.; Poellinger, L.; Okret, S. Assembly of a glucocorticoid receptor complex prior to DNA binding enhances its specific interaction with a glucocorticoid response element. *Journal of Biological Chemistry* **1991**, 266 (17), 11221–11226.

- [270] Hu, T.; Grosberg, A. Y.; Shklovskii, B. How proteins search for their specific sites on DNA: the role of DNA conformation. *Biophysical journal* **2006**, 90 (8), 2731–2744.
- [271] Eriksson, M.; Härd, T.; Nilsson, L. Molecular dynamics simulations of the glucocorticoid receptor DNA-binding domain in complex with DNA and free in solution. *Biophysical journal* **1995**, 68 (2), 402–426.
- [272] Halford, S. E.; Marko, J. F. How do site-specific DNA-binding proteins find their targets? *Nucleic acids research* **2004**, 32 (10), 3040–3052.
- [273] Murugan, R. Theory of site-specific DNA-protein interactions in the presence of conformational fluctuations of DNA binding domains. *Biophysical Journal* **2010**, 99 (2), 353–359.
- [274] Swinstead, E. E.; Miranda, T. B.; Paakinaho, V.; Baek, S.; Goldstein, I.; Hawkins, M.; Karpova, T. S.; Ball, D.; Mazza, D.; Lavis, L. D.; et al. Steroid receptors reprogram FoxA1 occupancy through dynamic chromatin transitions. *Cell* **2016**, 165 (3), 593–605.
- [275] Zhou, H.-X.; Szabo, A. Enhancement of association rates by non-specific binding to DNA and cell membranes. *Physical review letters* **2004**, 93 (17), 178101.
- [276] Klenin, K. V.; Merlitz, H.; Langowski, J.; Wu, C.-X. Facilitated diffusion of DNA-binding proteins. *Physical review letters* **2006**, 96 (1), 018104.
- [277] Elcock, A. H. Models of macromolecular crowding effects and the need for quantitative comparisons with experiment. *Current opinion in structural biology* **2010**, 20 (2), 196–206.
- [278] Gomez, D.; Klumpp, S. Biochemical reactions in crowded environments: revisiting the effects of volume exclusion with simulations. *Frontiers in Physics* **2015**, 3, 45.
- [279] Mirny, L.; Slutsky, M.; Wunderlich, Z.; Tafvizi, A.; Leith, J.; Kosmrlj, A. How a protein searches for its site on DNA: the mechanism of facilitated diffusion. *Journal of Physics A: Mathematical and Theoretical* **2009**, 42 (43), 434013.

-
- [280] Bancaud, A.; Huet, S.; Daigle, N.; Mozziconacci, J.; Beaudouin, J.; Ellenberg, J. Molecular crowding affects diffusion and binding of nuclear proteins in heterochromatin and reveals the fractal organization of chromatin. *The EMBO journal* **2009**, 28 (24), 3785–3798.
- [281] Ellis, R. J. Macromolecular crowding: obvious but underappreciated. *Trends in biochemical sciences* **2001**, 26 (10), 597–604.
- [282] Richter, K.; Nessling, M.; Lichter, P. Macromolecular crowding and its potential impact on nuclear function. *Biochimica et Biophysica Acta (BBA)-Molecular Cell Research* **2008**, 1783 (11), 2100–2107.
- [283] Akabayov, B.; Akabayov, S. R.; Lee, S.-J.; Wagner, G.; Richardson, C. C. Impact of macromolecular crowding on DNA replication. *Nature communications* **2013**, 4 (1), 1–10.

Samenvatting

Nucleosomen zijn het eerste niveau van DNA compactie in de kern van eukaryote cellen. In menselijke cellen wordt op deze manier ongeveer twee meter DNA gecondenseerd tot een bol met een diameter van zes micrometer. Hoewel het zich in deze sterk gecondenseerde staat bevindt, die chromatine wordt genoemd, is het DNA in chromatine betrokken bij processen zoals transcriptie en DNA-reparatie, en moet het DNA hiervoor toegankelijk zijn. Hiervoor wordt de structuur van chromatine gemoduleerd door histonstaartmodificaties, eiwitherkenningselementen in de DNA-sequentie en een groot aantal eiwit-DNA interacties. Eerdergenoemde processen hebben vaak directe DNA-toegang nodig en zijn daarvoor afhankelijk van een verandering in de nucleosoom compactie. In dit proefschrift beschrijf ik de resultaten van Pulsed Interleaved Excitation and Fluorescence (Cross) Correlation Spectroscopy (PIE-F(C)CS) gecombineerd met single-pair Förster Resonance Energy Transfer (spFRET) gebruikt om dynamiek en stabiliteit van enkele nucleosomen te bestuderen, welke afhangt van subtiele verschillen in de lengte van DNA uiteinden, DNA-sequentie, histonvarianten en specifieke en niet-specifieke eiwitinteracties. Deze techniek kan conformatieveranderingen van enkele nanometers meten, en is een uitstekende techniek om nucleosomale compactie te volgen, aangezien het nucleosoom slechts tien nanometer in diameter is. In combinatie met F(C)CS en PIE, is het mogelijk om met spFRET de conformatie veranderingen op een tijdschaal van micro- tot milliseconden te volgen.

Hoofdstuk 1 geeft een overzicht van eerdere studies van het nucleosoom, zijn rol in chromatine compactie *in vitro* en *in vivo* en de effecten van DNA-sequentie, histonmodificaties en eiwitinteracties op de stabiliteit en dynamiek van nucleosomen. Studies tonen een dubbele rol voor het nucleosoom; als stabiele structuur die herkend wordt door transcriptiefactoren die selectief binden aan specifieke histonmodificaties of DNA sequenties, en een dynamische entiteit die in staat is om DNA tijdelijk los te laten waardoor processen op het DNA kunnen worden gereguleerd. Dit alles gebeurt terwijl DNA in de cellen zit gevouwen op een schijnbaar ongeorganiseerde manier. In **Hoofdstukken 2 en 3** gaan we dieper in op de optische, analytische

en biologische hulpmiddelen die we hebben ontwikkeld en gebruikt om experimenten uit te voeren die gevoelig genoeg zijn om conformatie veranderingen in een enkel nucleosoom zichtbaar te maken. In **Hoofdstuk 2** beschrijven we de microscoop opstelling en het analyseproces voor experimenten met één molecuul. Het kwantificeren van de fluorofoorignalen in de microscoopopstelling en het optimaliseren van de uitlijning van de opstelling levert correlatiecurven van verschillende fluorescente signalen. De productie, zuivering en verwerking van DNA, nucleosomen en eiwitten zijn geoptimaliseerd, zoals beschreven in **Hoofdstuk 3**. Daarnaast presenteren we een nieuw algoritme om effecten van aggregatie in lange metingen uit te sluiten. Door dit algoritme hoeft men niet 'rond de aggregaten' te meten zoals gebruikelijk is. Het gebruik van PIE-F(C)CS met spFRET maakt het mogelijk om naast de concentratie- en diffusietijden, reactie kinetiek en meerdere populaties uit één enkele meting te distilleren. Door de gegevensanalyse na de acquisitie te optimaliseren kan een hoge mate van nauwkeurigheid voor de fysieke parameters worden bereikt. Dit betekent dat PIE-FCCS in combinatie met spFRET kleine verschillen tussen twee zeer vergelijkbare biologische samples kan ophelderen. Beide methodehoofdstukken worden afgesloten met validaties van de methoden uit experimenten. In **Hoofdstuk 4** laten we de effecten zien van veranderingen in DNA-sequentie, linker-DNA en buffersamenstelling op nucleosomen. In zoutconcentraties die lager zijn dan fysiologische omstandigheden, hebben nucleosomen de voorkeur om in een gesloten conformatie te zijn. Bij toenemende NaCl-concentratie neemt de openingssnelheid van het nucleosoom toe terwijl de sluitingssnelheid hetzelfde blijft. DNA-histon-interacties worden sterker met de lengte van linker-DNA. De insertie van het Glucocorticoid Response Element (GRE) in de Widom 601 DNA-sequentie vermindert de stabiliteit van het nucleosoom wanneer het GRE dieper in het nucleosoom werd ingebracht (d.w.z. naar de dyade toe). Behalve het nucleosoom waarin de GRE naar de histonkern is gericht, verhogen alle GRE-nucleosomen hun openingssnelheden bij toenemende NaCl-concentratie. Het positioneren van de GRE in de richting van de histonkern verhoogt niet de openingssnelheid, maar verlaagt juist de sluitingssnelheid. De GRE zou de stijfheid van de DNA-streng kunnen vergroten, waardoor het energetisch minder gunstig wordt om naar de histonkern te buigen. Het positioneren van de GRE naar de dyad vermindert de kritische NaCl-concentratie waarbij het dynamisch evenwicht verandert. Het vergelijken van PIE-FCS-resultaten met bevindingen van

burst-analyse voor nucleosomen met variabele linker-DNA-lengtes in lage NaCl-concentratie geeft inzicht in het effect van linker-DNA op compactie. Het nucleosoom met de kortste linkers heeft juist een hoge FRET-populatie vergelijkbaar met het nucleosoom met de kruisende linkers in burst-analyse, terwijl PIE-FCS een gesloten fractie vertoont die vergelijkbaar was met nucleosomen zonder DNA te kruisen. Toevoeging van stabilisatorverbindingen en zuurstofvangers vertraagt de nucleosomale dynamiek aanzienlijk en nucleosomen bevinden zich dan meer in een gesloten conformatie. Men zou kunnen stellen dat het toevoegen van stabilisatoren lijkt op meer *in vivo* opeengepakte omgevingen, en we willen benadrukken dat het effect van additieven op de dynamiek en stabiliteit in overweging moet worden genomen bij het vergelijken van experimenten.

In **Hoofdstuk 5** kwantificeren we het effect van posttranslationale histon modificatie (PTM) H3K36me3 op de stabiliteit en dynamiek van nucleosomen. Nucleosomen die de H3K36-trimethylering bevatten, lijken meer open, gebaseerd op hun gemiddelde FRET- en evenwichtsconstanten. Het FRET-signaal laat zien dat de trimethylering de buiging van de nucleosomale uitgang naar de histonkern niet remt. Het verlaagt echter het aantal elektrostatistische interacties met een factor twee. Deze afname in DNA-histon-interacties leidt ook tot snellere dynamiek van H3K36me3-nucleosomen in zowel lage als hoge zoutomstandigheden. Verhoogde kinetiek door minder (sterke) interacties tussen DNA-armen en histonkern kan de manier zijn waarop de trimethylering de binding aan nucleosomaal DNA vergemakkelijkt in processen zoals transcriptie en DNA-herstel. Het gebruik van PIE-FCCS op enkelvoudig gelabelde nucleosomen en gelabelde varianten van het LEDGF-eiwit (wildtype en AT-hook deficiënt) laat zien dat H3K36me3 de LEDGF-affiniteit voor nucleosomen verhoogt. De diffusietijden die voor verschillende LEDGF-nucleosoom complexen worden gevonden verschillen met meer dan een milliseconde van elkaar, wat verschillende wijzen van interactie aangeeft, afhankelijk van de LEDGF-variant en of H3K36me3 al dan niet aanwezig was in het nucleosoom. Het langzaamste complex, de combinatie van LEDGF-WT en nucleosomen zonder H3K36me3, diffundeert alsnog sneller dan open nucleosomen. De resultaten voor fracties en diffusietijden voor experimenten op WT-nucleosomen lijken nauwkeuriger te zijn dan die van experimenten op H3K36me3-nucleosomen; aangezien deze waarden zijn gebaseerd op de correlatiecurve, die het nucleosoom in bepaalde conformationele toestanden vertegenwoordigt, kunnen de grote

fouten worden veroorzaakt door overgangstoestanden als gevolg van de veranderde interacties van de H3-staart met nucleosomaal DNA. Ondanks het verlies van gesloten nucleosomen aan het begin van een experiment, is het verlies van FRET per nucleosoom minimaal, afhankelijk van het eiwit en de nucleosoomvarianten, wat impliceert dat LEDGF binding voornamelijk via vrije open nucleosomen verloopt en dat LEDGF-binding open nucleosomen stabiliseert.

In **Hoofdstuk 6** maken we de transitie van *in vitro* met gezuiverde eiwitten en DNA naar *ex vivo* experimenten met GR in nucleair extract. Toevoeging van het eiwit c-Jun verhoogt de diffusietijd van DNA enigszins, na uitsluiting van condensaten. Het verhogen van de concentratie van c-Jun verhoogt de diffusietijd van DNA niet, wanneer het signaal wordt gefilterd van bijdragen van condensaten. Deze waarnemingen wijzen op niet-specifieke interacties van c-Jun met DNA en impliceren een DNA-condenserende rol voor c-Jun tijdens transcriptie. Het verklaren van de interactie van GR in een nucleair extract met DNA of nucleosomen was minder eenvoudig; in agarosegel is geactiveerd GR in het nucleaire extract zichtbaar als een uitgesmeerde band in de gebieden met hoog molecuulgewicht. Dit uitsmeren kan het gevolg zijn van niet-specifieke, kortstondige interacties met andere eiwitten in het extract, wat eerder is waargenomen. Het kan ook een intrinsieke eigenschap zijn van de GR die zich in een ongeordende toestand bevindt, wat vaak wordt gecorreleerd aan het activiteitsniveau van een eiwit. Deze resultaten zijn in overeenstemming met die van FCCS experimenten, waar complexen van GR met ofwel DNA of nucleosoom nauwelijks zichtbaar zijn, wat een lage concentratie van een complex impliceert. Voor alle DNA- en nucleosoomconstructen zijn de bindingsaffiniteiten 20 nM en groter, en statistisch is er geen significant verschil in dissociatie-energie voor DNA-constructen GREh, GRE2 en GRE3. Deze resultaten verschillen van eerdere resultaten, waar werd aangetoond dat de compactie van DNA in nucleosomen, evenals het inbedden van de GRE-positie in nucleosomen, de affiniteit van GR verhoogt. Hoewel de verschillen in affiniteit klein waren, lijkt het erop dat *ex vivo*, dissociatie afhangt van de toegankelijkheid van het GRE in nucleosoom, d.w.z. een GRE die dicht bij de nucleosomale uitgang is geplaatst verhoogt de toegang voor GR.

De combinatie van deze bevindingen laat zien dat kleine veranderingen in histon-DNA-interacties, hetzij structureel of elektrostatisch, een significant effect kunnen hebben op de stabiliteit en kinetiek van nucleosomen *in vitro*.

In deze thesis hebben we laten zien dat verschillen zo klein als 7 baseparen meetbaar zijn met onze combinatie van microscopische technieken. Wanneer deze waarnemingen worden doorgetrokken naar *in vivo*-omgevingen, impliceren ze dat slechts zeer kleine energiever verschillen nodig zijn om veranderingen in de chromatine compactie op gang te brengen, waardoor DNA-eiwitinteracties en daaropvolgende processen zoals transcriptie mogelijk worden. PIE-FCCS gecombineerd met spFRET is een uitstekende techniek voor het kwantificeren van deze subtiele verschillen in zowel structurele als kinetische parameters, en zou met kleine aanpassingen ook gebruikt kunnen worden voor het meten aan *in vivo* systemen om uit te vinden welke veranderingen aan DNA sequentie, lengte of histon staarten doorslaggevend is voor de stabiliteit van en dynamiek in chromatine.



Summary

Nucleosomes are the first level of DNA compaction in the nucleus of eukaryotic cells. In human cells, about two meters of DNA is condensed in this way into a sphere with a diameter of six micrometres. Although it is in this highly condensed state, called chromatin, the DNA in chromatin is involved in processes such as transcription and DNA repair, for which the DNA must be accessible. To this end, the structure of chromatin is modulated by histone tail modifications, protein recognition elements in the DNA sequence and a large number of protein-DNA interactions. Aforementioned processes often require direct DNA access and are therefore dependent on a change in nucleosome compaction. In this thesis I describe the results of Pulsed Interleaved Excitation and Fluorescence (Cross) Correlation Spectroscopy (PIE-F(C)CS) combined with single-pair Förster Resonance Energy Transfer (spFRET) used to study dynamics in single nucleosomes, which depends on subtle differences in the length of DNA ends, DNA sequence, histone variants and specific and non-specific protein interactions. This technique, which can resolve distances between two fluorophores of only a few nanometers, is an excellent technique to monitor changes in nucleosomal compaction, as the nucleosome is only ten nanometers in diameter. In combination with F(C)CS and PIE, spFRET makes it possible to monitor conformational dynamics on a timescale of micro to milliseconds.

Chapter 1 provides an overview of previous studies of the nucleosome, its role in chromatin compaction *in vitro* and *in vivo* and the effects of DNA sequence, histone modifications and protein interactions on stability and dynamics of nucleosomes. Studies show a dual role for the nucleosome; as a stable structure that is recognized by transcription factors that selectively bind to specific histone modifications or DNA sequences, and as a dynamic entity that is able to temporarily release DNA, thereby regulating processes on the DNA. All of this happens while DNA is folded in the cells in a seemingly disorganized way. In **Chapters 2 and 3** we take a closer look at the optical, analytical and biological tools we developed and used to reveal conformational changes in a single nucleosome. In **Chapter 2** we describe the microscope setup and analysis process for single-molecule experiments.

We show how quantifying the subtleties of fluorophore signals in the microscope setup results in reliable correlation curves of those fluorescent signals after signal processing. The synthesis, purification and processing of DNA, nucleosomes and proteins were optimized, as described in **Chapter 3**. In addition, we present a new algorithm to exclude effects of aggregation in long measurements. With this algorithm one does not have to measure 'around the aggregates' as is usual. PIE-F(C)CS with spFRET was used to obtain the concentration, diffusion times and reaction kinetics of multiple populations from a single measurement. By optimizing the data analysis, a high degree of accuracy for the physical parameters can be achieved. This means that PIE-FCCS in combination with spFRET can elucidate small differences between two very similar biological samples. Both methods chapters are concluded with validations of the experimental methods.

In **Chapter 4** we show the effects of changes in DNA sequence, linker DNA and buffer composition on nucleosomes. In salt concentrations below physiological conditions, nucleosomes prefer to be in a closed conformation. With increasing NaCl concentration, the opening rate of the nucleosome increases while the closing rate remains the same. DNA-histone interactions become stronger with the length of linker DNA. The insertion of the Glucocorticoid Response Element (GRE) into the Widom 601 DNA sequence reduces nucleosome stability more as the GRE was introduced deeper into the nucleosome (i.e., toward the dyad). Except for the nucleosome in which the GRE faces the histone core, all GRE nucleosomes increase their opening rates with increasing NaCl concentration. Positioning the GRE toward the histone core does not increase opening speed, but rather decreases closing speed. The GRE could increase the stiffness of the DNA strand, making it energetically less favorable to bend towards the histone core. Positioning the GRE towards the dyad reduces the critical NaCl concentration at which the dynamic equilibrium changes. Comparing PIE-FCS results with findings from burst analysis for nucleosomes with variable linker DNA lengths in low NaCl concentration provides insight into the effect of linker DNA on compaction. The nucleosome with the shortest linkers has a high FRET population similar to the nucleosome with the crossing linkers in burst analysis, while PIE-FCS shows a closed fraction that was similar to nucleosomes without crossing DNA. Addition of stabilizer compounds and oxygen scavengers significantly slow down nucleosomal dynamics and nucleosomes are then more in a closed conformation. It could be argued that adding stabilizers resembles

more *in vivo* packed environments, and we want to emphasize that the effect of additives on dynamics and stability should be considered when comparing experiments.

In **Chapter 5** we quantify the effect of post-translational histone modification (PTM) H3K36me3 on nucleosome stability and dynamics. Nucleosomes containing H3K36 trimethylation appear more open, based on mean FRET and equilibrium constants. The FRET signal shows that the trimethylation does not inhibit bending of the nucleosomal DNA to the histone core. However, it reduces the number of electrostatic interactions by a factor of two. This decrease in DNA-histone interactions also leads to faster dynamics of H3K36me3 nucleosomes in both low and high salt conditions. Increased kinetics due to fewer interactions between DNA arms and histone core may be the reason how the trimethylation facilitates binding to nucleosomal DNA in processes such as transcription and DNA repair. The use of PIE-FCCS on single-labeled nucleosomes and labeled variants of the LEDGF protein (wild-type and AT-hook deficient) shows that H3K36me3 increases LEDGF affinity for nucleosomes. The diffusion times found for different LEDGF-nucleosome complexes differ by more than a millisecond, indicating different modes of interaction, depending on the LEDGF variant, and whether or not H3K36me3 was present in the nucleosome. The slowest complex, the combination of LEDGF-WT and nucleosomes without H3K36me3, still diffuses faster than open nucleosomes. The results for fractions and diffusion times for experiments on WT nucleosomes appear to be more accurate than those for experiments on H3K36me3 nucleosomes; since these values are based on the correlation curve, which represents the nucleosome in certain conformational states, large errors may be caused by transition states due to the altered interactions of the H3 tail with nucleosomal DNA. Despite the loss of closed nucleosomes at the start of an experiment, the loss of FRET per nucleosome is minimal, depending on the protein and nucleosome variants, implying that LEDGF binding is primarily via free open nucleosomes and suggesting that LEDGF binding stabilizes open nucleosomes.

In **Chapter 6** we make the transition from *in vitro* with purified proteins and DNA to *ex vivo* experiments with GR in nuclear extract. Addition of c-Jun slightly increases DNA diffusion time, after exclusion of condensates. Increasing the concentration of c-Jun does not increase DNA diffusion time when the signal is filtered from condensate contributions. These observa-

tions indicate non-specific interactions of c-Jun with DNA and may imply a DNA condensing role for c-Jun during transcription. Explaining the interaction of GR in a nuclear extract with DNA or nucleosomes has been less straightforward; in agarose gel, activated GR in the nuclear extract is visible as a smeared band in the high molecular weight regions. This smearing may be due to non-specific, transient interactions with other proteins in the extract, which has been observed previously. It may also be an intrinsic property of the GR being in a disordered state, which is often correlated to a protein's activity level. These results are in agreement with those of FCCS experiments, where complexes of GR with either DNA or nucleosome are barely visible, implying a low concentration of a complex. For all DNA and nucleosome constructs, binding affinities are 20 nM and greater, and there is no significant difference in dissociation energy for DNA constructs GREh, GRE2 and GRE3. These results differ from previous results, where the compaction of DNA into nucleosomes, as well as the embedding of the GRE position in nucleosomes, were shown to increase the affinity of GR. Here, GR had the highest affinity for nucleosomes containing the GRE closest to the exit (GREh). Although differences in affinity were small, it appears that *ex vivo*, dissociation depends on accessibility of the GRE in nucleosome, i.e. a GRE placed closer to the nucleosomal exit increases access for GR. In conclusion, the combination of these findings shows that small changes to the nucleosome, either structurally or electrostatically, can have a significant effect on its stability and breathing dynamics *in vitro*. In thesis we have shown that differences as small as changing 7 base pairs can be detected with our combination of microscopic techniques. Extending to *in vivo* environments, these observations imply only very small differences in energy are necessary to initiate changes in chromatin compaction, allowing DNA-protein interactions and subsequent processes such as transcription. PIE-FCCS combined with spFRET is an excellent tool for resolving these energetically subtle differences in structural as well as kinetic parameters, and with small adaptations could also be used to measure in *in vivo* systems to investigate which changes in DNA sequence, DNA linker length or histone tails is decisive factor for the stability and dynamics of chromatin.

Publications

spFRET reveals changes in nucleosomal breathing by neighbouring nucleosomes. R. Buning, W. Kropff, **K. Martens** and S.J.T. van Noort. *J Phys: Condens Matter*, 2015, 27(6)

Reliability and accuracy of single-molecule FRET studies for characterization of structural dynamics and distances in proteins. G. Agam, C. Gebhardt, M. Popara, R. Mächtel, J. Folz, B. Ambrose, N. Chamachi, T.D. Craggs, M de Boer, D. Grohmann, T. Ha, A. Hartmann, J. Hendrix, V. Hirschfeld, C.G. Hübner, T. Hugel, C. Jackers, D. Kammerer, H. Kang, A. Kapanidis, G. Krainer, K. Kramm, E. Lemke, E. Lerner, E. Margeat, **K. Martens**, J. Michaelis, J. Mitra, G.G. Moya Muñoz, R. Quast, N. Robb, M. Sattler, M. Schlierf, J. Schneider, T. Schröder, A. Sefer, P.S. Tan, J. Thurn, P. Tinnefeld, S.J.T. van Noort, S. Weiss, N. Zijlstra, A. Barth, C.A.M. Seidel, D.C. Lamb, T. Cordes. *Biorxiv*, 2022. *Submitted to Nature Methods*.



Curriculum Vitae

I was born on January 8th 1985 in Nijmegen, the Netherlands. I attended primary and high school in Tegelen and Venlo (Gymnasium, Collegium Marianum). In 2003 I moved to Leiden to study Astronomy and after one year switched to Chemistry. During my bachelors I followed several courses in Mathematics, was active in many committees of the study association De Leidsche Flesch, and became member of her board for educational and study activities in 2006-2007. My bachelor internship was performed in the Theoretical Chemistry group of prof. Kroes on modelling scattering of H₂ over Cu using potential energy surfaces. In 2010 I started my master Biological Chemistry with electives in mathematical biology, natural computing and neurocognition. I performed an *in silico* study on the binding and interaction of stress hormone receptors GR and MR at the Medical Pharmacology group of prof. de Kloet, and an experimental study of nucleosome dynamics at the Biophysics group of prof. van Noort.

After obtaining my masters degree in 2012 I started working at the Leiden Institute of Chemistry as a policy officer and project coordinator for the national Cyttron II consortium. In 2014 I returned to the group of prof. van Noort for a PhD position to characterize DNA-GR interactions in chromatin using FCCS and spFRET. I presented my work at national and international conferences, seminars, winter, spring and summer schools. I assisted in bachelor and master courses on experimental and theoretical Biophysics and Molecular Quantum Chemistry, and (co-)supervised several bachelor and master students.

In 2019 I took up the role of research policy officer in the academic affairs department under the board and dean of the Science faculty; end of 2021, I switched to NWO to the position of programme coordinator.



Acknowledgements

Many people have helped shape the contents of this thesis, and I would like to thank them for their contributions. First of all, thanks to John, for giving me the opportunity to do a PhD on a topic that was so serendipitously a combination of my two master internships. Thank you for your enthusiasm and commitment, and engaging work meetings; you have taught me many things. Also a warm appreciation of Helmut Schiessel, Michel Orrit, Thomas Schmidt and Stefan Semrau for interesting discussions, insights and support throughout my PhD. A special thanks to Yvonne, whose support in bureaucracy as well as psychology were a silver lining. I would like to acknowledge the expert contributions of Chi, Lionel, Ineke and Sylvie, having shown me the biochemistry crucial for my work.

Babette, your support and camaraderie have inspired me and will stay with me for the rest of my life. Thank you for being there beside me. Similar for my students Mark, Sanne and Dion; thank you for your unwavering hard work, giving me new insights and ideas, and being an integral part of my PhD journey. Melissa, thank you for our many many interesting and inspiring talks on physics, biology and life, for your patience, hygge and true friendship.

Furthermore, I would like to thank the laborious and immensely creative peoples of the FMD and ELD, without whom my confocal setup would not exist. A heartfelt thanks to my chromatin group colleagues Jeremie, Sara, Artur, Wietske, Hidde-Peter, Meng, Thomas, Redmar, Nicholas, Alex, Gert-Jan, Klaas, and Ivo for their valuable input, knowledge sharing, the laughter as well as comfort through the good and the bad times.

Also a big thank you to Biophysics supergroup and satellite members Lena, Olga, Emrah, Dominique, Rolf, Hedde, Marija, Saptaswa, Biswajit, Martin, Aquiles, Sacha, Kaveh, Daniel, Paul, Flavio, Joeri, Maria, Nelli, Esmee, Noemie, Patrick, Maria, Mazène, Marleen, Julia, Radek, Rick, Nikolay, Cynric, Falco, Bert, Elger, Margherita, Kim, Raoul, Nedim, Freek, Vincent, Willem-Jan, Wim, Stefano, Nigel, Loes, Daan, Caspar, Jamie and Jurien for the impromptu coffee breaks, lunches, technical and philosophical discussions and of course parties.

I would like to acknowledge my Leuven collaborators Wout, Tine and Willem for their insights in LEDGF binding and graciously sharing their LEDGF and modified histone samples with us. Thank you Marcel, Veer, Onno and other GR meeting group members for sharing your expertise on GR as well as your cell lines. A heartfelt thank you to Lennart, Christine, Anne, Ireth, Lennard, Samia, Fabrizio and Jimi as well as others of the Schiessel, Kraft, van Hecke and Giomi groups, for our insightful and critical discussions on (bio)physics, proofreading parts of my thesis and aiding with the lay-out. My colleagues of the Casimir Graduate school PhD committee, Marije, Gesa, Orkide, Bob, Marios, Koen, Floris, Robbie, Guoji, Nicole and Michał; thank you for your positive outlooks, support and of course organizing so many amazing and engaging activities for our community. Karlien, Natasja, Annemieke, Oliver, Louis and Tom, thank you for our nice dinners, drinks and distractions, even when they often ended in talks about physics.

Dear Ingeborg, Nils, Daniëlle and Eric, thank you for all your support and patience with me. Dear Papa en Mama, without you I would not be the person I am today; thank you for always supporting and believing in me.